UNIVERSITY OF COPENHAGEN
FACULTY OF SCIENCE

Angular distributions of atmospheric leptons via two-dimensional matrix cascade equations

Master of Science Thesis

Tetiana Kozynets

Supervisor
D. Jason Koskinen

Date
31st October, 2022

Abstract

Hadronic interactions of cosmic rays in the atmosphere induce rich cascades of daughter particles, including atmospheric neutrinos and muons. The atmospheric neutrino flux constitutes the main signal for neutrino oscillation measurements in experiments such as IceCube, KM3NeT, and Super-Kamiokande, and an accurate prediction of the flux expected prior to oscillations is crucial. This requires comprehensive modelling of the evolution of hadronic cascades in the atmosphere, which is unfeasible to do analytically. The Monte Carlo simulations, on the other hand, remain computationally expensive and lack flexibility when it comes to the investigation of systematic uncertainties.

These complications are mitigated in the numerical Matrix Cascade Equations (MCEq) code, which solves the system of coupled differential equations for particle production, interaction, and decay at extremely low computational costs. Previously, the MCEq framework included longitudinal-only development of air showers, which is a sufficient approximation for modelling neutrino fluxes at energies of $\mathcal{O}(10\,\mathrm{GeV})$ and above. However, the mentioned experiments are expected to be sensitive to neutrino energies of a few GeV and below within the next decade, following the deployment of the IceCube-Upgrade, KM3NeT/ORCA, and Hyper-Kamiokande, respectively. Since the lateral component of hadronic cascades becomes important at these low energies, three-dimensional calculation schemes are required for precision calculations of atmospheric neutrino angular distributions.

The necessary transition step between the one-dimensional and the three-dimensional treatments is a two-dimensional calculation, which takes into account the angular development of the air showers due to the deflection of the cascade secondaries from the primary cosmic ray axis. In this thesis, we develop a novel numerical technique for the combined longitudinal and angular evolution of the air showers using the MCEq code. By comparing our numerical solutions to those obtained with the standard Monte Carlo code CORSIKA, we show that our tool (dubbed "2D MCEq") is fast and accurate. This work is therefore providing a compelling alternative to the Monte Carlo codes and pushing the atmospheric neutrino flux calculations to the frontier of computational performance and precision.

Statement of contributions

This work develops an extension to an existing software framework, MCEq, which was written and is maintained by Anatoli Fedynitch [1, 2]. The idea to treat angular development of hadronic cascades as convolutions, which draws inspiration from image processing techniques, belongs to A. Fedynitch. Based on this idea and the numerical formulation of the one-dimensional cascade equations within the 1D MCEq framework, I have developed the two-dimensional cascade theory in angular and frequency domains and have independently performed all of the computations and code development thereon. Notable exceptions are the usage of the public impy interface [3] for running hadronic interaction models, which was also developed primarily by A. Fedynitch, as well as the model-to-matrix conversion tool. This tool was written by A. Fedynitch for the pre-generation of the 1D MCEq histograms and extended by me to include the production of the 2D MCEq matrices. The large-scale Monte Carlo simulations necessary to produce these matrices were performed by me on the DiCOS computing clusters at Academia Sinica, with access granted to me by A. Fedynitch. The integration of all the 2D MCEq methods into the MCEq framework was performed by me independently, except for the implementation of the energy losses due to ionization, which fully follows that of 1D MCEq and was not re-implemented in this work. All of the CORSIKA simulations used to cross-check the 2D MCEq results were run by me independently. Unless explicitly stated in the figure/table captions, all of the figures/tables in this thesis are my original work.

The early stages of this project were presented by me at multiple scientific conferences, including VLVnT-2021, ICRC-2021, Nordic Physics Days 2021, and NEUTRINO-2022. The proceedings of the ICRC-2021 conference were published in [4] and are included in the appendices of this thesis. The NEUTRINO-2022 poster was also published online [5].

Acknowledgements

First and foremost, I would like to say thanks to my advisor, Jason Koskinen, who gave me absolute freedom in selecting my Master's thesis project "with the right of veto" and luckily did not veto this one. I am infinitely grateful for your trust in me and for the trust I have in you, for your genuine care and support throughout these years, and for making me feel so accepted and welcome in the IceCube group at the NBI. Your questions often make me realize which pieces are missing from my puzzle of physics knowledge, and I am always encouraged to search for them after our meetings. I cannot imagine having a different supervisor for my PhD project and am truly privileged to spend the next 2 years working with you.

Another simple truth is that this project would not have been possible without Anatoli Fedynitch, who is one of the best living scientists and the brightest minds I know. Going into this project, I was certain that it would be difficult and fascinating, because I would never expect anything less from working with you. From the way you structure your code to the way you structure your thoughts and workflow, I always have something to learn from you. I am so very grateful for all the meetings across the split timezones, for the 1,000 Earth's atmospheres we have drawn over Zoom, and for keeping my creativity within the sane boundaries. Wrapping up our fantastic multi-layered project, I can most certainly conclude that not everything is supposed to be solved with neural networks.

I cannot imagine the last two years without the IceCube group at the NBI, whose members contributed giant amounts to my scientific and personal development. *To Étienne:* you are the first true friend I made here, and it is an honour to be called a "new Étienne" in the group. You saw me start this project from our tiny apartment in Østerbro and have been with me through the good and the bad of it all. You and Arianna are truly my family (which will soon have 3/3 PhD holders in it), and I am excited to see where the paths of life will take us. *To James:* your infinite care and kindness made the difficult moments of this last year bearable for me. I am truly inspired by your natural curiosity and positive attitude to life, and I thank you for being the voice of reason and rationale when it comes to navigating academia, research, and personal matters. *To Kathrine:* it is a pure delight to be PhD-ing on the same timeline as you. You are an absolute role model for me, and I truly admire your brilliant mind, your warm character, and your philosophy-infused wisdom. I am so appreciative of the fact that I could always have a ridiculously long rant about transport equations when talking to you, and you would not only *totally get me*, but also share a similar struggle or experience. *To Markus*: thanks to the brilliant theorists like you, I cannot decide whether I would like to be a theorist or an experimentalist in my future career. The depth and the breadth of knowledge stored in your brain, and the ease with which you operate and disseminate it, inspire me daily. Your thoughtful questions at the group meetings always make me dig deeper and put more rigour into my statements and derivations. *To Rikke*: I am so very thankful for your friendship and for having our academic paths overlap. Your passion for pure research is contagious even when I am already infected, and your gentle care and curiosity have contributed so much to my wellbeing and progress. *To Leon B. and Kaare*: reading both of your theses was an inspiration for me and gave me lots of ideas on how to structure my own. I will cherish our hangouts over boiled water and the IceCube discussions, our board game nights, and remember being silly, smart, and human with you fondly. And finally, to my time-translated, CP-conjugated mirror image, *Tom Stuttard*: thank you for quantizing the spacetime and opening portals to other dimensions within the distance of one office desk. Gazing into the Universe with you is an experience worth living for.

None of the above words would have been written without my former mentors – Oleksandr Dovzhenko, Andrii Gilchuk, Carsten Krauss, and Scott Fallows – who showed me the world of physics, research, and astroparticle physics, respectively. I have unravelled the path towards the field that fits me very gradually, and it took you four to find the right match and make every day of my life a dream. I would also like to remember my dear friends from back home: Tania, Ania, Misha, Leon O., and Nastia, and to thank them for having built something that lasts over decades, countries, and continents. This thesis would not have been possible without the roads we have walked together and our shared and deep-rooted connection, which helps me maintain my sanity and grow as a person. To my incredible Copenhagen friends – Ada, Rita, Alex, Karolis, Jessa, Greta, Tymon, Filip and Kristian – thank you for reminding me to close my laptop lid every once in a while and for sharing so many wonderful human moments with me. Ada and Rita – your support and encouragement especially in these last few weeks of writing mean the world.

Last but most certainly not least, I would like to thank my family: my mom Iryna, my dad Oleksandr, and my brother Andrii, for their unconditional love and for having trust in the path I have chosen. I love you all endlessly, and I dedicate this thesis to you.

Contents

CHAPTER 0

Introduction

The discovery of cosmic rays and their "terrestrial imprint" in the form of atmospheric air showers marked a crucial milestone in the astroparticle physics research. The advances in the cosmic ray detection techniques uncovered the existence of a plethora of elementary particles and provided the first peek into their intricate dynamics – from creation in energetic collisions to numerous re-interactions and eventual spontaneous disintegration. These complex "cascading" processes have been successfully replicated at the man-made particle collider facilities, yielding even more insight into the building blocks of matter and the nature of their mutual interactions. Yet, as the cosmic rays maintain superiority in the range of accessible energies and constantly bombard the Earth's atmosphere from all directions, the air showers continue to provide a unique source of data for probing fundamental physics.

This chapter will review the historical trails that led to the discovery of cosmic rays and air showers, setting up the stage for the main actors in this thesis – the atmospheric leptons (neutrinos and muons). We will explain why, while being a mere "byproduct" of cosmic ray interactions in the atmosphere, these particles are at the forefront of modern particle physics research, and thus motivate the need to model their production and propagation with great care. With this motivation in mind, we will outline the essence of this work – the development of a novel numerical approach to air shower modelling, with a particular focus on the atmospheric lepton fluxes and the energy regime where the geometry of the air shower development becomes important.

0.1 HISTORICAL OVERVIEW

It was a seemingly mundane question, and a tedious investigation into it that followed, that jump-started an eventful century of cosmic ray research. In 1785, the father of electrostatics Charles-Augustin de Coulomb [6] discovered that the charged spheres in his torsion balance experiment eventually underwent a discharge, which was not expected as they were enclosed in an electrically insulated electrometer. This observation turned the community's attention to the conductivity of air – as the latter could then be the medium through which the charge flows out of the electrometer – and in particular, towards *the reason why* air becomes conductive. The existence of a source of ionizing radiation penetrating the air was a plausible hypothesis, confirmed in 1899 by Elster and Geitel [7]. Importantly, they showed that the discharge could be reduced if the device were put into a thick metal box, which pointed towards a literal "outside the box" solution in the form of external ionizing agents. Yet, this conclusion left the discharge problem enthusiasts with the entire 4π solid angle around the metal container to explore.

The first attempt to cover some portion of the 4π with experimental evidence was to, perhaps most naturally, look down. In 1909, Theodor Wulf conducted a series of discharge measurements using his own two-string electroscope and concluded that the sources of ionizing radiation must be located up to 1 m below the surface of the Earth [8, 9]. Importantly, thanks to the discovery of radioactivity by Becquerel just 13 years earlier [10], Wulf could associate the claimed underground sources with radioactive γ-isotopes, and thereby "blame" the discharge phenomenon on the γ-radiation. According to Wulf, any possible contribution to the ionization rate coming from the atmosphere itself had to be negligibly small and impossible to measure.

In 1910, a contradicting piece of evidence came from Domenico Pacini, who continued the attempts to "look down" but added the twist of relocating from land to open sea to do so. At distances of nearly 500 m away from the shore, where the water depths were larger than 4 m, Pacini could safely neglect any ionization sources hiding in the soil. Surprisingly, using the same Wulf-type electrometer, Pacini found that the discharge-responsible ionization on the sea constituted nearly 2/3 of its terrestrial levels. At the same time, the ionization rates decreased significantly when the container with the electrometer was submerged in water [11, 12][1]. This meant that a sizeable portion of the radiation *must* come from the atmosphere... and that it was finally time to *look up*.

It is worth noting that the idea of performing a dedicated measurement of the ionization rate in the atmosphere itself was entertained even earlier (i.e., prior to Pacini's findings) by Franz Linke [14]. Between 1902–1903, he carried out multiple balloon flights up to an altitude of 5500 m and measured the

[1] See also [13] for translation.

discharge in a gold leaf electrometer as a function of altitude. He found that the ionization rate at 1000 m above the Earth's surface dropped compared to the sea level, which was consistent with Wulf's hypothesis that most of the radiation must come from the isotopes in the upper layers of the Earth. However, this expected initial decrease in the ionization rate was followed by an increase – so dramatic that at at the maximum altitude of Linke's flights it exceeded the ionization levels at Earth by a factor 4.

While Linke's measurements were not taken seriously at the time, the work of Pacini could not be as easily overlooked. Further evidence of the existence of the ionizing radiation in the atmosphere was once again sought by Wulf, who carried his electrometer to the top of the 300 m-high Eiffel tower in 1910 [15]. In parallel, Albert Gockel condected a series of balloon flights in Switzerland, where he measured the ionization rate up to 4500 m above the sea level [16, 17]. Both studies found no increase in the ionization rate with the altitude, although the observed decrease was much smaller than expected had the Earth's radioactivity been solely responsible for the electrometer discharge.

The dispute was solved by Victor Hess, who took the balloon measurements to the next level of precision. In particular, he conducted measurements during both day and night to check if solar activity had any influence on the ionization rate, and brought separate electrometers to measure γ- and β-radiation as a function of altitude. When Hess reached the highest altitude of his flights in 1912 (4800 m), he could make three conclusions with great confidence [18]. First, after the slight initial decrease, the ionization rate showed an increase as a function of altitude for all three electrometers he brought on board – suggesting that *the highly penetrating ionizing radiation must be entering the atmosphere from above*, and thus confirming the previous study by Linke. Second, Hess found no difference in the ionization rate measurements between day and night, excluding the possibility of the Sun being the prime source of this radiation. And third, as the altitude dependence of the ionization rate was similar between the γ and the β detectors, both must have been either the primary constituents of the incident radiation or its secondary products upon entering the atmosphere. In 1913–1914, the findings of Hess were confirmed by Kolhörster, who reached a record altitude of 9300 m during his balloon flight and measured the γ ionization rate which exceeded, by a factor 4, that recorded by Hess at 4800 m [19, 20]. Twenty years later, the characteristic altitude dependence found by Hess and Kolhörster was continued by Regener all the way up to 30 km above the sea level [21].

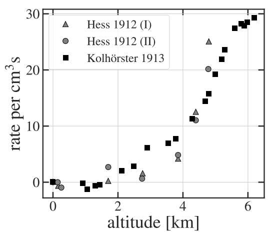

Figure 0.1 – Altitude dependence of the ionization rate [18–20].

Despite the remaining skepticism regarding the apparent extraterrestrial origin of the discovered ionizing radiation, the arguments in its favour solidified by the late 1920s. At this point, the focus shifted to the nature of the radiation rather than its origin – and in that regard, significant advances were made thanks to the emerging new technology. The early images from Wilson's cloud chamber, where the exposure of the water vapour to the ionizing radiation led to the formation of water droplets around the electron-stripped ions, already showed several straight tracks. In 1927, Skobelzyn (by pure accident) also found two high-energy tracks in his cloud chamber photographs – an in a dedicated follow-up observation, discovered 32 more [22]. The estimated energy of these tracks (>15 MeV) pointed to their association with the cosmic rays, and the very fact that they were visible in the cloud chamber – to them being electrically charged. Further evidence supporting the "charged particle" nature of the cosmic radiation came from the measurements with the Geiger-Müller counter, which was developed by Geiger and Müller in 1928 [23]. The operational principle of the counter consisted in accelerating the knock-on electrons using a strong electric field, causing further ionization of the gas filling the counter tube and the subsequent multiplication of the electron cascade. While the Geiger-Müller detectors successfully triggered on the incident charged radiation, there was no way to tell from the response of a single detector whether the charged particles are a "soft" secondary component of the primary cosmic radiation, or a part of the primary radiation itself. The stakes for making this distinction were especially high at the time when the dominant view in the community was still that promoted by Millikan, i.e. that any charged component to the ionizing radiation in the atmosphere must be secondary to the cosmic γ-radiation. It was thanks to the coincidence experiment by Bothe and Kolhörster that the "primary γ" hypothesis started losing its original popularity [24]. In 1929, they constructed a setup with two Geiger-Müller counters placed next to each other, aiming to measure temporally coincident signals in the two detectors. They showed that when a gold absorber is placed between the two counters, the rate of the signal in the second counter decreases only slightly compared to the setup without the absorber. According to Bothe and Kolhörster, the electrons would not have had a sufficient energy to pass the gold absorber had they been produced in a Compton scattering of the primary γ rays. While this did not conclusively mean that the primary *cosmic rays*[2] consisted of the charged electrons, it raised significant doubts about the high-energy photons being the definite and the only primaries. Thus, the Bothe-Kolhörster coincidence experiment helped the emerging community move forward to the exploration of other primary composition hypotheses.

That the primary cosmic rays are, in fact, charged particles, was finally confirmed by the geomagnetic latitude dependence of the ionization rate. Indeed, if the primary particles were charged, the intensity of the secondary signal would have to be smallest along the geomagnetic equator due to the stronger deflection in the geomagnetic field. This was exactly the behaviour observed by Compton, Turner, and others [25]. In addition, the possibility of determining the sign of the primary radiation charge from the asymmetry in

[2]The term "cosmic rays" is typically attributed to Millikan, who, ironically, disputed the extraterrestrial origin of the cosmic radiation in the 1920s.

its arrival directions was predicted by Rossi in the 1930s [26]. Shortly after, Alvarez and Compton [27], and eventually Rossi himself [28], experimentally found that the intensity of charged particles arriving from the east is less than that of the particles arriving from the west (later called an East-West effect). This meant that the cosmic ray primaries had to be predominantly *positively* charged. In 1941, Schein concluded that these charged particles were, for the most part, protons [29] – although that conclusion required several more puzzle pieces to complete the picture of the cosmic rays' journey in the atmosphere.

In particular, it required the discovery of the so-called *air showers* – the cascades of particles developing in the atmosphere as the result of cosmic ray interactions. Rossi was the first to detect the development of such cascades in dense matter [30, 31]. Building upon the coincidence technique of Bothe and Kolhörster, he arranged three Geiger-Müller counters in a circuit and put them in a lead box with a removable lid. The latter acted as an absorber screen, and using the lids with different thicknesses allowed Rossi to obtain the so-called "transition curves" – i.e. the coincidence rate as a function of the absorber thickness. Importantly, Rossi found that when the thickness was increased, the coincidence rate first rose and only then dropped, which pointed to the production of extra particles in the lid itself. The same principle obviously held in the atmosphere, which, albeit less dense, also acted as a target medium for the cosmic ray primaries to produce particle showers. Schmeiser, Bothe, and Kolhörster confirmed this experimentally in 1938, additionally showing that the rate of coincidence dropped as a function of separation distance between the counters [32]. Not only did this speak in favour of the air shower hypothesis, but it also showed, for the first time, that these showers had a *lateral extent*[3]. This was further confirmed in 1939 by Auger [33], who separated the Geiger counters by distances up 300 m and provided the first estimate of the primary energy (10^{15} eV, which is now known to be roughly the upper energy limit for the Galactic cosmic rays [35, 36]).

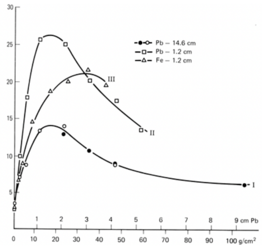

Figure 0.2 – Rossi's transition curves [30, 31].

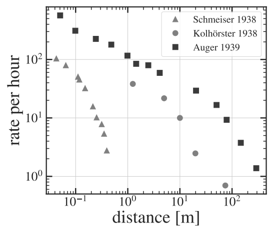

Figure 0.3 – First evidence of the lateral extent of air showers [32–34].

In a later analysis of Rossi's counting experiments, the "soft" component of the transition curve (the one exhibiting an initial increase followed by a drop) was attributed to secondary electrons, whose contribution to the radiation at the top of the atmosphere was negligible. This conclusion was a success of the electromagnetic cascade theory developed by Bhabha and Heitler [37] – the framework that put together the ionization energy losses by electrons, electron-positron pair production, Bremsstrahlung radiation, and Compton scattering. However, Rossi's transition curves also featured a long tail – the so-called "hard" component – which was far more penetrating and dropped off less rapidly as a function of the absorber thickness. Through balloon experiments, Schein, Jesse, and Wollan discovered that the counting rate of this hard radiation increased steadily with altitude and did not exhibit a

[3] The notion of the lateral (or angular) extent of the air showers will be central to this thesis.

maximum [29]. Therefore, it meant that the primary particle that produces the hard radiation *cannot be unstable* – else its decay would cause the drop-off of the hard radiation curve early in the atmosphere. This excluded the so-called mesotron – the particle postulated in 1937 by Anderson and Neddermeyer and now known to be a muon [38, 39] – as a possible primary. All of the gathered evidence on the particle nature of the primary radiation thus pointed to the protons, which, as we know now, indeed dominate the cosmic ray spectrum composition.

What about the muons, the "uncalled for" unstable particles whose existence was discovered amidst the hunt for the cosmic ray primaries? With their charge being equal to that of the electron and their mass being nearly 200 times larger, they were found to have suppressed radiative losses and penetrate matter further, thereby contributing to the hard radiation tail in Rossi's curves. At the same time, the muons were speculated to be responsible for the binding force between nucleons (e.g. protons and neutrons) inside a nucleus – i.e., to mediate the Yukawa interaction. However, even though the mass of the muon was roughly consistent with that postulated in the Yukawa theory, the mean lifetime of the muon at rest ($\sim 2\mu s$) exceeded the prediction by nearly 100 times [40, 41]. The paradox was solved in 1947, when Powell [42] and Perkins [43] independently observed the nuclear disintegration in the photographic plates due to the capture of a "slow charged particle." This particle turned out to be a pion – a crucial intermediate link between the primary protons and the secondary muons, which also happened to perfectly satisfy the Yukawa theory of nuclear forces. Shortly after, the kaon was discovered by Rochester and Butler [44] via the decay to charged pions. Nowadays, the pion and the kaon are known to form the group of light mesons whose disintegration in the atmosphere is responsible for the evolution of particle showers and the production of atmospheric leptons – muons and neutrinos.

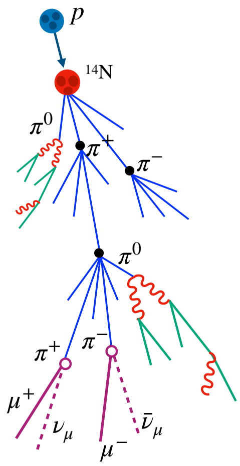

Figure 0.4 – Neutrino production in an air shower.

Neutrinos, unlike most cosmic ray secondaries discovered in the mid-20th century, do not carry an electromagnetic charge and are therefore practically "invisible" as they pass through matter. They are only observable through their extremely rare (*weak*) interactions with matter and subsequent production of charged particles. Due to these experimental complications, the first *atmospheric neutrinos* were detected via production of muons in deep underground observatories only in the 1960s [45, 46] – which is almost 30 years after the existence of neutrinos was first postulated from a completely different angle. In the 1910s, which most of the cosmic ray physicists spent in flights to the top of the atmosphere and back, the "terrestrial" particle physics was preoccupied with understanding the continuous electron spectrum in the nuclear beta decay. Assuming that a neutron had to decay into a proton and an electron via a two-body process, the electron was expected to have a very narrow kinetic energy distribution. However, the experiments by Chadwick, Ellis, and Wooster [47, 48] did not support this hypothesis and showed a spread of the electron kinetic energies instead. In 1930, Pauli proposed a neutral and weakly interacting particle (now identified as a neutrino), which would take away some of the kinetic energy in a three-body decay of the neutron and thereby explain the electron's diffuse spectrum [49]. The introduction of neutrinos into the so-called *Standard Model of particle physics* thus helped resolve one of the biggest experimental conundrums of the 20$^{\text{th}}$ century – and it is perhaps ironic that at present, neutrinos constitute a big conundrum of their own. In particular, the modern neutrino physics research revolves around the question of the origin of neutrino masses, which cannot be assigned to neutrinos via the same mechanism that gives all other particles mass (namely the Higgs mechanism). The presence of neutrino masses manifests itself in the observable phenomenon of *neutrino flavour oscillations*, which accompany neutrino propagation through space and time. Discovered on the verge of the 21st century by the Super-Kamiokande and the SNO collaborations [50, 51], these oscillations are now known to affect the propagation of neutrinos regardless of their source[4], whether it be the Sun, supernovae, or a population of extreme astrophysical objects such as blazars. The atmospheric neutrinos – those produced in decays of the air shower mesons and muons – are not an exception to the rule. They span a broad energy range from MeV to PeV and, once produced as a particular flavour (such as the muon neutrino, or ν_μ) in the atmosphere, may end up appearing as a different flavour (such as the tau neutrino, ν_τ, or the electron neutrino, ν_e) when detected at Earth[5]. The precision measurements of neutrino oscillation parameters (related to the frequency and the magnitude of the oscillations) fuel the quest for neutrino mass generation mechanisms [52–54] and are therefore of extreme value to the modern neutrino physics research. As we shall see in Section 0.2, these measurements require extra care when the low-energy ($\mathcal{O}$(GeV) and below) atmospheric neutrinos are used as the main signal, which leads directly to the "spotlight topic" of this thesis – *the precision modelling of low-energy atmospheric neutrino fluxes*.

0.2 THIS WORK IN THE CONTEXT OF MODERN PARTICLE PHYSICS

The probability of neutrino flavour oscillations depends on the neutrino energy as well as the path length travelled from production to detection. In atmospheric neutrino studies, this distance is typically approximated by the cosine of the angle at which neutrino is incident at the detector (the *zenith angle*). Thus, to correctly evaluate the expected count rates of neutrinos post-oscillations under a presumed set of oscillation parameters, accurate modelling of the "unoscillated" neutrino angular distributions is necessary. At $\mathcal{O}$(GeV) and sub-GeV energies, the angular distributions of the air shower

---

[4] The only difference is the frequency of the oscillations, which is driven by the energies accessible at the source and its proximity to the Earth.

[5] We will delay the explanation of the physics of this conversion until Chapter 2.

secondaries are affected by the Earth's magnetic field, which curves the trajectories of the charged cosmic ray primaries and the secondary muons. In addition, the angular spread of the low-energy secondaries about the direction of the primary cosmic ray (e.g. a proton) is large. This is understood from simple kinematical considerations: as the transverse momentum is Lorentz-invariant, its contribution to the total momentum (and therefore the deflection angle) grows with decreasing energy. Both of these effects are necessary to properly describe the angular evolution of atmospheric air showers and the resulting angular distributions of the low-energy atmospheric neutrinos from the full cosmic ray sky.

The most natural approach to incorporate the many stages of the air shower modelling into a single computational framework, including the aforementioned "geometric" effects at low energies, is via the Monte Carlo simulations [55–60]. The Monte Carlo treatment implies that the generation and propagation of the cosmic ray primaries is executed on an event-by-event basis, which also applies to interactions and decays of the secondary particles. While having high precision as a natural advantage, the Monte Carlo approach to atmospheric neutrino flux calculations suffers from computational complexity and lack of flexibility with regards to propagation of systematic uncertainties. An alternative path towards the "unoscillated" atmospheric neutrino flux predictions is via the differential cascade equations describing particle production, interaction, and decay in the atmosphere [1, 61, 62]. The current state-of-the-art software providing high-precision numerical solutions to these equations is the MCEq (Matrix Cascade Equations) code[6] [1, 2]. A fully numerical approach to the particle cascade evolution guarantees a significant speedup over the Monte Carlo codes and the flexibility to study the impact of the systematic parameters. However, prior to this work, the MCEq code could not be readily used to predict the angular distributions of the $\mathcal{O}$(GeV) atmospheric neutrinos. The reason for this constraint was that the original MCEq software was written in the 1D approximation of the air shower geometry development, i.e. under the assumption of the collinear (with respect to the primary cosmic ray axis) secondary particle production and propagation. Such an approximation is justified for neutrino energies above a few GeV, however is not valid at energies of $\mathcal{O}$(GeV) and below, where it results in an underestimation of the near-horizontal neutrino fluxes [63–65].

Given the limitations of the existing methods, this thesis seeks to improve the low-energy atmospheric neutrino flux modelling by extending the MCEq framework with the angular evolution of the atmospheric air showers. To that end, the main goals of this work are:

- To mathematically formulate the cascade theory in two dimensions (longitudinal + angular development);

[6] https://github.com/afedynitch/MCEq

- To develop the methodology for the 2D cascade equations solution in the MCEq framework;
- To build the software with the respective functionality (dubbed the "2D MCEq" cascade equation solver) and make it available for public use [7];
- To benchmark the results obtained with this software (focusing on the fluxes of atmospheric neutrinos and muons) against the existing Monte Carlo codes.

In the broader landscape of particle physics, fulfilling these goals means pushing the field of the air shower modelling to the frontier of computational performance and precision. This work thereby aids the transition from the "brute-force" Monte Carlo codes to fully numerical three-dimensional calculations of atmospheric neutrino fluxes, which is an important milestone for any atmospheric neutrino oscillation analyses sensitive to the $\lesssim \mathcal{O}(\mathrm{GeV})$ neutrino energies. This energy regime is of great relevance to several upcoming experiments such as the IceCube-Upgrade [66], Hyper-Kamiokande [67], KM3NeT/ORCA [68], DUNE [69], and JUNO [70], which will all benefit from the numerical recipes and the practical software solutions developed in this thesis.

[7] https://github.com/kotania/MCEq/tree/2DShow: preliminary version soon to be merged into the main MCEq repository.

I

Background

CHAPTER 1

The Standard Model

This chapter describes the foundations of the Standard Model of particle physics – the most complete encyclopedia of the constituent blocks of matter compiled to date and the most accurate rulebook according to which these constituents have been observed to behave and interact. Starting off with some essential preliminaries in Section 1.1, we will dedicate the remainder of this chapter to the aspects of the Standard Model of prime relevance in the context of this thesis. This includes the phenomenology of hadronic interactions and the production of leptons, which we cover in Sections 1.2 and 1.3, respectively. A more complete introduction to the subject of particle physics can be found in classic textbooks, e.g., [61] and [71–75], which were used as the references for this chapter. The phenomena unexplained in the Standard Model framework at the time of writing, such as the origin of the matter-antimatter asymmetry, the particle nature of dark matter, and the quantization of gravity are summarized in e.g. [76–79] and left outside the scope of this thesis.

1.1 Fields, particles, and forces

The most fundamental objects of Nature are **fields** – continuous entities permeating all of spacetime, such that each spacetime point $x^\mu = \langle t, x, y, z \rangle$ has a specific value $\psi(x^\mu)$ of the field assigned. This value can be a scalar, a vector, or a more exotic object such a spinor[1]. While all three types of fields are found in Nature, the fundamental difference between them is the way they

[1] There are also tensor fields, such as the electromagnetic field tensor $F^{\mu\nu}$, but we will need only scalar, vector, and spinor fields to describe the known particles of the Standard Model.

transform under the Poincaré transformations, which include translations, rotations, and Lorentz boosts. Such coordinate transformations leave the scalar fields unaltered; a less trivial yet familiar example is the transformation of the four-vector fields:

- $a^\mu \to a^\mu + b^\mu$ under translation by a four-vector b^μ;
- $a_\mu \to R^x_{\mu\nu}(\theta) a^\nu$ under rotation about the x-axis by an angle θ;
- $a_\mu \to \Lambda^z_{\mu\nu}(v) a^\nu$ under the boost along the z-axis by velocity $\mathbf{v} = \langle 0, 0, v \rangle$.

$R^x_{\mu\nu}(\theta)$ and $\Lambda^z_{\mu\nu}(v)$ are the usual 4×4 rotation and Lorentz boost matrices, respectively, whose explicit form we provide in Appendix A.1. The spinors obey even less trivial transformation rules under the Poincaré group. Importantly, they come in two fundamental types – the left-chiral spinors ψ_L and the right-chiral spinors ψ_R, both of which are two-component objects[2]. The ψ_L and ψ_R spinors transform identically under rotations but differently under boosts (see Equations (A.3) to (A.5)), and it is this difference that makes them physically distinct. The characteristic feature of the $\psi_\mathrm{L}(\psi_\mathrm{R})$ objects is their transformation into each other under the action of the parity $\mathbb{P}(\mathbf{x} \to -\mathbf{x})$:

$$\begin{aligned} \mathbb{P}[\psi_\mathrm{L}(\langle t, \mathbf{x} \rangle)] &= \psi_\mathrm{L}(\langle t, -\mathbf{x} \rangle) = \psi_\mathrm{R}(\langle t, \mathbf{x} \rangle); \\ \mathbb{P}[\psi_\mathrm{R}(\langle t, \mathbf{x} \rangle)] &= \psi_\mathrm{R}(\langle t, -\mathbf{x} \rangle) = \psi_\mathrm{L}(\langle t, \mathbf{x} \rangle). \end{aligned} \tag{1.1}$$

This mutual mirror-like behaviour between the fundamental spinors is what gives them the name "chiral," i.e., not identical to the original "image" after the parity transformation.

The reason why we introduced these three kinds of fields is that the excitation of a field via external energy input corresponds to the creation of a physical **particle**. In other terms, particles can be viewed as the localizations of the respective field's energy in spacetime. From this angle, the ways in which the different fields transform under the Poincaré group become much more than a mathematical abstraction and translate directly into the physical properties of the particles.

For example, the excitations of the spinor field correspond to the "spin-1/2"[3] particles called **fermions**. In the Standard Model, these encompass quarks and leptons – the elementary particles that make up all of the (visible) matter. A physical fermion is always a superposition of the left-chiral and the right-chiral components[4],

$$\Psi = \begin{pmatrix} \psi_\mathrm{L} \\ \psi_\mathrm{R} \end{pmatrix} \tag{1.2}$$

[2]Following [74], we refrain from calling spinors "vectors" to reserve the name "vectors" only for those objects that transform like four-vectors under Poincaré transformations. Mathematically, however, spinors do exist in the $\mathbb{C}^2$ space.

[3]To say that a particle has spin 1/2 implies that one needs to rotate the respective spinor object by 4π about a given axis to have it return to the original state, as seen from Equation (A.5). The spin-1 (vector) particles need to be rotated only by 2π (as per Equation (A.1)), and the spin-0 (scalar) particles can be rotated by any angle to return to themselves.

[4]Here we wrote the Dirac spinor in the chiral basis; other choices of the basis (such as the mass basis) are also possible.

where Ψ is called a Dirac spinor. Such an object is a solution to the Dirac equation describing the propagation of free fermions in spacetime:

$$i\partial_\mu \gamma^\mu \Psi - m\Psi = 0, \tag{1.3}$$

where m is the fermion mass and γ^μ are the usual "gamma matrices" linking the spacetime derivatives ∂_μ and the four "spinor space" components of Ψ . Neither of ψ_L or ψ_R individually are solutions to Equation (1.3); even if a fermion is prepared in a purely left-chiral state, it will evolve into a superposition of the two states throughout its propagation in spacetime and may eventually be measured as a purely right-chiral state. The rate at which the "flipping" between the two chiralities occurs is related to the fermion mass m (via the phase factor e^{imt}), which is a direct consequence of Equation (1.3). From a deeper physical perspective, the chirality flipping occurs because the fermions are not really fully *free* even when they propagate as single objects in vacuum. The "vacuum" of spacetime is, in fact, still permeated by a scalar ("spin-0") field with a non-zero expectation value, called the **Higgs field**, which couples to all massive fermions throughout their propagation. The strength of the coupling is proportional to the fermion's mass, such that more massive fermions are more likely to interact with the "background" Higgs field. Every such interaction collapses the wavefunction of the physical fermion Ψ into a state of definite (and opposite) chirality; what used to be $(\psi_\mathrm{L}, 0)^\top$ becomes $(0, \psi_\mathrm{R})^\top$, and vice versa. Once right-chiral, the fermion loses the ability to participate in the weak interactions – which is one of the four fundamental classes of interactions provided by Nature (among which three, excluding gravity, make it into the Standard Model).

To explain these three classes of interactions, and the three respective forces that they are mediated by, we shall make an obvious note the fermions can couple not only to the Higgs field, but also to other fermions. The confinement of quarks within protons and neutrons, the annihilation of electrons and positrons into a pair of photons, and the decay of a pion into a pair of leptons are some of the very many examples in which *the strong*, *the electromagnetic*, and *the weak forces* manifest themselves. We will summarize some of their most important properties below, relying on the "library" of elementary particles and force mediators in Figure 1.1 as a visual aid.

The strong force

The strong force governs the interactions of quarks and gluons, which are described within the theory of Quantum Chromodynamics (QCD). The quarks are fermions with fractional electric charge, which come in three "generations":

$$\begin{pmatrix} u \\ d \end{pmatrix}, \begin{pmatrix} c \\ s \end{pmatrix}, \text{and} \begin{pmatrix} t \\ b \end{pmatrix}.$$

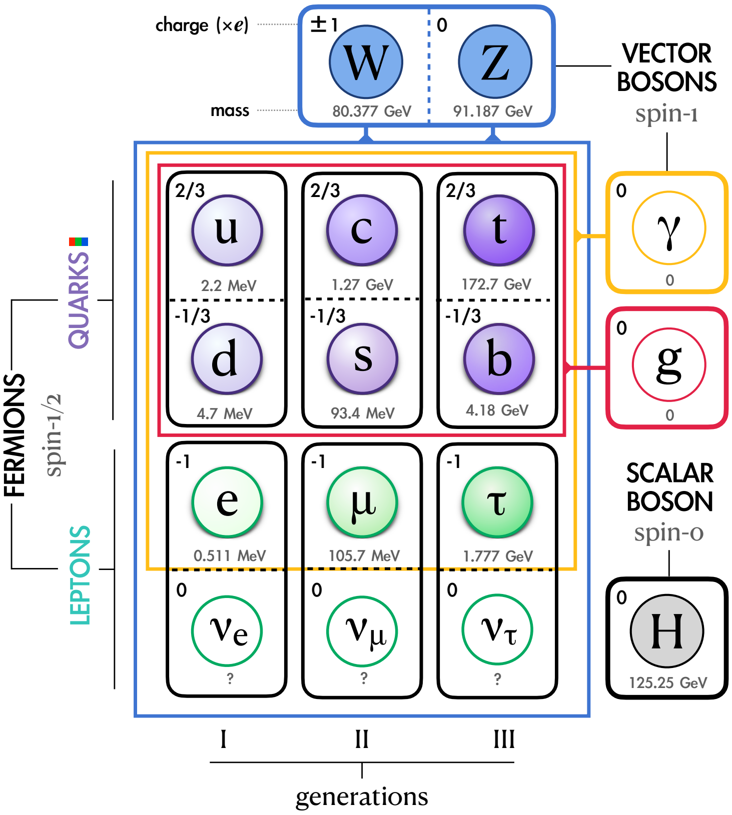

Figure 1.1 – The elementary particles of the Standard Model, including the matter particles (fermions), the force carries (vector bosons), and the Higgs. The antifermions are not included in this figure but can be obtained from the respective fermions via charge conjugation. The listed particle masses correspond to the central fit values from the 2022 edition of the Particle Data Group Review [80].

As per Figure 1.1, the quark generations differ by the mass scale of the quarks; the reason for their arrangement in doublets within each generation (e.g. (u, d)) will become obvious in the context of the weak force. In the context of QCD, the important property of the quarks is their **colour** – a degree of freedom added on top of the "standard" particle properties (such as charge, parity, and spin) to explain the existence of composite particles such as $\Omega^- = |sss\rangle$. Indeed, without any ability to differentiate between the strange (s) quarks in Ω^-, the latter would violate the Pauli exclusion principle by hosting three identical fermions. Thus, three extra "colour labels" are necessary, which are by convention referred to as *red* (r), *green* (g), and *blue* (b).

While important to keep track of the different quarks in composite systems, the colour does not make the quarks physically distinct, and the assignment of colour labels at each individual spacetime point x^μ is arbitrary. For example, a quark q_i at x_i^μ can be defined as a linear superposition of colours r, g, b, while a quark q_j at x_j^μ can be defined in the "coordinate system" $r'g'b'$ rotated with respect to rgb by an arbitrary angle. Locally, the quark physics (i.e., the QCD Lagrangian) remains *invariant* with respect to the choice of the coordinate system. However, to describe the interactions of quarks, one needs to take into account the relative relations between rgb and $r'g'b'$ so that q_i and q_j could enter the interaction on equal footing. This necessitates the existence of an extra vector field – also called a **gauge field** – which connects the two local coordinate systems at x_i^μ and x_j^μ and thereby mediates the interaction between the quarks. In QCD, the gauge field is that of gluons. Accordingly, the gluon itself is a massless **boson** ("spin-1" particle), which also carries the colour charge (conventionally one colour and one anticolour, such as $r\bar{b}$). There exist 8 kinds of gluons, allowing for all permutations of colour and anticolour but typically omitting the colourless state $\propto (r\bar{r} + g\bar{g} + b\bar{b})$. The fact that the gluons carry the colour charge implies that they are prone to self-interactions, which makes the strong force extremely short-range ($\mathcal{O}$(fm)) and confines the quarks within the bound states called **hadrons**.

The local invariance of the strong interactions with respect to the rotations in the abstract colour space of dimension 3 manifests itself as the SU(3) symmetry of QCD[5]. The global symmetries of QCD result in the conservation of the quark flavour (e.g. strangeness or topness), the colour charge, in addition to the electric charge of Quantum Electrodynamics. The flavour conservation in particular implies that the quarks can only be created in quark-antiquark pairs of identical flavour (e.g. $u\bar{u}$) in the strong interactions.

The electromagnetic force

The electromagnetic force mediates the interactions between all charged particles of the Standard Model, i.e., quarks and all leptons but neutrinos. The theory of electromagnetic interactions (Quantum Electrodynamics, or QED) is in many ways similar to QCD. The physics of electromagnetically interacting fermion fields is locally invariant with respect to the multiplication by an arbitrary complex phase, $e^{i\theta(x^\mu)}$, which is referred to as the U(1) symmetry. As in QCD, this local symmetry implies that the phases $\theta(x_i^\mu)$ and $\theta(x_j^\mu)$ need not be equal for $x_i^\mu \neq x_j^\mu$, but a "connecting" gauge field is necessary to keep track of their relative difference and thereby put the interacting fermions on equal footing. In QED, this gauge field is that of the photon – once again a massless boson, which does *not* carry the charge of the QED (the electric charge) and therefore conserves it at interaction vertices. Being electrically neutral, the photon does not self-interact, which makes the electromagnetic

[5] "SU" stands for the "special unitary" group, which imposes unitarity on the complex-valued transformations $\mathbb{M}$ in the group ($\mathbb{M}^\dagger\mathbb{M} = \mathbb{I}$) and demands that $\det \mathbb{M} = 1$.

force *long-range* and lets the colour-neutral fermions avoid the QCD-like confinement.

The weak force

The weak force mediates the interactions between all left-chiral fermions (and right-chiral antifermions) of the Standard Model. The fact that the weak force has a preferred chirality was experimentally determined in the famous ^{60}Co decay experiment by Wu [81] and is nowadays referred to as the **maximal parity violation**. This distinguishes the weak force from the parity-conserving strong and electromagnetic forces. However, the weak interactions are not completely devoid of symmetries; they conserve a property called **flavour**. The three quark and the three lepton generations in Figure 1.1 are grouped by flavour into the **weak iso-doublets**, such that e.g. (u, d) and (c, s) are considered separate flavours/iso-doublets, while u and d belong to the same weak iso-doublet. Similarly, in the lepton sector, (e^-, ν_e) and (μ^-, ν_μ) constitute the doublets of separate flavours, while e^- and ν_e share the same flavour. Just like in QED and QCD, the orientation of the doublet axes at each spacetime point might be arbitrary, which reflects the local SU(2) symmetry. Based on the intuition inherited from QCD and QED, we could expect that this symmetry leads to introduction of a massless gauge boson field – a "connector" keeping track of the coordinate system transformations across spacetime. However, the bosons mediating the weak interactions ($W^\pm$ and Z^0) are *massive*, which reflects the spontaneous breaking of the SU(2) symmetry and implies that we can, in fact, tell the physical difference between the members of each weak iso-doublet (e.g. e^- and ν_e). That the weak interaction mediators are not just massive but also *quite heavy* leads to the strong suppression of the weak force range (by the factor $e^{-M_{W,Z} r}$, where r is distance). Thus the weak force is the shortest-range force in Nature, acting on distance scales $\lesssim \mathcal{O}(10^{-3}\,\text{fm})$.

1.2 ASPECTS OF QUANTUM CHROMODYNAMICS

1.2.1 *Quark-parton model*

As discussed in Section 1.1, the self-interactions of gluons imply that the strong force has an extremely short range and confines the quarks within hadrons – the colourless bound states. Hadrons are further classified into two groups – baryons (made up of 3 quarks of different colours) and mesons (made up of a quark of some colour and an antiquark of the respective anti-colour). For example, a proton ($p = |uud\rangle$) is a baryon, whilst a pion ($\pi^+ = |u\bar{d}\rangle$) is a meson. Only these bound states can be observed in Nature. However, their *parton* (quark and gluon) structure is revealed in high-energy hadronic collisions, where each of the partons acts as an independent scattering center [82–84]. The high-energy regime is thus also referred to as the regime of

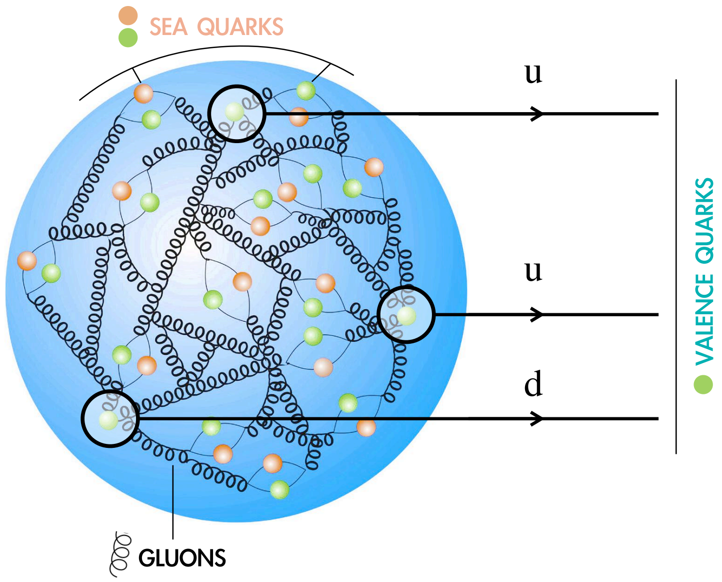

FIGURE 1.2 – The proton structure. *Image credit:* H1 and ZEUS experiments at HERA/DESY. Adapted the DESY press release [85].

an asymptotic freedom, where the quarks need not be treated as confined. The partonic structure of hadrons also includes the *sea quarks* (in addition to the *valence quarks* listed as part of the bound state), which pop in and out of existence as quark-antiquark pairs. To visualize these concepts, we present a schematic illustration of the proton structure in Figure 1.2.

1.2.2 *Hadron-hadron scattering*

In the context of hadronic collisions, an important feature of the quark-parton model is that the partons are allowed to radiate more partons (e.g. via the gluon splitting into a quark-antiquark pair, or through a gluon radiating a gluon). These "offspring" partons can exist only on short distance scales as prescribed by the Heisenberg uncertainty [61]. The scale at which these short-lived "virtual" partons can be resolved is set by the momentum transfer of the interaction; the higher the momentum transfer, the smaller distances can be resolved and the more partons effectively participate in the scattering process. The amplitude of each Feynman diagram contributing to the scattering process is weighted by the QCD coupling constant, α_{QCD}, raised to the power of the diagram's order[6]. Such *perturbative* calculations are possible thanks to the running of α_{QCD} with momentum transfer (Q^2). Indeed, as

[6] The order of the diagram is decided by the number of the virtual particles exchanged.

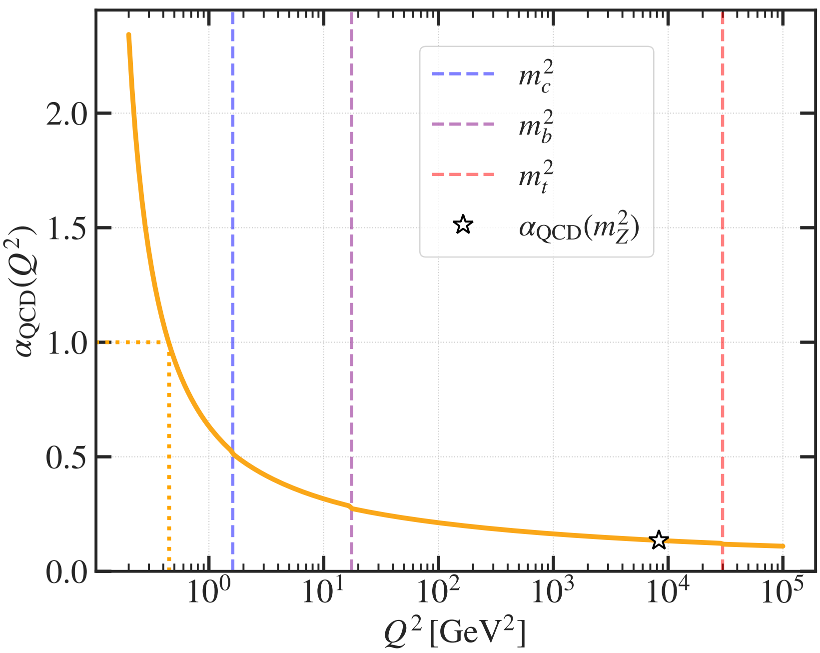

FIGURE 1.3 – The evolution (running) of the QCD coupling constant λ_{QCD} with the momentum transfer Q^2 of the interaction. Here, $\alpha_{\text{QCD}}(Q^2)$ is computed to leading order in perturbation theory from the Renormalization Group Equation, using the quark flavour schemes appropriate for each Q^2 region (bounded by the dashed lines) [80, 86]. To the left of the vertical dotted yellow line, $\alpha_{\text{QCD}} \gtrsim 1$, and the perturbative theory of QCD is no longer applicable.

seen from Figure 1.3, $\alpha_{\text{QCD}} \lesssim 0.1$ above the mass scale of the Z boson (m_Z), and keeps dropping at higher momentum transfers. This regime corresponds to extremely small distances, where the quarks "feel" the dilution of color carried away by the gluons and are not coupled as strongly [86].

The weakening of the QCD coupling at high energies allows one to formulate the total hadron-hadron collision cross section in terms of the cross sections of individual quark-quark scattering processes, which are convolved with the parton distribution functions $f(x, Q^2)$ of the respective quarks. The parton distribution functions describe the probability density of the struck parton momentum relative to the momentum of the primary hadron, which is encoded in the "Bjorken x" variable. The total hadron-hadron cross section then reads:

$$\sigma_{\text{tot}}^{ab\to X} = \sum_{i,j} \int \mathrm{d}x_a \mathrm{d}x_b f_i(x_a, Q^2) f_j(x_b, Q^2) \hat{\sigma}^{ij\to X}(x_a p_a, x_b p_b, Q^2), \tag{1.4}$$

where a, b are the primary hadrons; i, j are the partons participating in the hard scattering; X are the final state particles; x_a and x_b are the fractions of the primary parton momenta p_a and p_b carried away by i and j, respectively; and Q^2 is the momentum transfer of the interaction. The individual parton-parton cross sections, $\hat{\sigma}^{ij\to X}$, can be calculated from the Feynman rules, while the structure functions are obtained from fits to the scattering data[7] (see e.g. [88, 89]). This makes the hadron-hadron cross section straightforward to compute at high energies.

However, moving towards lower energies or momentum transfers, the running of the QCD coupling is no longer a helpful property: already at $Q^2 \sim 0.5\,\text{GeV}^2$, $\alpha_{\text{QCD}} \approx 1$, which makes any perturbative calculations invalid. The regime of low momentum transfer corresponds to large distances, which cannot be treated in the framework of the short-range QCD potentials.

Two predecessor theories of the quark-parton model of hadronic interactions were quite successful in describing the problematic "soft" (low Q^2) hadronic collisions. These are the theories of Regge [90] and Pomeranchuk [91], which were formulated in the late 1950s based on the solutions to the non-relativistic scattering equations and the analytical continuation of the angular momenta in the complex plane. These theories interpret the soft hadron-hadron scattering as the exchange of a *reggeon* and a *pomeron*, respectively. The reggeons correspond to several unflavoured mesons (ρ, a, f, ω), while a pomeron does not have a known corresponding particle. The Regge-Pomeranchuk phenomenology yields the following parametrization of the cross sections in the low-Q^2 processes [92, 93]:

$$\sigma_{\text{tot}}^{ab}(s) = Y^{ab}s^{-\eta} + X^{ab}s^{\varepsilon}, \tag{1.5}$$

where the coefficients Y^{ab} and X^{ab} are specific to the interacting hadrons a, b and $\{-\eta, \epsilon\}$ are global parameters determined from the fits to the hadron-hadron scattering data. The Regge term alone ($Y^{ab}s^{-\eta}$) is sufficient to explain the pp and $p\bar{p}$ scattering data at the center-of-mass energies $\sqrt{s} \lesssim 10\,\text{GeV}$[8], while the Pomeron term ($X^{ab}s^{\varepsilon}$) is necessary to describe the rise of the $\sigma(s)$ curve at higher energies [92].

To accurately reflect both low-Q^2 and high-Q^2 physics in practical calculations, typical Monte Carlo implementations (**event generators**) of hadronic interactions transition between the Regge-Pomeron parametrization of the cross sections and the perturbative QCD calculations of hard scattering processes in the quark-parton model. This is supplemented with extension of the hadron-hadron collisions to the hadron-nucleus collisions via e.g. the Glauber multiple scattering formalism [94], while the final hadronization of the scattered partons back into bound states is normally handled via the Lund string fragmentation model [95].

[7] If the measurements were performed at a different Q^2 scale, the parton distribution functions can also be evolved to the Q^2 scale of interest via the DGLAP equations [87].

[8] s is a Mandelstam variable; in a $1+2 \to 3+4$ scattering process, $s = (p_1^\mu + p_2^\mu)^2 = (p_3^\mu + p_4^\mu)^2$.

1.3 ASPECTS OF THE ELECTROWEAK THEORY

1.3.1 *Pion decay*

High-energy hadron collisions at particle colliders and cosmic ray-nucleus interactions in the atmosphere are accompanied by production of secondary particles, including the charged pions $\pi^{\pm}$. The subsequent re-interactions and decays of $\pi^{\pm}$ play a crucial role in the evolution of hadronic cascades. Being a light meson, the pion cannot decay strongly; the main weak decay modes of π^- include $\pi^- \to \mu^-\bar{\nu}_\mu$ ($\hat{\Gamma}_1 = 0.99987$), $\pi^- \to \mu^-\bar{\nu}_\mu\gamma$ ($\hat{\Gamma}_2 = 2\times10^{-4}$), and $\pi^- \to e^-\bar{\nu}_e$ ($\hat{\Gamma}_3 = 1.23\times10^{-4}$), where $\hat{\Gamma}_i$ are the branching ratios [80]. The two-body decay to a muon and a muon antineutrino (alternatively, to an antimuon and a muon neutrino in the case of π^+) is therefore one of the main means of muon neutrino production in air showers. Electron (anti)neutrinos, on the other hand, appear from the pion decay extremely rarely, and come predominantly from the three-body decays of kaons ($K^- \to \pi^0 e^-\bar{\nu}_e$, $\hat{\Gamma} \simeq 0.05$) and muons ($\mu^- \to e^-\bar{\nu}_e\nu_\mu, \hat{\Gamma} \simeq 1$).

The reason why the $\pi^- \to e^-\bar{\nu}_e$ decay is heavily suppressed compared to $\pi^- \to \mu^-\bar{\nu}_\mu$ is the violation of parity in the weak interactions. Specifically, the W^- mediating the π^- decay can couple only to the left-chiral fermions (u_L) and the right-chiral antifermions (v_R). However, as discussed earlier in Section 1.1, the chiral eigenstates are not the eigenstates of the Dirac equation (Equation (1.3)), i.e., they do not correspond to physical fermions propagating in spacetime. The physical fermions are eigenstates of the **helicity operator**, $\hat{h}$, defined as

$$\hat{h} = \frac{\hat{\mathbf{S}}\cdot\hat{\mathbf{p}}}{p}, \tag{1.6}$$

where $\hat{\mathbf{S}}$ is the spin operator, $\hat{\mathbf{p}}$ is the momentum operator, and p is the magnitude of the fermion three-momentum. The eigenstates of $\hat{h}$ are the right-helical (**right-handed**) state $u_\uparrow$ and the left-helical (**left-handed**) state $u_\downarrow$, which correspond to the fermion spin $\mathbf{s}$ being completely aligned or anti-aligned with the momentum $\mathbf{p}$, respectively. In general, $u_\uparrow$ and $u_\downarrow$ are superpositions of the right-chiral and the left-chiral states. For example, $u_\uparrow$ can be expressed in terms of u_L and u_R as follows [71]:

$$u_\uparrow = \frac{1}{2}\left(1 + \frac{p}{E+m}\right)u_\mathrm{R} + \frac{1}{2}\left(1 - \frac{p}{E+m}\right)u_\mathrm{L}, \tag{1.7}$$

where m, p, E are the mass, the three-momentum magnitude, and the energy of the fermion, respectively. In the ultrarelativistic limit, where $E \gg m$ and $p \approx E$, we find that $u_\uparrow \approx u_\mathrm{R}$, i.e., the fundamental right-chiral eigenstate of the weak interaction and the right-handed eigenstate of the helicity operator become equivalent. An analogous correspondence is acquired for $u_\downarrow$ and u_L. This implies that in the ultrarelativistic (massless) limit, the right-handed

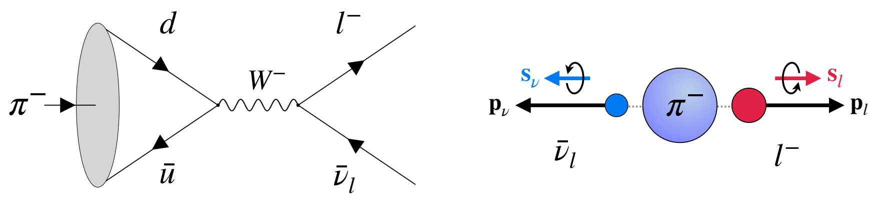

FIGURE 1.4 – The decay of $\pi^- = |\bar{u}d\rangle$, represented as a Feynman diagram (left) and a schematic illustration in the pion rest frame (right). In the left panel, the "blob" alongside the incoming π^- indicates that the pion is a bound state. In the right panel, the black arrows represent the directions of the outgoing lepton momenta, and the coloured arrows – the spin directions under the assumption of a massless neutrino.

fermions and the left-handed antifermions are *disfavoured* by the weak interactions, since they almost completely lack the necessary left-chiral/right-chiral component. On the other hand, the left-handed fermions/right-handed antifermions are almost exclusively left-chiral/right-chiral at high energies, and are therefore preferred.

This picture, applied in the context of pion decay, explains the *helicity suppression* of $\pi^- \to e^-\bar{\nu}_e$. In Figure 1.4, we show the Feynman diagram of the π^- decay to a generic lepton pair ($l^-\bar{\nu}_l$) and the respective spin/momentum assignments in the pion rest frame. The conservation of linear momentum dictates that $\mathbf{p}_\nu = -\mathbf{p}_l$. Since the neutrino is almost massless, the ultra-relativistic limit applies, where the right-chiral antineutrino is always right-handed. This implies that $\mathbf{s}_\nu \uparrow\uparrow \mathbf{p}_l$. Furthermore, π^- is a scalar (spin-0) particle, and the conservation of the total angular momentum demands that $\mathbf{s}_\nu = -\mathbf{s}_l$. The spin and the momentum of the lepton l^- are therefore aligned, too, and l^- emerges from the decay as right-handed. In the above discussion, we have shown that right-handed fermions cannot couple to the weak force unless they are sufficiently massive. The electron, with $m_e \simeq 511\,\text{keV}$, is *effectively* massless and therefore $u_\uparrow(e^-)$ almost completely lacks the left-chiral component $u_\text{L}(e^-)$ necessary to couple to W^-. On the other hand, the muon is nearly 200 times as massive ($m_\mu \simeq 105.7\,\text{MeV}$), and $u_\uparrow(\mu^-)$ has a sufficient contribution from $u_\text{L}(\mu^-)$. Thus, the decay $\pi^- \to \mu^-\bar{\nu}_\mu$ can proceed, providing a source of muon neutrinos in the decays of atmospheric pions.

An important consequence of the above discussion is that the muons (μ^-) always emerge as right-handed in the rest frame of the decaying π^-. A similar argument applies to the decay of π^+, which produces exclusively left-handed μ^+ in the π^+ rest frame. This phenomenon is referred to as **muon polarization**. However, the eigenvalue of the helicity operator $\hbar$, i.e., the helicity itself, is not a Lorentz-invariant quantity:

$$h = \frac{\mathbf{s} \cdot \mathbf{p}}{|\mathbf{p}|}, \tag{1.8}$$

since the three-vectors $\mathbf{s}$ and $\mathbf{p}$ (i.e. the spatial components of the respective four-vectors s^μ and p^μ) both transform under boosts[9]. This means that in the frame of a boosted pion (i.e. the lab frame), the muon can have either either a positive or a negative helicity with a certain probability. In a scenario where the pion moves with a velocity v_π along the z-axis (such that its Lorentz velocity factor $\beta_\pi = v_\pi/c \equiv v_\pi$ in the natural units) and the emitted muon makes an angle θ^* with the z-axis in the pion rest frame, the lab-frame helicity of the muon reads [96]:

$$h_{\text{lab}}(\beta_\pi, \theta^*) = \frac{1}{\beta_\mu} \cdot \frac{(1 - r_\pi) + (1 + r_\pi)\cos\theta^* \beta_\pi}{(1 + r_\pi) + (1 - r_\pi)\cos\theta^* \beta_\pi}, \tag{1.9}$$

where β_μ is the muon velocity in the lab frame and $r_\pi = (m_\mu/m_\pi)^2$. The helicity in the boosted frame is no longer restricted to ± 1 (in our choice of normalization) and can take values in the continuous -1..1 range. In practice, the spin states of individual muons are often not important and only the average behaviour of a muon population is of interest[10]. It is then convenient to model the muon ensemble as a superposition of purely right-randed muons ($\mu^-_\uparrow$ with $h = +1$) and purely left-handed muons ($\mu^-_\downarrow$ with $h = -1$), appearing with probabilities $\mathcal{P}_\uparrow$ and $\mathcal{P}_\downarrow$, respectively. Expressed in terms of h_{lab}, these probabilities are

$$\mathcal{P}_{\uparrow,\downarrow}(\beta_\pi, \theta^*) = \frac{1}{2}\left[1 \pm h_{\text{lab}}(\beta_\pi, \theta^*)\right], \tag{1.10}$$

where "+" corresponds to the $\mu^-_\uparrow$ state and "-" – to the $\mu^-_\downarrow$ state [96]. For μ^+, the correspondence between the right-/left-handedness and the +/- sign in Equation (1.10) is flipped. The same formalism applies to the two-body decays of charged kaons, $K^\pm$, replacing β_π with β_K and r_π with $r_K = (m_\mu/m_K)^2$.

1.3.2 *Muon decay*

In Section 1.3.1, we established that muons emerging from the two-body decays of $\pi^\pm$ and $K^\pm$ are completely polarized in the rest frame of the decaying mesons. In the lab frame, the asymmetry in the orientation of the muon spin with respect to its momentum remains. The muon polarization has an important consequence for the spectra and the angular distributions of the $\mu^- \to e^- \bar{\nu}_e \nu_\mu$ decay secondaries, which is best illustrated with the following example.

---

9 In the definition of h in Equation (1.8), we implicitly assume that $\mathbf{s}$ is a unit vector and therefore do not include its magnitude in the denominator. However, we note that the spin operator eigenvalues are quantized and are necessarily integer multiples of $\hbar/2$.

10 This concerns, in particular, the modelling of muon fluxes in cascade equations.

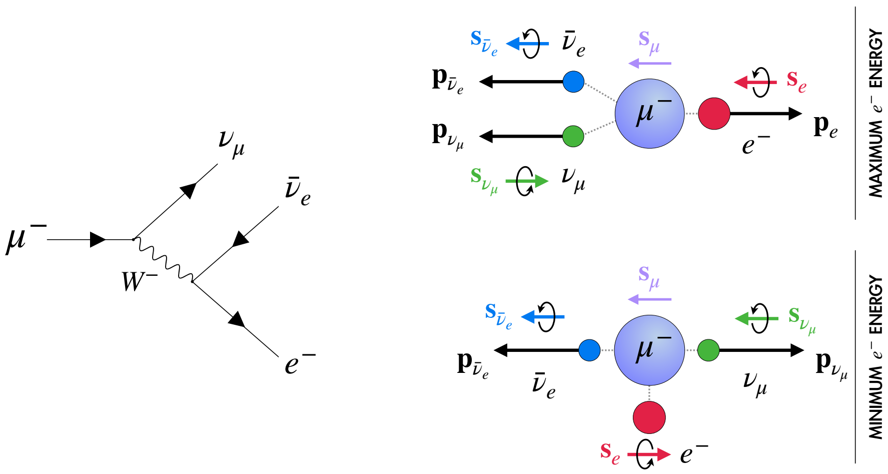

FIGURE 1.5 – The three-body muon decay ($\mu^- \to e^- \bar{\nu}_e \nu_\mu$), represented as a Feynman diagram (left) and a schematic illustration in the muon rest frame (right). The arrows in the right panel are coloured in the same way as in Figure 1.4. The two spin assignment choices correspond to the edge cases of the maximum (top) and the minimum (bottom) electron energies.

Let's assume a μ^- decaying at rest, with its spin unit vector pointing along the direction of the negative z-axis ($\mathbf{s}_\mu = \langle 0, 0, -1 \rangle$). The Feynman diagram of the muon decay is shown in the left panel of Figure 1.5. From here, two regions of the electron energy distribution are instructive to examine: the regime where the electron energy is maximal and where the electron is practically at rest. In the first case (which corresponds to $E_e^* = E_{e,\max}^* = m_\mu/2$ in the muon rest frame), the two neutrinos are emitted collinearly in the direction opposite to that of the electron. In the limit of massless neutrinos, $\bar{\nu}_e$ must be right-handed, and ν_μ must be left-handed; thus, $\mathbf{s}_{\bar{\nu}_e} \uparrow\uparrow \mathbf{p}_{\bar{\nu}_e}$, and $\mathbf{s}_{\nu_\mu} \downarrow\uparrow \mathbf{p}_{\nu_\mu}$. It follows that the spins of the neutrinos are anti-parallel and cancel each other out, meaning that the spin of the electron has to be oriented in the same way as the spin of the muon to preserve angular momentum. Thus, we find that $\mathbf{s}_e \downarrow\uparrow \mathbf{p}_e$, i.e., the emitted electron is left-handed at the maximum allowed energy. This corresponds to our intuition that the fermions emerging from weak decays should be preferentially left-handed, and we can therefore expect the electron energy distribution to be peaking at $E_{e,\max}^*$. In the second edge case (where $E_e^* \simeq m_e$), the electron is nearly still, and the muon's rest energy is split between the two neutrinos emitted back to back. The handedness assignments for neutrinos do not change, and now their spins are pointing in the same direction. To compensate for this and recover muon's original spin vector, the electron spin direction must be opposite to that of neutrinos. Once

	$f_0(x)$	$f_1(x)$
$\bar{\nu}_\mu(\nu_\mu)$, $e^+(e^-)$	$2x^2(3-2x)$	$2x^2(1-2x)$
$\nu_e(\bar{\nu}_e)$	$12x^2(1-x)$	$12x^2(1-x)$

Table 1.1 – Energy-dependent coefficients for the polarized muon decay spectra in Equation (1.11). The secondaries outside (inside) the parentheses correspond to the decay of $\mu^+(\mu^-)$.

again remembering that the left-handed fermions are preferred by the weak interaction, we arrive at a preferred orientation of the electron momentum at low energies – which is parallel to the direction of the muon spin.

Since ν_μ is also left-handed, it will follow the same asymmetry in the angle-energy distributions as the electron, while for $\bar{\nu}_e$ the qualitative picture is reversed. Quantitatively, the double-differential spectra of the $\mu^\pm$ decay secondaries read [97]:

$$\frac{\mathrm{d}^2 N_l}{\mathrm{d}x \mathrm{d}\cos\alpha} = f_0 \mp f_1(x)\cos\alpha, \tag{1.11}$$

where α is the angle between the muon spin and the momentum of the outgoing lepton l ($\cos\alpha = \mathbf{s}_\mu \cdot \mathbf{p}_l/|\mathbf{p}_l| \equiv \mathbf{s}_\mu \cdot \hat{\mathbf{p}}_l$), x is the lepton energy fraction ($x = 2E_l^*/m_\mu$, with E_l^* being the lepton energy in the muon rest frame), and $f_i(x)$ are the functions defined in Table 1.1. In Figure 1.6, we show these double-differential distributions for the daughters of μ^-. As expected from the qualitative analysis of the two extreme cases, the left-handed daughters are preferentially emitted in the direction opposite to that of the muon spin ($\cos\alpha \simeq -1$), and the right-handed ones (in this case $\bar{\nu}_e$) – in the direction aligned with the muon spin ($\cos\alpha \simeq 1$). In Section 5.2.3, we will see how muon polarization affects the angular distributions and the energy spectra of the daughters in the lab at the muon energies of interest for this work.

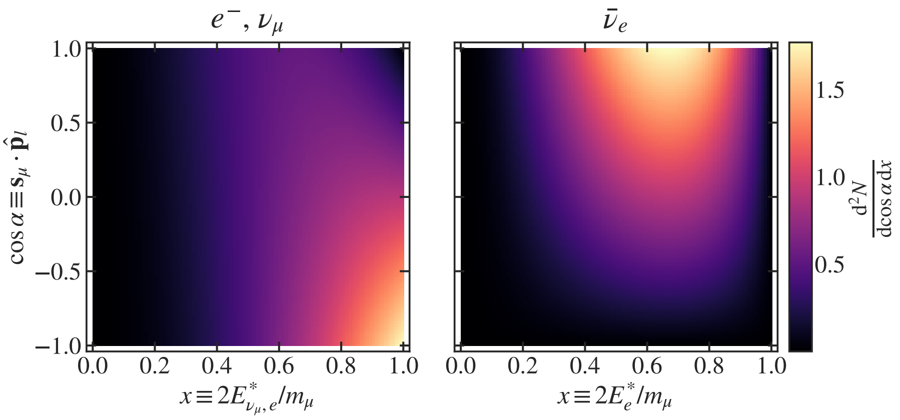

Figure 1.6 – The double-differential spectra of the $\mu^- \to e^-\bar{\nu}_e\nu_\mu$ decay daughters in the μ^- rest frame, as predicted by Equation (1.11) (see also [96, 97]).

CHAPTER 2

Neutrinos

In Section 1.1, we talked about neutrinos as members of the weak iso-doublets of the Standard Model; separately, Sections 1.3.1 and 1.3.2 covered their creation in the decays of a pion and a muon, respectively. However, the properties of neutrinos on their own deserve a closer look, in particular when it comes to the phenomenon of neutrino flavour oscillations and its apparent inconsistency with the Standard Model. In this chapter, we will cover the phenomenology of neutrino flavour and mixing (Section 2.1), highlighting the role of atmospheric neutrinos in constraining neutrino oscillation parameters. Section 2.2 will then give an overview of atmospheric neutrino production, detection, and oscillations, and explain how the different choices of atmospheric neutrino flux modelling approaches can affect the oscillation measurements.

2.1 Neutrinos in the Standard Model (and beyond)

In the Standard Model, neutrinos are neutral leptons which appear in three flavours: ν_e, ν_μ, and ν_τ, one for each corresponding charged lepton (e, μ, and τ). The $|\nu_e\rangle$, $|\nu_\mu\rangle$, and $|\nu_\tau\rangle$ particle states are known to only couple to the weak force[1] and are therefore necessarily left-chiral (see Section 1.1). Accordingly, the respective weak eigenstates for antineutrinos ($|\bar{\nu}_e\rangle$, $|\bar{\nu}_\mu\rangle$, $|\bar{\nu}_\tau\rangle$) are exclusively right-chiral. An important twist to the story is the 1958 experiment by Goldhaber, Grodzins, and Sunyar, who measured the ν_e helicity of in the $^{152\mathrm{m}}$Eu decay [98]:

$$^{152\mathrm{m}}\mathrm{Eu} + e^- \rightarrow {}^{152}\mathrm{Sm}^* + \nu_e \rightarrow {}^{152}\mathrm{Sm} + \nu_e + \gamma \qquad (2.1)$$

[1] Besides gravity, which neutrinos can still couple to as they are not completely massless.

Group	Year	Flavour	Process	h_ν ± unc.	Ref.
Golhaber *et al.*	1958	ν_e	$^{152\mathrm{m}}\mathrm{Eu} + e^- \to$ $^{152}\mathrm{Sm} + \nu_e + \gamma$	-1.0 ± 0.2	[98]
Roesch *et al.*	1982	ν_μ	$^{12}\mathrm{C} + \mu^- \to$ $^{12}\mathrm{B} + \nu_\mu$	-1.06 ± 0.11	[99]
ALEPH	1994	ν_τ	$e^+e^- \to \tau^+\tau^- \to$ $\pi^-\nu_\tau, \rho^-\nu_\tau$	$-0.99 \pm 0.07 \pm 0.04$	[100]
ALEPH	1995	ν_τ	$e^+e^- \to \tau^+\tau^- \to$ $\pi^-\nu_\tau, \rho^-\nu_\tau$	$-1.006 \pm 0.032 \pm 0.019$	[101]
CLEO	1997	ν_τ	$e^+e^- \to \tau^+\tau^- \to$ $\pi^+\pi_0\bar{\nu}_\tau(\pi^-\pi_0\nu_\tau)$	$-0.995 \pm 0.01 \pm 0.003$	[102]
SLD	1997	ν_τ	$e^+e^- \to \tau^+\tau^- \to$ $\pi^-\nu_\tau, \rho^-\nu_\tau$	$-0.93 \pm 0.10 \pm 0.04$	[103]

Table 2.1 – A summary of the direct neutrino helicity measurements.

The result of the measurement was that the neutrino was left-handed ($h \simeq -1$), with about 20% experimental uncertainty. Several more experiments for direct helicity measurements of neutrinos followed, with their summary given in Table 2.1. As is apparent from the measurements of all flavours, the neutrino seems to have left-handed helicity, in both Goldhaber-like experiments (such as [99]) and polarized τ decays (such as [100–103]). Now, as we have shown in Section 1.3.1, in particular Equation (1.7), the helicity eigenstates are only equivalent to the chiral eigenstates in the ultrarelativistic (massless) limit, thereby hinting at the masslessness of neutrinos. The direct measurements of neutrino mass from the electron spectrum endpoint in the tritium decay,

$$^3_1\mathrm{H} \to ^3_2\mathrm{He} + e^- + \bar{\nu}_e, \tag{2.2}$$

are providing an independent constraint on the (electron-based) upper mass limit, which improved from 1.7 keV in 1948 [104] to 0.1 eV in 2022 (by the KATRIN experiment at the 90% confidence level; see [80, 105]). A comprehensive review on direct neutrino mass measurements can be found in [106]. Another set of upper bounds is provided through cosmological observations, which yield the limit of about $\sum m_\nu \lesssim 0.1\,\mathrm{eV}$ (at the 95% confidence level) on the sum of the "active" ($\nu_{e,\mu,\tau}$) state masses in the ΛCDM cosmology [80, 107–109].

The results of the neutrino mass measurements combined with the measurements of helicity point to the fact that neutrinos must be *very* light – more than 10^6 times lighter than the next lightest elementary particle, the electron.

But are they *truly massless*? It is nowadays known that this is not the case, as each of the weak eigenstates $|\nu_\alpha\rangle$ ($\alpha = \{e, \mu, \tau\}$) is a superposition of three distinct mass eigenstates, $|\nu_i\rangle$ ($i = \{1, 2, 3\}$). The mass eigenstates $|\nu_i\rangle$ are the "physical" eigenstates of the free-particle Hamiltonian, which satisfy the Dirac equation (1.3) and thus describe a neutrino propagating in spacetime. This is contrasted with the chiral neutrino eigenstates $|\nu_\alpha\rangle$, which couple to the weak force and are only "physical" at production or detection. $|\nu_\alpha\rangle$ and $|\nu_i\rangle$ are related via the unitary[2] **mixing matrix** U:

$$|\nu_\alpha\rangle = \sum_i U^*_{\alpha i}|\nu_i\rangle, \tag{2.3}$$

where the unitarity implies that $U^\dagger U = UU^\dagger = \mathbb{I}$, i.e., that the inverse of U is also its Hermitian conjugate ($U^{-1} = U^\dagger \equiv (U^*)^\top$). Given a state $|\nu_\alpha\rangle$ produced in a weak interaction, the probability to measure a (possibly different) state ν_β after a neutrino with energy E has travelled a distance L is [73]:

$$\begin{aligned} P_{\alpha\to\beta} = \left|\langle\nu_\beta|\nu_\alpha\rangle\right|^2 = \delta_{\alpha\beta} - 4\sum_{i<j}\mathfrak{Re}(U^*_{\alpha i}U_{\beta_i}U_{\alpha j}U^*_{\beta j})\sin^2\left(\frac{\Delta m^2_{ij}L}{4E}\right) \\ + 2\sum_{i<j}\mathfrak{Im}(U^*_{\alpha i}U_{\beta_i}U_{\alpha j}U^*_{\beta j})\sin^2\left(\frac{\Delta m^2_{ij}L}{4E}\right), \end{aligned} \tag{2.4}$$

where

$$\Delta m^2_{ij} = m^2_i - m^2_j \tag{2.5}$$

is the **mass splitting** between the state $|\nu_i\rangle$ with a definite mass m_i and the state $|\nu_j\rangle$ with a definite mass m_j. For antineutrinos, the sign of the last term ($2\sum_{i<j}\mathfrak{Im}\ldots$) is reversed. Importantly, if the neutrinos were massless, we would have $m_i = m_j$ for all i, j, and the oscillation amplitude would always be 0 – which is in contradiction with numerous modern experiments (for a review, see [80, 110]). This creates tension with the Standard Model, where only left-chiral neutrino fields exist and the right-chiral counterpart is necessary to generate neutrino masses via the Higgs mechanism [111].

To simplify Equation (2.4), the mixing matrix U is often parametrized in terms of the three rotation matrices R_{23}, R_{13}, and R_{12}:

$$U = R_{23}R_{13}R_{12} \equiv \begin{pmatrix} 1 & 0 & 0 \\ 0 & c_{23} & s_{23} \\ 0 & -s_{23} & c_{23} \end{pmatrix}\begin{pmatrix} c_{13} & 0 & s_{13}e^{-i\delta} \\ 0 & 1 & 0 \\ -s_{13}e^{i\delta} & 0 & c_{13} \end{pmatrix}\begin{pmatrix} c_{12} & s_{12} & 0 \\ -s_{12} & c_{12} & 0 \\ 0 & 0 & 1 \end{pmatrix}, \tag{2.6}$$

[2]The unitarity of the mixing matrix is an assumption of the Standard Model.

where δ is a (physical) complex phase[3], $c_{ij} \equiv \cos\theta_{ij}$, $s_{ij} \equiv \sin\theta_{ij}$, and θ_{ij} is the **mixing angle** between eigenstates i and j. The physical meaning of the mixing angles is revealed in the two-flavour approximation, where only flavours α and β (and no other flavour $\gamma \notin \{\alpha, \beta\}$) exist. In this scenario, the probability to *oscillate* from $|\nu_\alpha\rangle$ to $|\nu_\beta\rangle$ is

$$P^{2\,\text{flav.}}_{\alpha\to\beta,\alpha\neq\beta} = \sin^2(2\theta_{ij})\sin^2\left(\frac{\Delta m^2_{ij} L}{4E}\right), \tag{2.7}$$

where i, j are now simply $1, 2$, respectively. Equation (2.7) makes it transparent that the mass splittings Δm^2_{ij} control the frequency of neutrino oscillations as a function of L/E, while the mixing angles θ_{ij} control the oscillation amplitude. We note that the "frequency term" is commonly rewritten in the convenient units of baseline length L and energy E:

$$\sin^2\left(\frac{\Delta m^2_{ij} L}{4E}\right) \longrightarrow \sin^2\left(\frac{1.27\Delta m^2_{ij}\,(\mathrm{eV}^2)\,L\,(\mathrm{km})}{E\,(\mathrm{GeV})}\right) \tag{2.8}$$

The baseline length L and the energy E are specific to the source of neutrinos and the type of detector measuring the oscillations, such that the different L, E combinations allow one to probe different parts of the Δm_{ij} and θ_{ij} parameter space. The rotation matrices R_{ij} are for that reason sometimes called after the respective type of experiment: R_{12} is conventionally referred to as the *solar* matrix (probing the oscillations of ν_e produced in the nuclear fusion reactions in the Sun); R_{13} – as the *reactor* matrix (probing the oscillations of $\bar{\nu}_e$ from the β^- decays of unstable isotopes in nuclear reactors); and R_{23} – as the *atmospheric* matrix (probing the oscillations of atmospheric neutrinos originating from the cosmic ray-induced air showers). As a transition to a more detailed discussion on the latter, which we provide in Section 2.2, we illustrate the phenomenon of neutrino oscillations at three characteristic atmospheric neutrino energies – 2, 10, and 100 GeV – in Figure 2.1.

2.2 ATMOSPHERIC NEUTRINO FLUXES AND OSCILLATIONS

The Earth's atmosphere is constantly bombarded by cosmic rays[4], whose collisions with the atmospheric nuclei induce **atmospheric air showers**. As shown schematically in Figure 2.2, neutrinos are one of the byproducts of the cosmic ray interactions, where they originate primarily in decays of light mesons and muons (as described in Section 1.3.1 and Section 1.3.2, respectively). On their

[3] Also called the Dirac phase, which we by convention incorporated into R_{13}. The Majorana phases, which do not affect neutrino oscillations, are not included.

[4] In Chapter 0, we have provided the historical evidence for cosmic rays being composed of predominantly protons; a modern view on cosmic ray composition and flux can be found in e.g. [114, 115].

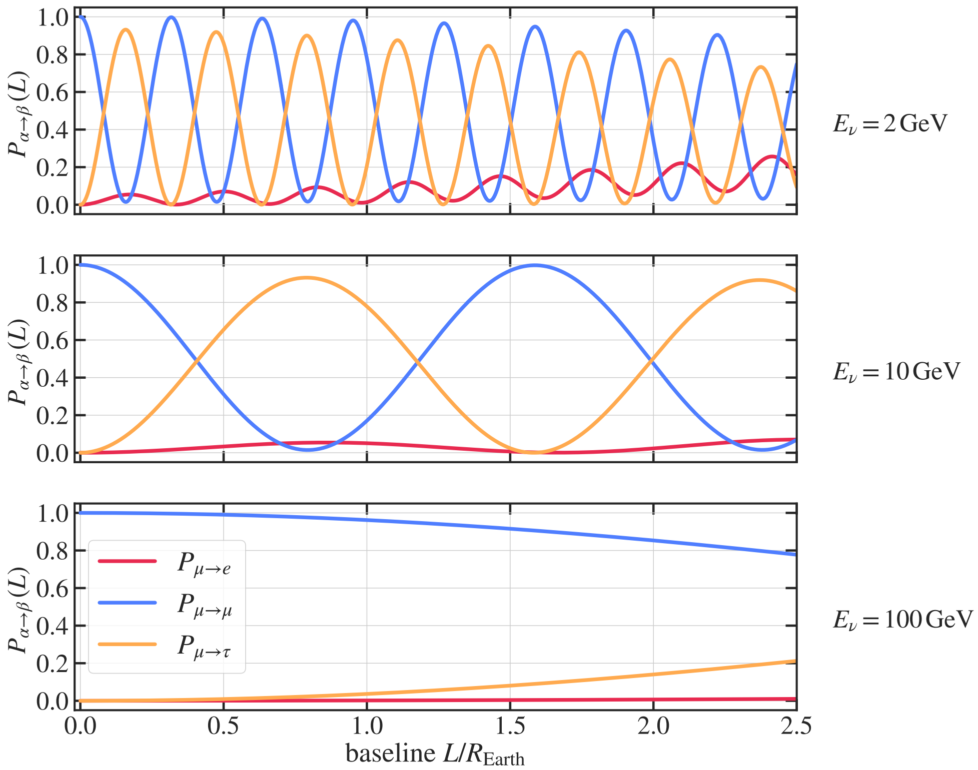

FIGURE 2.1 – The probability of ν_μ oscillation into ν_e (red), ν_τ (orange), as well as its survival as ν_μ (blue), shown at three characteristic energies of atmospheric neutrinos. The oscillation probabilities were computed in the full three-flavour scheme using the NuOscProbExact software [112]. The oscillation parameters follow NuFit 5.1 (2021) [113], assuming normal ordering of the mass states.

way to a terrestrial detector, neutrinos can cross the entire Earth unimpeded, modulo the Earth absorption effects at energies $\gtrsim 40\,\text{TeV}$ [117] and the flavour oscillations. From Figure 2.1, we can see that for a neutrino produced as a ν_μ flavour state, the probability of being detected in the same state after crossing $L = 2R_{\text{Earth}}$ is $\gtrsim 0.8$ for $100\,\text{GeV}$ neutrinos but only about $\sim$0.5 at neutrino energies of 2 and $10\,\text{GeV}$. This is reflected in the increased *tau neutrino appearance* probability, which is $\lesssim 0.2$ for the high-energy neutrinos and $\sim$0.5 for the low-energy neutrinos in our example. Therefore, to measure the neutrino oscillation parameters from the neutrino flavour composition observed at Earth, it is crucial to accurately predict how many neutrinos within each energy band are expected from the cosmic ray interactions *prior* to oscillations. This is represented by the quantity called the **neutrino flux**,

$$\Phi_\nu(E,\Omega) = \frac{\mathrm{d}N}{\mathrm{d}E\,\mathrm{d}A\,\mathrm{d}t\,\mathrm{d}\Omega}, \tag{2.9}$$

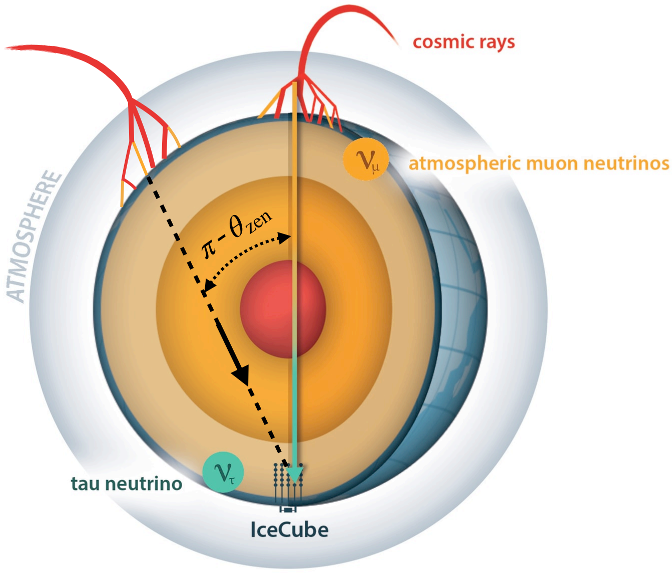

FIGURE 2.2 – Production of atmospheric neutrinos followed by propagation towards a terrestrial detector (in this case using the IceCube Neutrino Observatory at the South Pole as an example) in the direction defined by the zenith angle θ_{zen}. *Image credit*: The IceCube Collaboration. Adapted from the IceCube press release [116].

i.e., the energy spectrum $\mathrm{d}N/\mathrm{d}E$ of neutrinos produced per unit area A, unit time t, and solid angle Ω as viewed from the detector. In spherical coordinates, the unit solid angle is $\mathrm{d}\Omega = \mathrm{d}\cos\theta_{\text{zen}}\mathrm{d}\varphi$, where θ_{zen} is the **zenith angle** (as defined by the orientation of the neutrino arrival direction relative to the detector axis; see Figure 2.2), and φ is the respective azimuthal angle. The latter is only sensitive to the local geomagnetic field effects (i.e. the curving of the charged cosmic ray primary and secondary trajectories in the magnetic field of the Earth), which are near-negligible in high-energy ($\gtrsim \mathcal{O}(10\,\text{GeV})$) neutrino flux calculations [63]. Averaging over the azimuthal angle, the neutrino flux becomes a function of only E and $\cos\theta_{\text{zen}}$. We show the $\cos\theta_{\text{zen}}$ dependence of the $\nu_\mu + \bar{\nu}_\mu$ and $\nu_e + \bar{\nu}_e$ fluxes in Figure 2.3, fixing the neutrino energies at the same three values as in Figure 2.1. We additionally show the $\cos\theta_{\text{zen}}$-averaged fluxes as a function of energy in Figure 2.4.

There are several relevant observations to be made from the two figures:

- In both the zenith-averaged and the zenith-dependent plot, only the ν_e and ν_μ flavour fluxes are shown, as the ν_τ flux is negligibly small across the chosen energy range. This is related to the fact that in the air showers, ν_τ are only generated in the decays of the tau lepton (τ) and the charged mesons ($D^\pm$, D^0, and D_s). Both τ and the D-mesons are relatively heavy ($m_\tau \approx 1.78\,\text{GeV}$, $m_D \approx 1.9\,\text{GeV}$) and require more

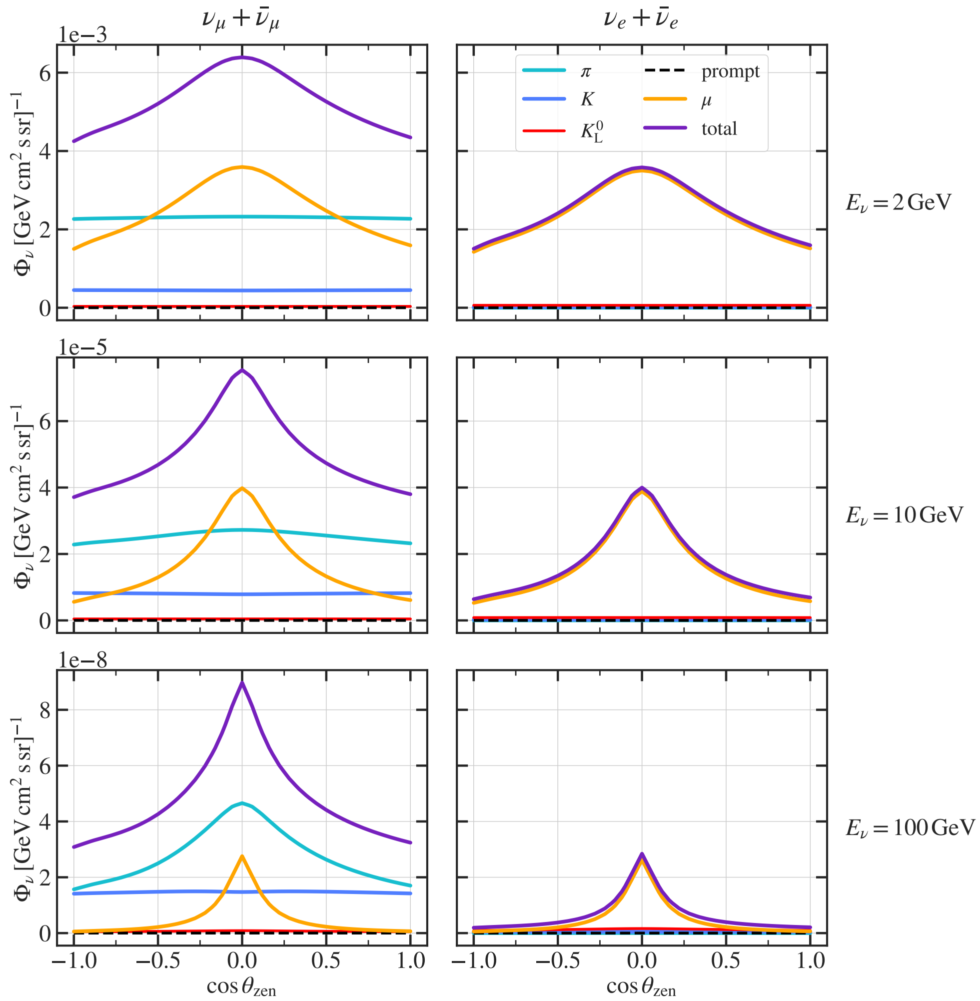

Figure 2.3 – $\cos\theta_{\mathrm{zen}}$ dependence of the atmospheric neutrino fluxes at three fixed energies. The fluxes were computed via the (1D) MCEq software [1, 2], using the DPMJet-III 19.1 hadronic interaction model [62], Global Spline Fit cosmic ray flux [114], and the NRLMSISE-00 atmosphere for the South Pole in January [118]. The different coloured lines highlight the contributions of the different neutrino parents to the total flux (solid purple).

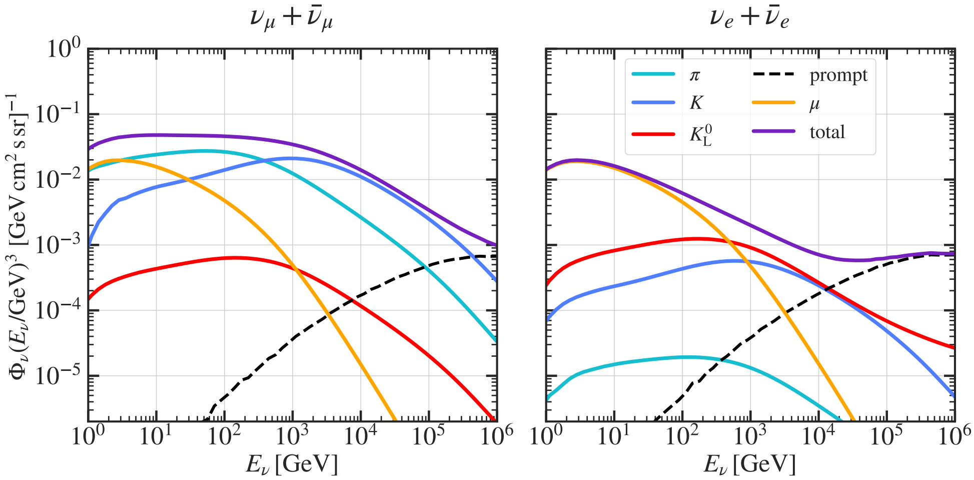

FIGURE 2.4 – Energy dependence of the $\cos\theta_{zen}$-averaged atmospheric neutrino fluxes, scaled by E_ν^3. The fluxes were computed in the same way as in Figure 2.3.

energy to be produced than the light mesons. The flux of neutrinos produced in τ and D decays is referred to as the *prompt* flux, as opposed to the *conventional* flux of neutrinos from $\pi^\pm, K^\pm$, and K^0.

- That the flux of the air shower ν_τ is extremely small at energies $\mathcal{O}(100\,\mathrm{GeV})$ implies that any ν_τ detected at these energies most likely originate from neutrino flavour oscillations (e.g. $\nu_\mu \to \nu_\tau$, as shown in Figures 2.1 and 2.2).
- In general, atmospheric neutrino fluxes are dominated by low-energy neutrinos: for example, in Figure 2.4, the ν_μ (flux $\times E_\nu^3$) curve remains approximately flat between 1 and 10^3 GeV, indicating that flux $\propto E^{-3}$, to first order. For $E_\nu < \mathcal{O}(100\,\mathrm{GeV})$, the largest contribution to the ν_e flux comes from muons, and to the ν_μ flux – from pions (with the muon contribution dominating only until $\sim 3\,\mathrm{GeV}$).
- The flux in Figure 2.3 is almost completely up-down symmetric by construction (where "up" corresponds to $\cos\theta_{zen} < 0$, and "down" – to $\cos\theta_{zen} > 0$). The reason for this is that no geomagnetic cutoff (i.e., allowing only cosmic ray primaries with a sufficient energy to come from a certain direction to a specific location on Earth) has been imposed in these calculations, which were carried out with the MCEq software [1, 2]. Another simplification of the presented calculations is the **collinear approximation** of neutrino production with respect to the cosmic ray primary axis – i.e., the simplification of the full air shower geometry (including both longitudinal and angular development) to longitudinal-only. The distinction between the two geometries is illustrated in Figure 2.5.

While valid for the > 10 GeV atmospheric neutrino flux calculations, both

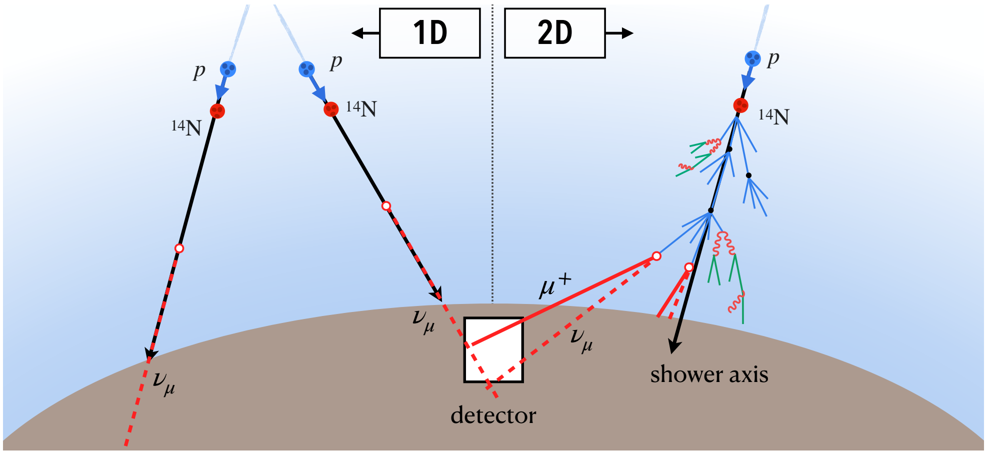

FIGURE 2.5 – Air shower development in the 1D geometry (left panel: neutrinos collinear with the primary proton axis) and the 2D geometry (right panel: neutrinos can deflect from the primary axis).

the $|\mathbf{B}| \approx 0$ and the collinearity assumptions need to be lifted for $\leq \mathcal{O}(\text{GeV})$ neutrinos. To stress the importance of the latter aspect, Table 2.2 quotes the average angles θ_ν of the neutrino deflection with respect to the primary particle axis, as obtained in [65] via a three-dimensional Monte Carlo simulation. We see that at energies above 5 GeV, the neutrino emission angle is $\lesssim 2°$, and

E_ν [GeV]	$\langle\theta_{\nu_e+\bar{\nu}_e}\rangle$ [deg]	$\langle\theta_{\nu_\mu+\bar{\nu}_\mu}\rangle$ [deg]
0–0.25	47.6	53.4
0.25–0.5	23.8	27.6
0.5–1.0	15.6	15.9
1.0–2.0	8.9	9.0
2.0–5.0	4.4	4.6
5.0–20.0	1.8	1.8
20.0–200.0	0.5	0.5

TABLE 2.2 – Average neutrino emission angle θ_ν with respect to primary particle axis as a function of neutrino energy E_ν. The values are quoted directly from [65]

the collinearity assumption can be justified. However, in the 1–2 GeV range the average emission angle is already at ∼9° and increases dramatically at lower energies. This has a large effect on the full-sky angular distributions of $\lesssim \mathcal{O}(\text{GeV})$ atmospheric neutrinos, as illustrated in Figure 2.6. In particular, we notice that the main difference between the collinear and the non-collinear treatments of neutrino production (i.e., the thin solid line and the thick solid line in Figure 2.6, respectively) is in the strong enhancement of the near-horizontal ($\cos\theta_{\text{zen}} \in [-0.3, 0.3]$) fluxes at $E_\nu \lesssim 3$ GeV. The inclusion of the geomagnetic field into the calculations, on the other hand, affects mostly the fluxes of the upgoing $\cos\theta_{\text{zen}} \lesssim -0.3$ neutrinos. To highlight the importance

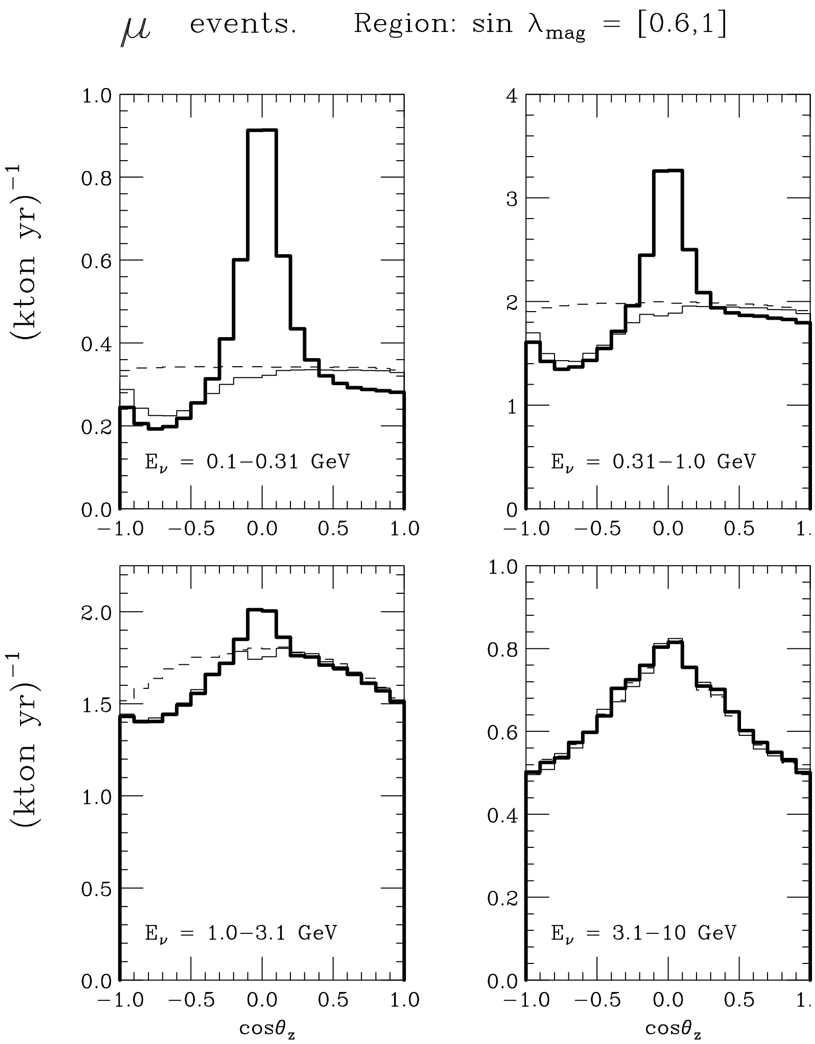

FIGURE 2.6 – $\cos\theta_{\text{zen}}$ distributions of ν_μ neutrinos, as calculated for the magnetic north polar region ($\sin\lambda_{\text{mag}} \in [0.6, 1]$, where λ_{mag} is the geomagnetic latitude). The dashed line corresponds to the calculation without the geomagnetic (**B**) field and with the collinear approximation of atmospheric neutrino production with respect to the primary particle axis. The thin solid line adds the **B**-field, and the thick solid line includes both the **B**-field and the off-axis production of neutrinos. The figure is taken from [63].

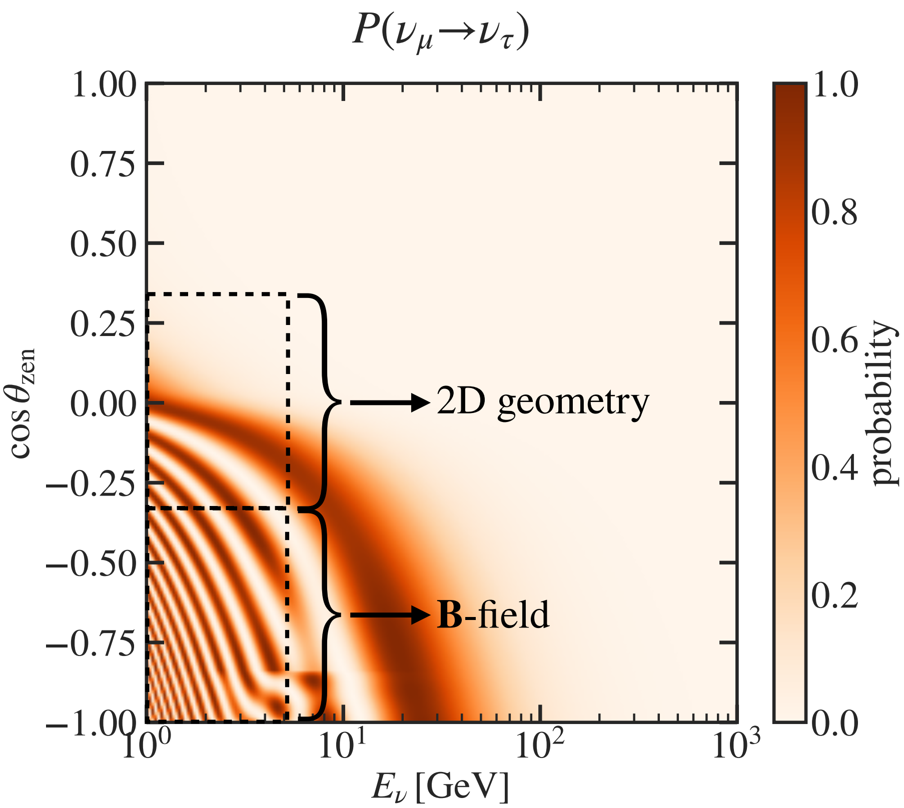

FIGURE 2.7 – The probability of $\nu_\mu \to \nu_\tau$ oscillations for atmospheric neutrinos, as computed using the NuCraft software [119] with the NuFit 5.1 (2021) oscillation parameters [113]. The PREM Earth model [120] is assumed for the computation of matter effects [121, 122]. The two highlighted regions correspond to the low-energy regime, where the $\cos\theta_{\rm zen}$ distributions of the unoscillated ν_μ neutrinos are affected by the deflection of neutrinos from the cosmic primary ray axis ("2D geometry") and the curving of the charged particle trajectories in the geomagnetic (**B**) field.

of these two aspects for neutrino oscillation measurements, we present the oscillation probability of $\nu_\mu \to \nu_\tau$ across the $(E_\nu, \cos\theta_{\rm zen})$ space in Figure 2.7. As clear from the figure, the regions of the oscillogram where the neutrino flux is affected by the off-axis neutrino production and the geomagnetic field both contain strong oscillation signatures. This means that for an accurate determination of the neutrino oscillation parameters in a real analysis, where $P_{\nu_\mu \to \nu_\tau}(E, \cos\theta_{\rm zen})$ is convolved with the unoscillated flux $\Phi_{\nu_\mu}(E, \cos\theta_{\rm zen})$, the modelling of the latter has to include both the "2D geometry" and the magnetic field effects. In this thesis, we focus on the 2D geometry implementation only, extending the MCEq software used to produce the fluxes in Figures 2.3 and 2.4 with the angular development of air showers.

II

Cascade equations

CHAPTER 3

One-dimensional cascade equations

With this chapter, we begin the detailed discussion of **cascade equations**, which are the coupled differential equations describing production, interaction, and decay of particles in the atmosphere. These equations compute the evolution of the particle flux Φ, i.e., the number of particles per unit energy, time, area, and solid angle expected to reach a certain atmospheric altitude *on average*. This is in contrast with the Monte Carlo approaches to air shower evolution, e.g. via the codes such as CORSIKA [55] or AIRES [56], where every individual particle is tracked and the expectation values of the fluxes are computed from the ensemble of simulated particles. For the purpose of atmospheric neutrino flux modelling, only the expectation values are in the end of interest, and obtaining them directly from the cascade equations, while avoiding the statistical uncertainties and high computational costs of the Monte Carlo simulations, is an appealing approach.

A natural way to introduce the cascade equations is via formulating them in one dimension first, namely in the approximation where all secondary particles in an air shower evolve collinearly with the shower-inducing primaries. We will provide an analytical formulation of such equations in Section 3.1 and show how they are formulated numerically in terms of matrices in Section 3.2. The latter form the basis of the *Matrix Cascade Equations* (MCEq) code [1, 2], and the description of the 1D MCEq framework concludes this chapter.

3.1 ANALYTICAL FORMULATION

Starting with the flux of cosmic rays incident on the top of the atmosphere, the evolution of the particle showers is typically described in terms of the **atmospheric slant depth** X. At the observation altitude h_o above surface,

$$X(h_o) = \int_0^{h_o} \mathrm{d}\ell \rho_{\mathrm{air}}(\ell), \tag{3.1}$$

where ρ_{air} is the air density and the integral is evaluated along the trajectory ℓ of the shower core. With ρ_{air} given in $\mathrm{g\,cm^{-3}}$, and ℓ by convention taken in cm, the unit of X is $\mathrm{g\,cm^{-2}}$. The coupled cascade equations [1, 2, 61] prescribe that the flux Φ_h of the particle species h with energy E (defined as in Equation (2.9)) evolves as a function of X according to

$$\frac{\mathrm{d}\Phi_h(E,X)}{\mathrm{d}X} = -\frac{\Phi_h(E,X)}{\lambda_{\mathrm{int},h}(E)} - \frac{\Phi_h(E,X)}{\lambda_{\mathrm{dec},h}(E,X)} \tag{3.2a}$$

$$- \frac{\partial}{\partial E}(\mu_E \Phi_h(E,X)) \tag{3.2b}$$

$$+ \sum_l \int_E^\infty \mathrm{d}E_l \frac{\mathrm{d}N^{\mathrm{dec}}_{l(E_l)\to h(E)}}{\mathrm{d}E} \frac{\Phi_l(E_l,X)}{\lambda_{\mathrm{int},l}(E_l)} \tag{3.2c}$$

$$+ \sum_l \int_E^\infty \mathrm{d}E_l \frac{\mathrm{d}N^{\mathrm{int}}_{l(E_l)\to h(E)}}{\mathrm{d}E} \frac{\Phi_l(E_l,X)}{\lambda_{\mathrm{dec},l}(E_l,X)}. \tag{3.2d}$$

The sink terms in Equation (3.2a) represent the loss of the particle h as the result of its interactions in the atmosphere after travelling the interaction length $\lambda_{\mathrm{int},h}$, or its decay (if applicable) after travelling the decay length $\lambda_{\mathrm{dec},h}$. Another sink term in Equation (3.2b) stands for the energy losses of the charged particles due to ionization, where $\mu_E = \langle \frac{\mathrm{d}E}{\mathrm{d}X} \rangle$ is the average energy loss per unit length. The source terms in Equation (3.2c) and Equation (3.2d) describe the production of this particle in the interactions and decays of other particle species l with energy E_l, with the respective yields of particle h reflected in the $\frac{\mathrm{d}N_{l(E_l)\to h(E)}}{\mathrm{d}E}$ factors. The energy conservation constraint is given in the integral bounds ($\int_E^\infty$) of Equations (3.2c) and (3.2d): it requires that the total energy E_l of the primary particle l must be greater than, or equal to, the total energy E of the secondary particle h.

As seen from Equation (3.2), the evolution of the particle fluxes is driven by the interplay of interactions and decays. The interaction length and the decay length are both energy-dependent, with

$$\lambda_{\mathrm{int},h} = \frac{m_{\mathrm{air}}}{\sigma^{\mathrm{inel}}_{h-\mathrm{air}}(E)} \tag{3.3}$$

and

$$\lambda_{\mathrm{dec},h}(E,X) = \frac{c\tau_h E \rho_{\mathrm{air}}(X)}{m_h}, \tag{3.4}$$

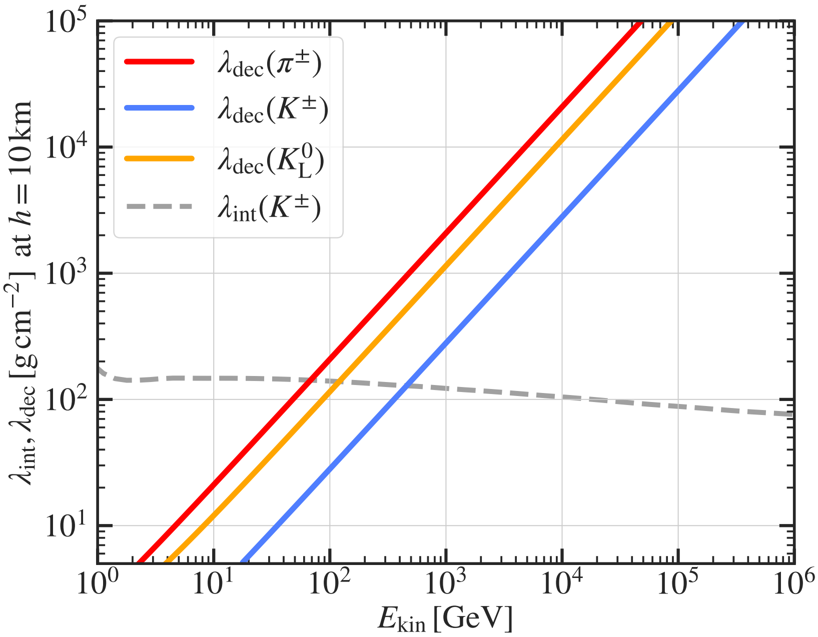

Figure 3.1 – Decay lengths $\lambda_{\rm dec}$ shown for several light mesons as a function of their kinetic energy (solid lines), where the same density profile as in fig. 2.3 is assumed. The interaction length of $K^\pm$ is shown for comparison (dashed line), where the DPMJet-III 19.1 inelastic cross sections [62, 123] were used for Equation (3.3).

where $m_{\rm air}\,[\rm g]$ is the mean mass of the atomic nuclei in the atmosphere (weighted by the respective mass fractions); $\sigma^{\rm inel}_{h-{\rm air}}\,[\rm cm^2]$ is the inelastic scattering cross section; $\tau_h\,[\rm s]$ and $m_h\,[\rm GeV]$ are the mean lifetime and the mass of the particle h at rest, respectively; E is the total energy of h in the lab frame; and $\rho_{\rm air}(X)\,[\rm g\,cm^{-3}]$ is the slant depth-dependent atmospheric density. That the factor of E/m_h (i.e., the Lorentz boost γ) enters Equation (3.4) is a reflection of the relativistic time dilation effect.

In Figure 3.1, we show the energy dependence of the decay lengths for the $\pi^\pm$, $K^\pm$, and $K^0_{\rm L}$ mesons, as compared to the interaction length for $K^\pm$[1]. Whenever $\lambda_{\rm dec} < \lambda_{\rm int}$, the decay processes dominate, and vice versa; for example, at the plotted altitude of $h = 10\,\rm km$, interactions dominate over decays for $\pi^\pm$ with energies $> 70\,\rm GeV$.

3.2 Numerical formulation and the MCEq code

For a shower particle h which can interact with the nuclei in the atmosphere (e.g. ^{14}N or ^{16}O), the interaction cross section $\sigma_{h-{\rm air}}$ is energy-dependent, as is the yield of the interaction products in an inelastic collision. Similarly, if the particle is unstable, the energy spectra of its decay products depend

[1] The interaction lengths of other mesons are within 20–40 % of $\lambda_{\rm int}(K^\pm)$.

on the boost of the parent particle. It is therefore natural to discretize the transport equation (3.2) in energy, i.e. to distribute the particle fluxes between the discrete energy bins E_i, $i \in [1, N_E]$. To simplify the notation in this and subsequent chapters, we will define the "1D" flux of the particle h at the energy E_i as

$$\Phi^h_{E_i} = \frac{\mathrm{d}N_h}{\mathrm{d}E}\bigg|_{E=E_i}, \tag{3.5}$$

i.e., the differential of the particle number N_h with respect to energy, where the integration over a unit of area, time, and solid angle will be implied. The discrete cascade equation then reads:

$$\begin{aligned}
\frac{\mathrm{d}\Phi^h_{E_i}(X)}{\mathrm{d}X} = &-\frac{\Phi^h_{E_i}(X)}{\lambda^h_{\mathrm{int},E_i}} - \frac{\Phi^h_{E_i}(X)}{\lambda^h_{\mathrm{dec},E_i}(X)} && \text{(3.6a)}\\
&-\nabla_i[\mu^h_{E_i}\Phi^h_{E_i}(X)] && \text{(3.6b)}\\
&+\sum_l \sum_{E^*_k \geq E^*_i} \frac{c_{l(E_k)\to h(E_i)}}{\lambda^l_{\mathrm{int},E_k}}\Phi^l_{E_k}(X) && \text{(3.6c)}\\
&+\sum_l \sum_{E^*_k \geq E^*_i} \frac{d_{l(E_k)\to h(E_i)}}{\lambda^l_{\mathrm{dec},E_k}(X)}\Phi^l_{E_k}(X), && \text{(3.6d)}
\end{aligned}$$

where we arranged the terms in the same order as in Equation (3.2) to clarify the correspondences between the continuous and the discrete equation versions. In Equation (3.6c), we defined the coefficient c for the yield of particle h in interactions as

$$c_{l(E_k)\to h(E_i)} = \frac{\mathrm{d}N_{l(E_k)\to h(E_i)}}{\mathrm{d}E}\bigg|_{E=E_i}\Delta E_k, \tag{3.7}$$

which translates as the flux of particles h with energy E_i generated per primary l within the energy bin E_k. An analogous definition holds for the decay coefficient d in Equation (3.6d). These definitions let us replace the integral $\int_E^\infty$ by the sum $\sum_{E^*_k \geq E^*_i}$, which once again reflects the energy conservation constraint. Here we explicitly clarify that the energy conservation must be reflected by the total particle energies E^*_k and E^*_i, as opposed to the kinetic energies E_k and E_i[2] which form the grid of Equation (3.6) in 1D MCEq [1, 2].

If H species participate in the coupled transport, the all-species particle flux vector $\mathbf{\Phi}$ has the dimension $N_E \cdot H$:

$$\mathbf{\Phi} = (\Phi^p_{E_0}\Phi^p_{E_1}\ldots\Phi^p_{E_{N_E-1}}\ \ldots\ \Phi^{\pi^+}_{E_0}\Phi^{\pi^+}_{E_1}\ldots\Phi^{\pi^+}_{E_{N_E-1}}\ldots)^\top \tag{3.8}$$

[2] This distinction is important as the energy conservation constraint does not necessarily have to hold for kinetic energies, especially in the case of low-energy primaries and low-mass secondaries.

The particle yield coefficients $c_{l \to h}$ and $d_{l \to h}$ associated with the production of h by different primaries l can then be put in a matrix form, where the dimension of such matrices is $(N_E \cdot H) \times (N_E \cdot H)$. For example, the all-species matrix of interaction coefficients is constructed as

$$\mathbf{C} = \begin{pmatrix} \mathbf{C}_{p\to p} & \mathbf{C}_{n\to p} & \mathbf{C}_{\pi^+\to p} & \dots \\ \mathbf{C}_{p\to n} & \mathbf{C}_{n\to n} & \mathbf{C}_{\pi^+\to n} & \dots \\ \mathbf{C}_{p\to \pi^+} & \mathbf{C}_{n\to \pi^+} & \mathbf{C}_{\pi^+\to \pi^+} & \dots \\ \dots & \dots & \dots & \ddots \end{pmatrix}, \tag{3.9}$$

where each individual sub-block is

$$\mathbf{C}_{l\to h} = \begin{pmatrix} c_{l(E_0)\to h(E_0)} & \cdots & c_{l(E_{N_E-1})\to h(E_0)} \\ & & c_{l(E_{N_E-1})\to h(E_1)} \\ & \ddots & \dots \\ \mathbf{0} & & c_{l(E_{N_E-1})\to h(E_{N_E-1})} \end{pmatrix}. \tag{3.10}$$

An analogous definition holds for the all-species decay coefficient matrix $\mathbf{D}$. In this way, the matrices $\mathbf{C}$ and $\mathbf{D}$ filled with $c_{l\to h}$ and $d_{l\to h}$ across the entire energy grid couple the cascade equations for the different particle species. The interaction and decay lengths can also be put in a matrix form, with

$$\begin{aligned} \mathbf{\Lambda}_{\text{int}} = \text{diag}\Bigg\{ & \frac{1}{\lambda^{p}_{\text{int},E_0}}, \frac{1}{\lambda^{p}_{\text{int},E_1}}, \dots \frac{1}{\lambda^{p}_{\text{int},E_{N_E-1}}}, \dots \\ & \frac{1}{\lambda^{\pi^+}_{\text{int},E_0}}, \frac{1}{\lambda^{\pi^+}_{\text{int},E_1}}, \dots \frac{1}{\lambda^{\pi^+}_{\text{int},E_{N_E-1}}}, \dots \Bigg\}, \end{aligned} \tag{3.11}$$

and $\mathbf{\Lambda}_{\text{dec}}$ constructed analogously from the reduced decay lengths $\lambda^{h,*}_{\text{dec},E_i} \equiv \lambda^{h}_{\text{dec},E_i}\,\rho^{-1}_{\text{air}}(X)$. With these definitions, the matrix form of the coupled system of equations (3.6) can finally be written as [1, 2]:

$$\frac{\mathrm{d}\mathbf{\Phi}}{\mathrm{d}X} = -\mathbf{\nabla}_E[\text{diag}(\boldsymbol{\mu})\cdot\mathbf{\Phi}] + \left[(-\mathbb{I}+\mathbf{C})\mathbf{\Lambda}_{\text{int}} + \frac{1}{\rho_{\text{air}}(X)}(-\mathbb{I}+\mathbf{D})\mathbf{\Lambda}_{\text{dec}}\right]\mathbf{\Phi}, \tag{3.12}$$

where the $-\mathbb{I}$ matrices absorbed the sink terms from Equation (3.6a), and $\mathbf{\nabla}_E$ is the finite difference operator for the first-order energy derivative. Equation (3.12) is solved by the forward integration in X, which forms the basis of the longitudinal air shower development in the 1D MCEq software [1, 2].

In MCEq, the yield coefficients are derived from event generators (e.g. UrQMD [124], DPMJet [62, 123], Sibyll [2, 125], or EPOS-LHC [126] for hadron-nucleus collisions, and Pythia [127] for decays) by histogramming the secondary particle yields as a function of the secondary and the primary kinetic energies (E_i and E_k). The kinetic energy grid in MCEq is logarithmically

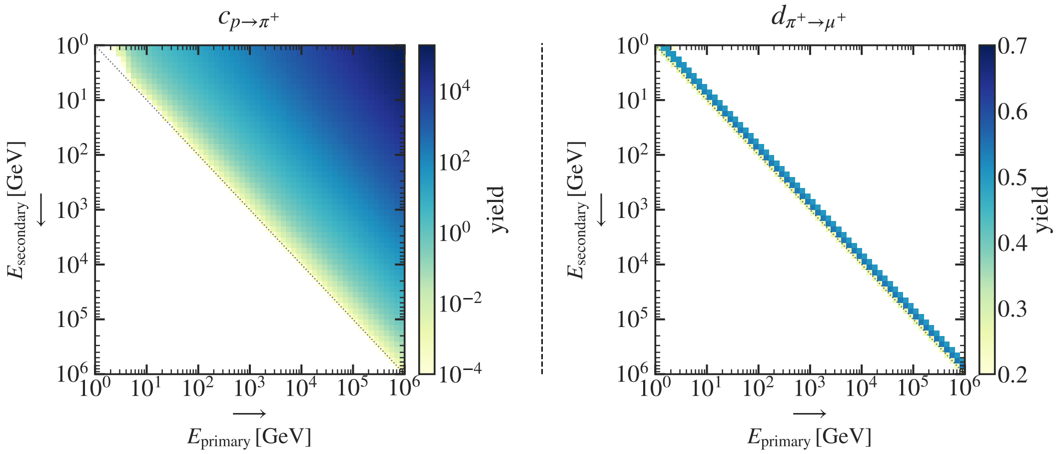

Figure 3.2 – *Left:* interaction yield coefficient $c_{p\to\pi^+}$ for production of π^+ in the proton-air collisions. *Right:* decay yield coefficient $d_{\pi^+\to\mu^+}$ for production of μ^+ in the π^+ decays. The c and d coefficients are computed according to Equation (3.7) after histogramming the secondary particle yields from the DPMJet-III 19.1 [62, 123] and Pythia [127] event generators, respectively.

spaced between 10^{-2} and 10^{11} GeV, with $\Delta \log_{10} E = 0.1$ (thus giving 10 bins per decade of energy). In the 1D approximation, all secondary particle angles with respect to the primary particle direction of motion are contributing to the yield coefficients, thereby resulting in the angle-integrated interaction/decay yields inside each energy bin. Example 1D MCEq matrices for the pion yields in the proton-air interactions and the μ^+ yields in the π^+ decay are shown in Figure 3.2.

In Section 2.2, we have already provided the example 1D MCEq solutions for the ν_μ and ν_e fluxes at the Earth's surface. As we have now revealed that they originate as solutions to Equation (3.12), it is also instructive to present these solutions "in the making," i.e., following the evolution of fluxes with the slant depth. Figure 3.3 shows the combined $\mu^- + \mu^+$, $\nu_\mu + \bar{\nu}_\mu$, and $\nu_e + \bar{\nu}_e$ fluxes integrated over the kinetic energies $E < 10\,\text{GeV}$. As expected, the $\mu^- + \mu^+$ fluxes have a maximum (at about $h \simeq 12\,\text{km}$), which reflects the interplay between the production of muons and their decay. Since neutrinos are stable and effectively non-interacting in the atmosphere due to its low density, their fluxes increase monotonically as a function of X. The neutrino production rate, however, decreases with increasing slant depth; this is due to the fact that muons, pions, and kaons eventually decay and have no "replenishment" from the shower when the primary protons lose energy. In the next chapter, we will show how to add an "orthogonal" dimension to Figure 3.3, i.e., to extend the MCEq framework in such a way that the flux evolution is computed as a function of both X and the angle θ with the respect to the primary axis.

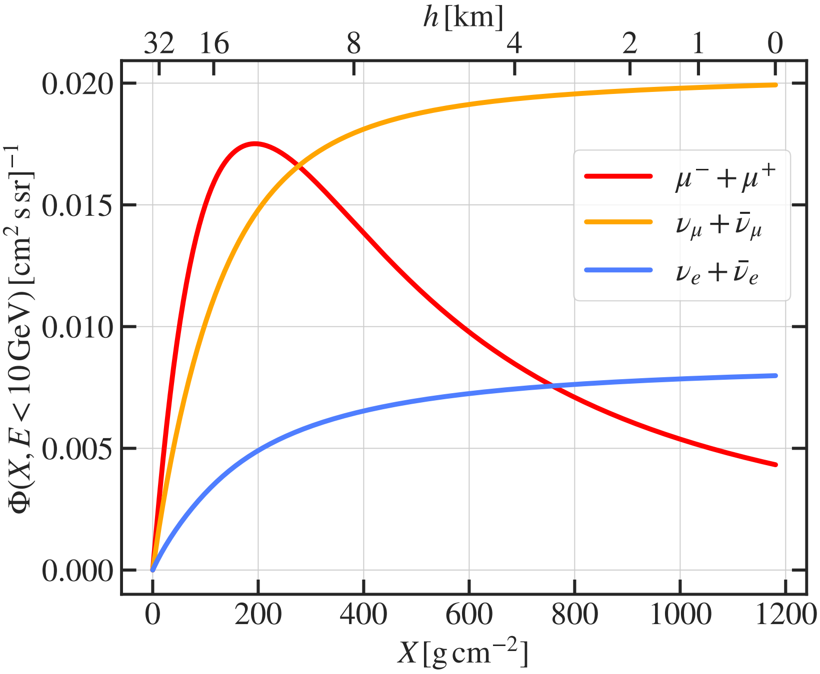

FIGURE 3.3 – Longitudinal evolution of the lepton fluxes integrated over kinetic energies $0 \leq E \leq 10\,\mathrm{GeV}$. The shower inclination in this case is 30°, and the rest of the setup follows that of Figure 2.3. The top axis shows the slant depth X converted to the height h above the Earth's surface, according to the density profile $\rho_{\mathrm{air}}(X)$.

CHAPTER 4

Two-dimensional cascade equations

As a rule of thumb, the angular deflection of the secondary (daughter) particles in inelastic collisions or decays of high-energy projectiles is small, meaning that the secondary particles will mostly follow the primary particle trajectories. This justifies the use of the 1D approximation in the evolution of high-energy hadronic cascades, which leads to the 1D cascade equation discussed in Chapter 3. However, this approximation becomes increasingly less valid with decreasing energy, which we already saw in Table 2.2 by examining the mean deflection angles of $\mathcal{O}$(GeV) neutrinos. The accuracy of the one-dimensional cascade equation solutions is therefore limited when it comes to angular distributions of low-energy secondaries. In this chapter, we develop an approach to add a second (angular) dimension to the cascade equation, which is described in Section 4.1. Further, in Section 4.2, we show how to simplify these equations and gain significant speedup by reformulating them in the frequency domain via the Hankel transform.

4.1 Numerical formulation in the angular space

To smoothly transition to the 2D cascade equations, let us imagine a simple scenario with a primary particle l travelling along the z-axis and producing a particle h as the result of interaction or decay. In the 1D approximation, the velocity unit vector $\hat{\mathbf{u}}^{l\to h}$ of the secondary particle relative to the direction of l can be written as $\langle 0, 0, 1\rangle$. This is the idealistic case of perfect collinearity, where the polar angle $\theta_{l\to h}$ between h and l is negligibly small. At low energies, where the 1D approximation breaks down, one has to take into account the x and y components of the velocity unit vector to accurately compute the angular distribution of the secondary particles. Writing out $\hat{\mathbf{u}}^{l\to h} = \langle \sin\theta_{l\to h}\cos\varphi_{l\to h}, \sin\theta_{l\to h}\sin\varphi_{l\to h}, \cos\theta_{l\to h}\rangle$, we no longer assume that $\sin\theta_{l\to h}$ is negligible and that $\cos\theta_{l\to h}$ is infinitely close to 1. However, for a single interaction/decay, we can still rely on the smallness of the polar angle to write $\sin\theta_{l\to h} \simeq \theta_{l\to h}$, as well as invoke azimuthal symmetry (i.e. invariance *wrt.* $\varphi^{l\to h}$). Then, to second order in θ,

$$\hat{\mathbf{u}}^{l\to h} = \langle \theta_{l\to h}\cos\varphi_{l\to h}, \theta_{l\to h}\sin\varphi_{l\to h}, 1 - \frac{(\theta_{l\to h})^2}{2}\rangle \tag{4.1}$$

Similarly, the initial particle l can be assigned a unit velocity vector $\hat{\mathbf{u}}^l = \langle \theta_l\cos\varphi_l, \theta_l\sin\varphi_l, 1 - \frac{(\theta_l)^2}{2}\rangle$ (albeit in our example $\theta_l = 0$). In a Monte Carlo simulation, where the interactions or decays would be treated on an event-by-event basis, the two full velocity vectors (i.e., $\hat{\mathbf{u}}^l$ and $\hat{\mathbf{u}}^{l\to h}$ scaled by the respective magnitudes) could be simply added together to find the absolute direction $\hat{\mathbf{u}}^h$ of the secondary particle h in the lab frame. However, for inclusive flux calculations in a numerical code like MCEq, one has to remember that both the lab frame angle θ_l of the primary particle and the relative scattering/decay angle $\theta_{l\to h}$ have a certain *probability density*. For example, the total flux $\Phi^l_{E_k}$ of the primary l with energy E_k can have an angular probability density $\phi^l_{E_k}(\theta_l)$ such that

$$\Phi^l_{E_k} = \int_0^{\theta_{\max}} \phi^l_{E_k}(\theta_l)\theta_l \mathrm{d}\theta_l. \tag{4.2}$$

Comparing to Equation (3.5), we find:

$$\phi^l_{E_k}(\theta_l) = \frac{1}{\theta_l}\frac{\mathrm{d}^2 N_l(\theta_l)}{\mathrm{d}\theta_l \mathrm{d}E}\bigg|_{E=E_k}. \tag{4.3}$$

Throughout this thesis, we will assume $\theta_{\max} = \pi/2$, i.e. consider only forward-going particles. In general, the distribution of θ_l is either defined by the user as the initial condition (e.g. a delta function denoting the direction of a single cosmic ray primary) or is an input to the differential equation integrator from the previous propagation step. In that sense, the probability density of θ_l is dynamic, i.e. evolving with the slant depth X. On the other hand, the distribution of $\theta_{l\to h}$ is defined by the allowed phase space in a given interaction or decay process (following the prescription of a given event generator) and constitutes a static **diffusion kernel**. With these two ingredients at hand, the angular distribution of the particle h in the $\mathcal{XY}$ plane can be obtained as the 2D convolution of the angular distribution of particle l with the diffusion kernel $l \to h$, which we will denote as $\varsigma_{l\to h}$ for interactions and $\delta_{l\to h}$ for decays. We schematically show the 2D convolution principle in

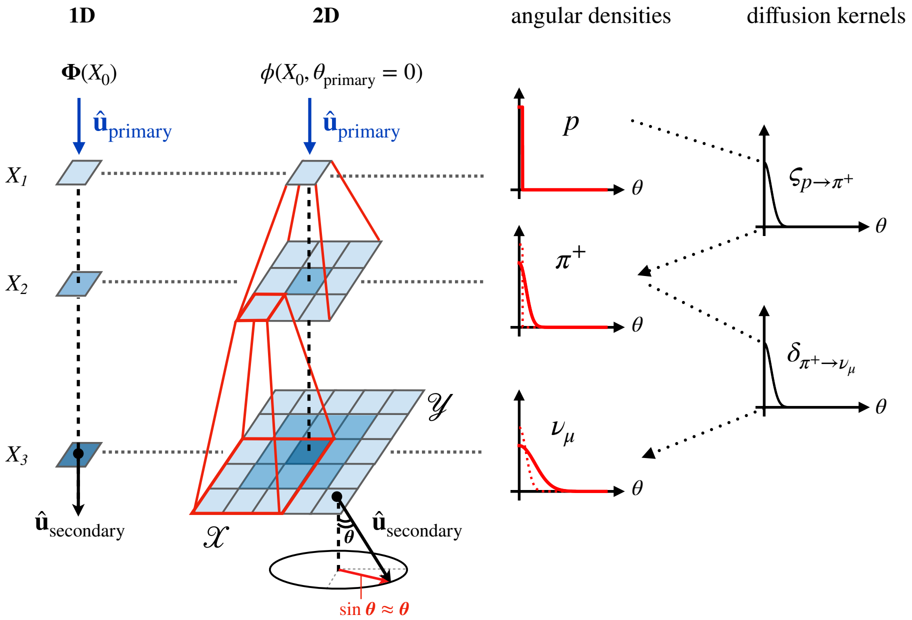

Figure 4.1 – Schematic development of a hadronic cascade ($p \to \pi^+ \to \nu_\mu$) in the 1D (longitudinal-only) and the 2D (longitudinal + angular) geometries. The longitudinal propagation is discretized into four steps along the slant depth X. At each step in X, we draw the angular distribution of the primaries from the previous step as the dotted line, and the current angular distribution of the specified particle as the solid line. The distributions of secondaries get wider further down the chain due to the convolution with the diffusion kernels $\varsigma_{p\to\pi^+}$ and $\delta_{\pi^+\to\nu_\mu}$ (see text for details).

Figure 4.1. In this toy setup, a beam of protons with the total flux $\mathbf{\Phi}$ enters the atmosphere at the slant depth X_0, making an angle $\theta_{\text{primary}} = 0$ with the z-axis (pointing down). The direction of the proton beam is represented by the unit vector $\hat{\mathbf{u}}_{\text{primary}}$. After propagating longitudinally to the next slant depth step X_1, the proton interacts with atmospheric nuclei and produces pions (π^+) at X_2. Between X_2 and X_3, some of the pions decay, leading to the flux of muon neutrinos at X_3. In the 1D geometry, the velocity unit vector $\hat{\mathbf{u}}_{\text{secondary}}$ of ν_μ is aligned with $\hat{\mathbf{u}}_{\text{primary}}$, while in the 2D geometry, this does not hold beyond X_0. As the proton interacts with the atmospheric nuclei, the secondary products of the interaction (including the π^+) gain transverse momentum, and their angular distribution widens. This is represented by the convolution with the diffusion kernel of the interaction, $\varsigma_{p\to\pi^+}$. As the pion decays, the muon neutrinos get an even wider angular distribution due to the convolution of the pion angular density with the decay kernel $\delta_{\pi^+\to\nu_\mu}$.

Mathematically, the production of the particle h with energy E_i by the primary l with energy E_k leads to the following change in the angular probability density of h:

$$\frac{\mathrm{d}^+}{\mathrm{d}X}\phi^h_{E_i}(X,\theta_h) = \frac{1}{\lambda^l_{\mathrm{int},E_k}}\int_0^{\pi/2} \varsigma_{l(E_k,\theta_l)\to h(E_i,\theta_h)}\phi^l_{E_k}(X,\theta_l)\theta_l\,\mathrm{d}\theta_l + \frac{1}{\lambda^l_{\mathrm{dec},E_k}}\int_0^{\pi/2} \delta_{l(E_k,\theta_l)\to h(E_i,\theta_h)}\phi^l_{E_k}(X,\theta_l)\theta_l\,\mathrm{d}\theta_l, \tag{4.4}$$

where we used $(\mathrm{d}^+/\mathrm{d}X)$ as a shorthand for the source term of the X-derivative of $\phi^h_{E_i}$. The appearance of the θ_l factor in the integrals of Equation (4.4) is an important feature of the 2D convolution in the $\mathcal{XY}$ plane, where θ_l and $\theta_{l\to h}$ are interpreted as the radii of the $\hat{\mathbf{u}}^l$ and $\hat{\mathbf{u}}^{l\to h}$ velocity vectors projected onto $\mathcal{XY}$. As the two functions being convolved are azimuthally symmetric, we have absorbed the integration over the azimuthal variable φ into $\varsigma_{l\to h}$ and $\delta_{l\to h}$, following the formalism of [128]. The integrals of these diffusion kernels over the polar scattering angle are equivalent to the total yield coefficients $c_{l(E_k)\to h(E_i)}$ and $d_{l(E_k)\to h(E_i)}$ from Equation (3.6). In particular, for interaction coefficients we postulate

$$c_{l(E_k)\to h(E_i)} = \int_0^{\pi/2} \varsigma_{l(E_k,\theta_l)\to h(E_i,\theta_h)}\theta_{l\to h}\mathrm{d}\theta_{l\to h} = \int_0^{\pi/2} \varsigma_{l(E_k,0)\to h(E_i,\theta)}\theta\mathrm{d}\theta, \tag{4.5}$$

where the change of variables is possible thanks to the translational equivariance of the diffusion kernel. The normalization of the decay coefficients is fully analogous to that in Equation (4.5), swapping $c \leftrightarrow d$ and $\varsigma \leftrightarrow \delta$. Finally, we note that the sink terms in Equation (3.6a) and Equation (3.6b) do not change the angular distribution of the primaries and simply contribute to the change in the overall normalization. Combining this observation with Equation (4.4), we can write down the 2D version of Equation (3.6) as follows:

$$\begin{aligned}\frac{\mathrm{d}\phi^h_{E_i}(X,\theta)}{\mathrm{d}X} &= -\frac{\phi^h_{E_i}(X,\theta)}{\lambda^h_{\mathrm{int},E_i}} - \frac{\phi^h_{E_i}(X,\theta)}{\lambda^h_{\mathrm{dec},E_i}(X)} - \nabla_i[\mu^h_{E_i}\phi^h_{E_i}(X,\theta)] \\ &+ \sum_l \sum_{E_k^*\geq E_i^*}\int_0^{\pi/2}\frac{\varsigma_{l(E_k,\theta_l)\to h(E_i,\theta)}}{\lambda^l_{\mathrm{int},E_k}}\phi^l_{E_k}(X,\theta_l)\theta_l\mathrm{d}\theta_l \\ &+ \sum_l \sum_{E_k^*\geq E_i^*}\int_0^{\pi/2}\frac{\delta_{l(E_k,\theta_l)\to h(E_i,\theta)}}{\lambda^l_{\mathrm{dec},E_k}(X)}\phi^l_{E_k}(X,\theta_l)\theta_l\mathrm{d}\theta_l,\end{aligned} \tag{4.6}$$

where we have now dropped the h index in θ_h to simplify the notation. Importantly, this equation gives the evolution of the angular and energy density of all particle species as a function of the slant depth X in the atmosphere. The longitudinal development of the secondary particle cascades is computed, as before, through the forward difference integration of Equation (4.6). The new component in Equation (4.6) compared to Equation (3.6) is the angular development of the secondaries, which is taken care of via the 2D convolutions of the angular densities of the primaries with the interaction/decay diffusion kernels.

4.2 NUMERICAL FORMULATION IN THE FREQUENCY SPACE

Depending on the energy scales of hadronic interactions and unstable particle decays in the atmosphere, the widths of the angular distributions of the secondary particles can vary by orders of magnitude. The low-energy secondaries normally have a large spread about the primary particle axis, whereas the high-energy ones do not deflect from the primary axis significantly. Furthermore, the evolution of hadronic cascades over sizeable slant depths can have a visible impact on the angular distributions of the secondaries even if the angular deflection in a single interaction/decay is small. As the result, Equation (4.6) demands a "universal" θ grid which could accommodate both large and small angular deflections. Making such a grid linear would imply an extremely fine discretization, and the numerical evaluation of the 2D convolution integrals would become prohibitively expensive. On the other hand, if the θ grid were made logarithmic, the product of convolution would not exist on the same grid as the diffusion kernel and the primary particle angular density, even if the grids of the latter were aligned. While the techniques for convolving functions defined on logarithmic grids exist, they often come with hyperparameters to be tuned by the user in order to keep the numerical errors to the minimum [129–131]. This extra freedom in the choice of hyperparameters could lead to an unpredictable numerical behaviour in the integration of Equation (4.6) over thousands of steps in X.

To avoid the complications of the 2D convolutions in the θ space (which we will also refer to as the "real" space), we choose to operate in the spectral ("frequency") domain instead. For the 2D convolutions of Equation (4.6), the correct kind of transform between the two domains is the Hankel transform, which we define and justify in Section 4.2.1. The derivations in Section 4.2.1 are modified and expanded from [128].

4.2.1 *Hankel transform and the 2D convolution theorem*

The two-dimensional convolution of two functions $f(\mathbf{r}) = f(r,\varphi)$ and $g(\mathbf{r}) = g(r,\varphi)$ in polar coordinates (r,φ) is defined as

$$h(\mathbf{r}) = f(\mathbf{r}) ** g(\mathbf{r}) = \int_{-\infty}^{\infty} g(\mathbf{r}_0) f(\mathbf{r} - \mathbf{r}_0) \mathrm{d}\mathbf{r}_0, \tag{4.7}$$

where $\mathrm{d}\mathbf{r}_0 = r_0 \mathrm{d}r_0 \mathrm{d}\varphi_0$. The functions $g(\mathbf{r}_0)$ and $f(\mathbf{r}-\mathbf{r}_0)$ can be expanded in terms of the Fourier series; the expansion of $g(\mathbf{r}_0)$ is trivial:

$$g(\mathbf{r}_0) = g(r_0, \varphi_0) = \sum_{m=-\infty}^{\infty} g_m(r_0) e^{im\varphi_0}, \tag{4.8}$$

where

$$g_m(r_0) = \frac{1}{\sqrt{2\pi}} \int_0^{2\pi} g(r_0, \varphi) e^{-jm\varphi} \mathrm{d}\varphi \tag{4.9}$$

is the standard Fourier coefficient[1]. The expansion of $f(\mathbf{r}-\mathbf{r}_0)$, as a function which is spatially shifted from $\mathbf{r}_0$ to $\mathbf{r}$, is more complex:

$$\begin{aligned} f(\mathbf{r}-\mathbf{r}_0) &= \sum_{k=-\infty}^{\infty} [f(\mathbf{r}-\mathbf{r}_0)]_k \, e^{ik\varphi} \\ &= \sum_{k=-\infty}^{\infty} e^{ik\varphi} \sum_{n=-\infty}^{\infty} e^{-i(k-n)\varphi_0} \int_0^{\infty} f_n(u) S_n^k(u, r, r_0) u \mathrm{d}u, \end{aligned} \tag{4.10}$$

where $f_n(u)$ is the familiar Fourier coefficient (defined analogously to Equation (4.9)) and S_n^k is the shift operator:

$$S_n^k(u, r, r_0) = \int_0^{\infty} J_n(\rho u) J_{k-n}(\rho r_0) J_k(\rho r) \kappa \mathrm{d}\rho. \tag{4.11}$$

In Equation (4.11), $J_n(x)$ is the n^{th} order Bessel function of the first kind. With these definitions, the 2D convolution reads

$$\begin{aligned} h(\mathbf{r}) = &\int_0^{\infty} \int_0^{2\pi} \sum_{m=-\infty}^{\infty} g_m(r_0) e^{im\varphi_0} \sum_{k=-\infty}^{\infty} e^{ik\varphi} \sum_{n=-\infty}^{\infty} e^{-i(k-n)\varphi_0} \\ &\times \int_0^{\infty} f_n(u) S_n^k(u, r, r_0) u \mathrm{d}u \, r_0 \mathrm{d}r_0 \mathrm{d}\varphi_0. \end{aligned} \tag{4.12}$$

The inner integral over φ_0, $\int_0^{2\pi} e^{im\varphi_0} e^{-i(k-n)\varphi_0} \mathrm{d}\varphi_0$, is only non-zero if $m = k-n$, in which case it reduces to 2π. This also means that $g_m \leftrightarrow g_{k-n}$. Then, using the definition of S_n^k and re-grouping the Bessel function terms, we find

$$\begin{aligned} h(\mathbf{r}) = \sum_{k=-\infty}^{\infty} 2\pi e^{ik\varphi} \int_0^{\infty} \Bigg[\sum_{n=-\infty}^{\infty} &\int_0^{\infty} g_{k-n}(r_0) J_{k-n}(\rho r_0) r_0 \mathrm{d}r_0 \\ &\times \int_0^{\infty} f_n(u) J_n(\rho u) u \mathrm{d}u \Bigg] J_k(\rho r) \rho \mathrm{d}\rho. \end{aligned} \tag{4.13}$$

[1] Note that [128] have a normalization factor $\frac{1}{2\pi}$ instead, which does not preserve the equivalence between the forward and the inverse transforms.

A cumbersome expression at first, Equation (4.13) is significantly simplified if we define the **n$^{\text{th}}$-order Hankel transform** $\mathcal{H}_n$:

$$\mathcal{H}_n[f(r)](\kappa) = \int_0^\infty f(r) J_n(\kappa r)\, r\, \mathrm{d}r \tag{4.14}$$

As we shall see further, an important property of this transform is that it is functionally equivalent to its inverse, i.e.,

$$f(r) = \int_0^\infty \Big\{ \mathcal{H}_n[f(r)](\kappa) \Big\} J_n(\kappa r) \mathrm{d}r = \mathcal{H}_n^{-1} \mathcal{H}_n[f(r)] \tag{4.15}$$

Under these definitions, Equation (4.13) becomes:

$$h(\mathbf{r}) = \sum_{k=-\infty}^{\infty} 2\pi e^{ik\varphi} \int_0^\infty \Bigg[\sum_{n=-\infty}^{\infty} \mathcal{H}_{k-n}[g_{k-n}](\rho) \cdot \mathcal{H}_n[f_n](\rho) \Bigg] J_k(\rho r) \rho \mathrm{d}\rho \tag{4.16}$$

Further simplification is achieved for the special case of *radially symmetric* functions g and f, i.e., the functions which are invariant with respect to rotation by an arbitrary angle φ in polar coordinates. For such functions, only the $m = 0$ term has a nonzero coefficient g_m in the Fourier expansion in Equation (4.8); similarly, only the $k = n = 0$ term in Equation (4.10) is non-zero (otherwise there would be a dependence on φ remaining). This means that we can rewrite Equation (4.16) as

$$h(\mathbf{r}) = 2\pi \int_0^\infty \Big[\mathcal{H}_0[g_0](\rho) \cdot \mathcal{H}_0[f_0](\rho) \Big] J_0(\rho r) \rho \mathrm{d}\rho, \tag{4.17}$$

where g_0 and f_0 are equivalent to simply $\frac{g(r)}{\sqrt{2\pi}}$ and $\frac{f(r)}{\sqrt{2\pi}}$, as follows directly from Equation (4.9). We also note that since there is no more φ dependence left in Equation (4.17), $h(\mathbf{r}) = h(r)$. Finally, we identify the integral in Equation (4.17) as the inverse Hankel transform, $\mathcal{H}^{-1}$, from Equation (4.15):

$$h(r) = \mathcal{H}_0^{-1} \Big[\mathcal{H}_0[g(r)](\rho) \cdot \mathcal{H}_0[f(r)](\rho) \Big] \tag{4.18}$$

Applying the forward transform to both sides of Equation (4.18), we arrive at the **convolution theorem** for two-dimensional radially symmetric functions:

$$\mathcal{H}[h(r)] = \mathcal{H}[f(r) * * g(r)] = \mathcal{H}[f(r)](\kappa) \cdot \mathcal{H}[g(r)](\kappa), \tag{4.19}$$

where we replaced ρ with κ and dropped the "0" in $\mathcal{H}_0$ for cleaner notation. As we will see in Section 4.2.2, it is this theorem that will help us transform the angular space cascade equations (4.6) to the **Hankel frequency space** κ.

4.2.2 2D cascade equations with discrete Hankel modes

The diffusion kernels $\varsigma_{l\to h}$ and $\delta_{l\to h}$, which represent the probability densities of the secondary particle deflections relative to their primaries in the two dimensional cascade equations (4.1), are azimuthally symmetric. This is equivalent to the "radially symmetric functions" we introduced in Section 4.2.1 when talking about the convolutions on a 2D plane; both of these terms imply invariance with respect to the angle φ in e.g. Equation (4.1) and Equation (4.12). When the geomagnetic field is not taken into account in the air shower evolution, the angular densities $\phi(X,\theta)$ of all particle species are also azimuthally/radially symmetric. Further, in Section 4.1, we made an important observation that the three-dimensional polar angle θ is to be interpreted as the *radial* variable in the $\mathcal{XY}$ plane. This means that θ is equivalent to r in Section 4.2.1. Putting these arguments together, we see that the convolution theorem in Equation (4.19) is fully applicable to our two-dimensional cascade equations. With that in mind, we bring the diffusion kernels and the angular densities of the cascade particles to the Hankel frequency space by defining their 0^{th}-order Hankel transforms as follows:

$$\tilde{\phi}^h_{E_i}(X,\kappa) \equiv \mathcal{H}[\phi^h_{E_i}(X,\theta)](\kappa) \tag{4.20a}$$

$$\tilde{\varsigma}_{l(E_k)\to h(E_i)}(\kappa) \equiv \mathcal{H}[\varsigma_{l(E_k)\to h(E_i)}(\theta)](\kappa) \tag{4.20b}$$

$$\tilde{\delta}_{l(E_k)\to h(E_i)}(\kappa) \equiv \mathcal{H}[\delta_{l(E_k)\to h(E_i)}(\theta)](\kappa) \tag{4.20c}$$

In the formal definition of $\mathcal{H}$ (see Equation (4.14)), the upper limit of the θ integral is ∞, however we only consider the forward-going particles in practice and therefore restrict our attention to $\theta \leq \pi/2$ when evaluating the forward transforms in Equation (4.20). Then, using the convolution theorem, we reformulate Equation (4.6) as

$$\begin{aligned}
\frac{\mathrm{d}\tilde{\phi}^h_{E_i}(X,\kappa)}{\mathrm{d}X} = &-\frac{\tilde{\phi}^h_{E_i}(X,\kappa)}{\lambda^h_{\text{int},E_i}} - \frac{\tilde{\phi}^h_{E_i}(X,\kappa)}{\lambda^h_{\text{dec},E_i}(X)} \\
&- \nabla_i[\mu^h_{E_i}\tilde{\phi}^h_{E_i}(X,\kappa)] \\
&+ \sum_l \sum_{E^*_k \geq E^*_i} \frac{[\tilde{\varsigma}_{l(E_k)\to h(E_i)} \cdot \tilde{\phi}^l_{E_k}](\kappa)}{\lambda^l_{\text{int},E_k}} \\
&+ \sum_l \sum_{E^*_k \geq E^*_i} \frac{[\tilde{\delta}_{l(E_k)\to h(E_i)} \cdot \tilde{\phi}^l_{E_k}](\kappa)}{\lambda^l_{\text{dec},E_k}(X)},
\end{aligned} \tag{4.21}$$

which is the main equation of the "2D MCEq" software developed in this thesis. Notably, in Equation (4.21), the Hankel-transformed diffusion kernels and the Hankel-transformed angular densities of the primaries are simply *multiplied*. The multiplication is performed elementwise with respect to frequency modes κ, which are chosen to be discrete in practical calculations.

The matrix form of Equation (4.21) is then defined analogously to the 1D MCEq equation (3.12), but separately for each κ:

$$\frac{\mathrm{d}\tilde{\boldsymbol{\phi}}_\kappa}{\mathrm{d}X} = -\boldsymbol{\nabla}_E[\mathrm{diag}(\boldsymbol{\mu}) \cdot \boldsymbol{\phi}_\kappa] + \left[(-\mathbb{I} + \tilde{\mathbf{C}}_\kappa)\boldsymbol{\Lambda}_{\mathrm{int}} + \frac{1}{\rho_{\mathrm{air}}(X)}(-\mathbb{I} + \tilde{\mathbf{D}}_\kappa)\boldsymbol{\Lambda}_{\mathrm{dec}}\right]\tilde{\boldsymbol{\phi}}_\kappa. \quad (4.22)$$

We note that the 1D MCEq equation is a special case of Equation (4.22) for $\kappa = 0$, as $J_0(0) = 1$ and Equation (4.14) becomes equivalent to our earlier definition of the total flux normalization from Equation (4.2). This implies that Equation (4.22) retains the computational complexity of Equation (3.12), up to a linear scaling by the number of the frequency modes (N_κ). One can then either choose to solve the N_κ equations (one for each κ) sequentially or in parallel, or to assemble the Hankel-transformed yield coefficients and angular densities into a more complex matrix structure[2]. The implementation developed in this thesis relies on the sequential solution of the N_κ equations but can easily be adapted to the user's preference. Our choice of the 2D MCEq matrix structure and the pipeline we followed to produce these matrices are described in detail in Chapter 5.

[2]Some possible structures are a tensor with κ being the third dimension in addition to the primary and the secondary particle energies, or a block-diagonal matrix with each block dedicated to a separate κ mode.

III

2D MCEq code

CHAPTER 5

2D MCEq matrices

5.1 Matrix structure

For the purpose of the low-energy atmospheric neutrino flux calculations, we use a fixed logarithmically spaced kinetic energy grid extending between 10 MeV and 10 TeV. We note that while 10 MeV is our lower energy limit *de jure*, we found that the 2D MCEq solutions for atmospheric neutrino fluxes are *de facto* valid only down to the energies of ~50 MeV. Energies higher than 10 TeV were not included as their (spectrum-weighted) contribution to the $\mathcal{O}$(GeV) neutrino flux is negligible. The bin width of the energy grid is set to $\Delta \log_{10} E_{\mathrm{kin}} = 0.1$ as in 1D MCEq, which results in $N_E = 60$ energy bins. Our Hankel frequency (κ) grid is also near-logarithmically-spaced, with $\kappa_{\mathrm{min}} = 0$, $\kappa_{\mathrm{max}} = 2000$, and a total of $N_\kappa = 24$ integer modes $\kappa \in [\kappa_{\mathrm{min}}, \kappa_{\mathrm{max}}]$. The flux of every particle species in 2D MCEq exists on the $(\kappa, E_{\mathrm{kin}})$ grid.

As the electromagnetic cascades are not included in 2D MCEq at the time of writing, the only particles that contribute to the coupled cascade equations (4.21) are those participating in the hadronic cascade development and atmospheric neutrino production. This includes 6 baryon species ($p/\bar{p}, n/\bar{n}$, and $\Lambda^0/\bar{\Lambda}^0$), 5 meson species ($\pi^\pm$, $K^\pm$, K^0_{L},), and 10 leptons ($\mu^\pm_{\mathrm{R/L}}$, $\mu^\pm$, $\nu_e/\bar{\nu}_e$, and $\nu_\mu/\bar{\nu}_\mu$), thus giving a total of $H = 21$ particles. The muons contribute 6 species, with each of $\mu^\pm$ contributing two polarizations: left-handed "L" and right-handed "R", as well as an unpolarized component (denoted as $\mu^\pm$ without a subscript). We stress that the polarized muon species correspond to the left-*helical* and the right-*helical* eigenstates $\mu^\pm_\uparrow$ and $\mu^\pm_\downarrow$ of Section 1.3.1, where we switched notation via $\mu^\pm_\uparrow \to \mu^\pm_{\mathrm{R}}$ and $\mu^\pm_\downarrow \to \mu^\pm_{\mathrm{L}}$. These species are **not** to be confused with the chiral eigenstates of the weak interaction. Given

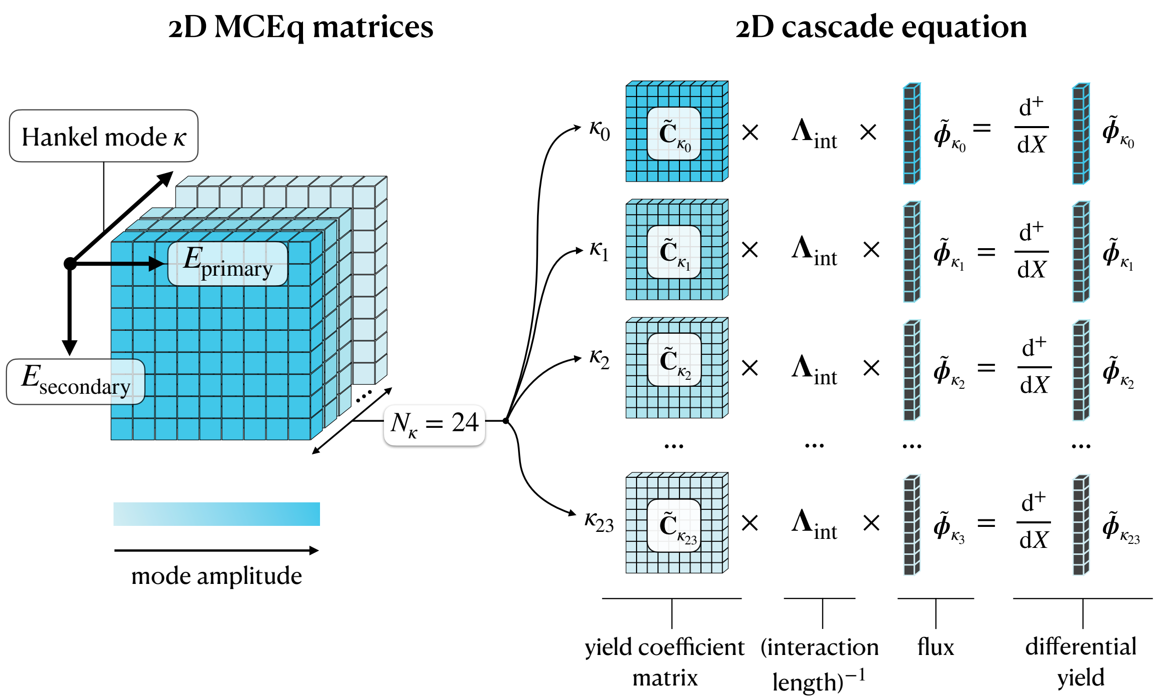

FIGURE 5.1 – *Left*: The structure of the 2D MCEQ yield coefficient matrices ($\tilde{\mathbf{C}}$) in the Hankel space. *Right*: 2D cascade equation in the Hankel space, formulated in terms of the individual Hankel modes κ_i (see Equation (4.22)).

H particle species, N_E energy bins, and N_κ Hankel frequency modes, the resulting dimension of the flux vector $\tilde{\boldsymbol{\phi}}$ is $N_\kappa \times (N_E \cdot H)$, which in our case amounts to 24×1260. The 2D MCEQ matrices themselves hold the "couplings" (yield coefficients) between pairs of primary and secondary particles, such that their dimension is $N_\kappa \times (N_E \cdot H) \times (N_E \cdot H) = 24 \times 1260 \times 1260$. We visualize the structure of a typical 2D MCEQ matrix in Figure 5.1. We also show how the individual "slices" of the yield coefficient matrix, $\tilde{\mathbf{C}}_{\kappa_i}$, multiply the Hankel-decomposed flux vectors, $\tilde{\boldsymbol{\phi}}_{\kappa_i}$, resulting in a differential increase in the flux of the secondary particles $\frac{\mathrm{d}^+}{\mathrm{d}X}\left[\tilde{\boldsymbol{\phi}}_{\kappa_i}\right]$ according to Equation (4.22). That the multiplication is done elementwise for the different discrete modes κ_i is the success of the convolution theorem (4.19).

5.2 EVENT GENERATION

The main computational advantage of the MCEQ code compared to the Monte Carlo simulations comes from the pre-generation of the particle yield coefficients, which is done outside of the user interface. The user receives the prepared interaction/decay matrices for solving Equation (3.12) (in the case of 1D MCEq) and Equation (4.22) (in the case of 2D MCEq). In that sense, the procedure of the 2D MCEq matrix production closely follows that of the 1D MCEq [1, 2]. It relies on the execution of a given event generator of hadronic interactions or decays and the histogramming of the corresponding particle yields within each channel. These histograms have two dimensions (primary and secondary particle energies, E_{prim} and E_{sec}) in 1D MCEq, whereas in 2D MCEq we add the Hankel mode κ as shown in Figure 5.1. Below, we describe how this $(\kappa, E_{\text{sec}}, E_{\text{prim}})$ grid is populated with events from event generators before it is made available to the user. In particular, Section 5.2.1 explains the event generation and matrix production procedure for the generic case of hadronic interactions and decays of particles without polarization treatment, while Sections 5.2.2 and 5.2.3 explain how the procedure is different when handling polarized muon production and decay.

5.2.1 *General case*

For each particle capable of producing secondaries (i.e. all particles in the list of section 5.1), we are running event generators to compute the respective secondary particle yields. For hadronic interactions, we consider the following hadronic interaction models: UrQMD [124], EPOS-LHC [126], Sibyll-2.3c [2, 125], and DPMJet-III 19.1 [62, 123]. These models are accessed via the impy interface [3]. For unstable particle decays, we run Pythia 8.306 [127]. Notable exceptions are the production of polarized muons in the two-body decays of $\pi^{\pm}$ and $K^{\pm}$, as well as the three-body decay of polarized muons. Neither of these scenarios can be simulated in Pythia, which generates events in the spin-averaged phase spaces, and therefore require special treatment.

Universally for all interaction/decay channels, we employ the following event generation and histogramming scheme. For all primaries falling into the kinetic energy bin k, we use the logarithmic center of that bin as the initial energy of the primary. For example, if the edges of the energy bin are $[E_{k'}, E_{k''}]$, then $E_k = \sqrt{E_{k'} \cdot E_{k''}}$ is assigned to the interacting/decaying primary particle. This particle then enters the event generator of choice with the four-momentum $p^{\mu}_{\text{prim}} = \langle E_k, 0, 0, \sqrt{E_k + 2E_k m_{\text{prim}}} \rangle$, i.e., moving along the positive z-axis. For hadronic interactions, we make the projectile collide with the nitrogen nucleus (^{14}N) at rest; including ^{16}O or other atmospheric nuclei as the targets results in negligible modifications to the secondary particle yields. For decays, we put the decaying particle at rest and then boost its daughters to the lab frame, applying the transformation rule in Equation (A.2).

In our pipeline, the energies of the secondaries/decay daughters are recorded in the same way as in 1D MCEq, i.e., by filling in the yield histograms in the $(E_{\text{sec}}, E_{\text{prim}})$ space (see Figure 3.2 for an example). To solve the 2D cascade equation (4.21), one needs to additionally derive the Hankel-transformed angular densities of the secondary particles, i.e., to discretize the yield coefficients $c_{l(E_k)\to h(E_i)}$ into the amplitudes $\tilde{\varsigma}_{l(E_k)\to h(E_i)}(\kappa)$ of the Hankel

particle	$\log_{10}\left(\frac{E_{k'}}{\mathrm{GeV}}\right)$ [$E_{k'}$ (GeV)]	$\log_{10}\left(\frac{E_{k}}{\mathrm{GeV}}\right)$ [E_{k} (GeV)]	$\log_{10}\left(\frac{E_{k'}}{\mathrm{GeV}}\right)$ [$E_{k''}$ (GeV)]
p	2.0 [100.0]	2.05 [112.2]	2.1 [125.8]
π^+	1.0 [10.0]	1.05 [11.2]	1.1 [12.6]
ν_μ	0.5 [3.2]	0.55 [3.5]	0.6 [4.0]

Table 5.1 – Energy grid settings for the event generation chain example. The three columns (from left to right) correspond to the left bin edge, the bin center, and the right bin edge of the respective particles on the MCEq kinetic energy grid.

modes κ. We will illustrate how this is done using the muon neutrino production chain from Figure 4.1, i.e., $p + {}^{14}\mathrm{N} \to \pi^+ + \mathrm{X}^* \to \nu_\mu + \mu^+$, focusing on the angular distributions of π^+ and ν_μ. As these angular distributions populate a discrete two-dimensional energy grid, we choose the primary proton and the secondary pion/neutrino energy bins as in Table 5.1 for this example. This choice reflects the characteristic energies for the low-energy neutrino production in air showers. We begin our simulation chain with a beam of protons incident at ^{14}N in the EPOS-LHC event generator, which returns the kinematic properties of the secondary particles produced in the inelastic scattering. This includes the π^+ of interest. The top left panel of Figure 5.2 shows the distribution of angles $\theta_{p\to\pi^+}$ that the secondary pions make with the primary proton axis. The number of entries n_{π^+} in the histogram (normalized to the number of the primary protons n_p) is equivalent to the total secondary pion yield $c_{p\to\pi^+}$ in this interaction channel, i.e., $n_{\pi^+} \equiv n_p \cdot c_{p\to\pi^+}$. Each of the secondary pions contributes a delta function $\underline{\delta}(\theta - \theta^j_{p\to\pi^+}), j \in [1, n_{\pi^+}]$, to the overall angular density[1]. The Hankel transform of the delta function has an analytical representation[2],

$$\mathcal{H}\left[\frac{1}{a}\underline{\delta}(\theta - a)\right](\kappa) = J_0(\kappa a), \tag{5.1}$$

meaning that the Hankel-space representation of an individual particle angular density can populate the κ-grid as soon as the respective event is generated in the Monte Carlo simulation. Then, thanks to the additivity of the Hankel transform, the sum of the Hankel-transformed delta functions $\underline{\delta}(\theta - \theta^j_{p\to\pi^+})$ asymptotically approaches the Hankel transform $\tilde{\varsigma}_{p\to\pi^+}(\kappa)$ of the underlying angular density $\varsigma_{p\to\pi^+}(\theta)$ of the secondary pions:

$$\tilde{\varsigma}_{p\to\pi^+}(\kappa) \overset{n_p\to\infty}{=} \frac{1}{n_p}\sum_{j=1}^{n_{\pi^+}} J_0(\kappa\theta^j_{p\to\pi^+}) \tag{5.2}$$

[1] Note that we used $\underline{\delta}$ to denote a Dirac delta function to distinguish it from the decay coefficient $\delta_{l\to h}$ used earlier in Equation (4.6).

[2] We scale the delta function centered at $\theta = a$ by a^{-1} to be consistent with the angular density definition in Equation (4.2).

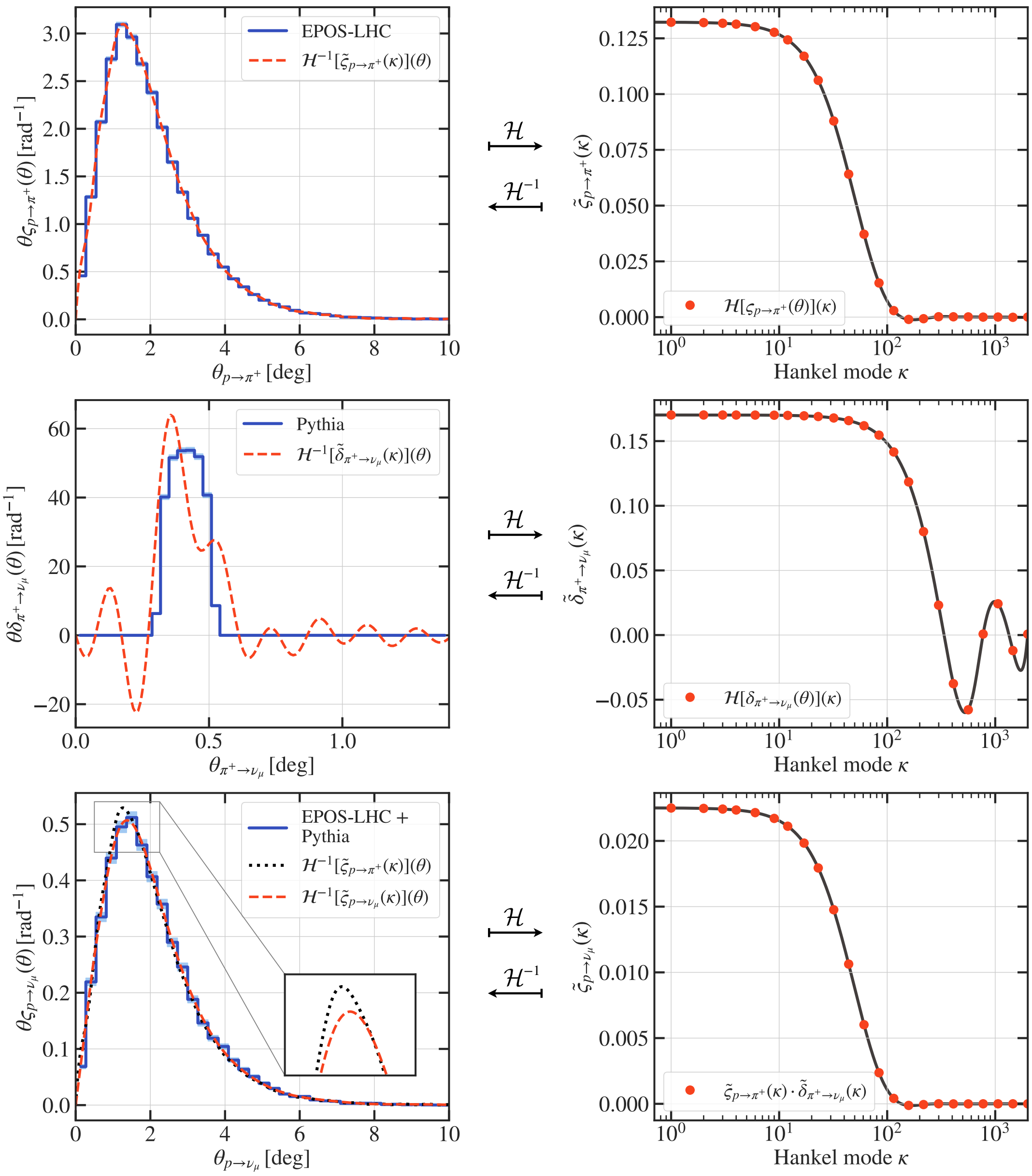

Figure 5.2 – *Top left*: angular distribution of the secondary pions in the p+^{14}N→ $\pi^+ + X^*$ process, as extracted from the EPOS-LHC event generator (solid blue line) and as obtained from the inverse Hankel transform (dashed red line) of the top right panel. *Top right*: Hankel transform of the angular distribution of the secondary pions (obtained directly using Equation (5.2)). *Middle*: same as top, but evaluated for daughter ν_μ in the $\pi^+ \to \mu^+ + \nu_\mu$ decay. *Bottom*: the application of the convolution theorem to the $p \to \pi^+ \to \nu_\mu$ chain: the inverse transform of the product of the Hankel transforms (top right and middle right) reconstructs the angular density of the tetriary neutrinos (bottom left). The dotted black line in the bottom left panel shows the appropriately normalized angular distribution of the secondary pions for comparison.

The angular density can therefore be expressed via the inverse Hankel transform as[3]

$$\varsigma_{p\to\pi^+}(\theta) \equiv \mathcal{H}^{-1}\left[\tilde{\varsigma}_{p\to\pi^+}(\kappa)\right] \overset{n_p\to\infty}{=} \frac{1}{n_p}\mathcal{H}^{-1}\left[\sum_{j=1}^{n_{\pi^+}} J_0(\kappa\theta^j_{p\to\pi^+})\right](\theta). \tag{5.3}$$

We emphasize that Equation (5.3) holds only in the limit of a large number of delta functions being summed, i.e., large Monte Carlo statistics. We prove this for toy functions in Appendix B. For that reason, we always generate 10^7 events for every energy bin of every primary particle to arrive at accurate angular density estimates of the secondaries via the delta function summation in the Hankel space[4].

The Hankel mode amplitudes $\tilde{\varsigma}_{p\to\pi^+}(\kappa)$ calculated via the delta function summation are shown in the top right panel of Figure 5.2. The respective inverse transform $\varsigma_{p\to\pi^+}(\theta)$ is overlayed with the original histogram of the secondary pion angles in the top left panel. In this representative example, two observations are of particular importance. First, the inverse Hankel transform as evaluated through Equation (5.3) matches the original (histogrammed) angular distribution of the pions very well. This provides an empirical validation to the Hankel transform as a tool to "compactify" the angular densities of secondary particles in hadronic interactions, as well as to our specific choice of the κ-grid. Second, from the top right panel of Figure 5.2, we notice that the amplitudes of the Hankel modes with $\kappa \geq 100$ become near-negligible. This means that the angular density of the ~10 GeV pions produced in the interaction of a ~100 GeV proton with ^{14}N is sufficiently wide so as not to involve the higher-frequency modes. This is not the case for all processes occurring in a typical air shower. For example, in the decay of the ~10 GeV pion to ~4 GeV muon neutrinos, the angular distribution of the latter is sharp-edged and only about 0.25° wide, as illustrated in the middle left panel of Figure 5.2. In this case, even κ as high as 2000 is not sufficient to accurately reconstruct the angular density $\delta_{\pi^+\to\nu_\mu}(\theta)$, and the inverse Hankel transform exhibits a lot of "ringing." However, this would only be concerning if we set to reconstruct the angular distributions of neutrinos in the decay of an infinitely narrow beam of pions. In a realistic air shower and at the energies of interest, the pions already get a reasonably wide angular distribution prior to decaying into neutrinos, which we saw in the proton-^{14}N scattering example. As the result, the neutrinos from the $p \to \pi^+ \to \nu_\mu$ chain (and all analagous processes) inherit the smooth angular distribution of the parent mesons, only slightly widening it as the result of convolution of $\varsigma_{p\to\pi^+}$ with $\delta_{\pi\to\nu_\mu}$. In the Hankel space, the equivalent explanation is the effective "disappearance" of the

[3] A more general expression for a process with a primary l and a secondary h can be obtained by replacing $p \leftrightarrow l$ and $\pi^+ \leftrightarrow h$.

[4] We have developed this density estimation method specifically for this study and are not aware of its mentions or applications in any other literature.

higher-frequency modes in $\tilde{\delta}_{\pi\to\nu_\mu}(\kappa)$ after multiplication with $\tilde{\varsigma}_{p\to\pi^+}$, which is effectively 0 at $k \geq 100$. This is an example of the convolution theorem application, which, following the inverse transform of $\tilde{\varsigma}_{p\to\pi^+}(\kappa)\cdot\tilde{\delta}_{\pi^+\to\nu_\mu}(\kappa)$, results in an accurate reconstruction of the ν_μ angular distribution from the Monte Carlo simulation chain[5]:

$$\varsigma_{p\to\nu_\mu}(\theta) = \mathcal{H}^{-1}\left[\tilde{\varsigma}_{p\to\pi^+}(\kappa)\cdot\tilde{\delta}_{\pi^+\to\nu_\mu}(\kappa)\right](\theta). \tag{5.4}$$

Thus, given its success in a representative example, our general method for populating the 2D MCEq matrices with event generator yields consists in the usual 1D MCEq histogramming of the primary and secondary energies supplemented with the delta function summation in the Hankel space.

5.2.2 *Production of polarized muons*

Since the Pythia event generator that we use to process most of the particle decays does not keep track of the particle spins, we use Equation (1.9) [96] to assign the muon helicities in the two-body decays of $\pi^\pm$ and $K^\pm$. We then convert the obtained helicities to probabilities of a muon being purely right-/left-handed ($h = \pm1$) via Equation (1.10), where these two states act as a basis in which we represent the entire population of muons with continuous helicities. Then, after $\pi^\pm$ and $K^\pm$ undergo a two-body decay in Pythia, we draw a number from a random uniform distribution in the $[0,1]$ interval and compare it to the evaluated probability of e.g. right-handedness. If the probability is larger than the number drawn, we keep the muon as right-handed (μ_R); otherwise, we keep it as left-handed (μ_L). The muons produced in the three-body decays of $K^\pm$ and K^0_L are considered unpolarized and fall into the generic "μ" category with the $h = 0$ label. The energy and angular distributions of all muon species are kept from Pythia. This way, we populate the $\tilde{\delta}_{K^\pm(\pi^\pm)\to\mu^\pm_{\mathrm{R,L}}}$ matrix blocks, following the procedure from Section 5.2.1.

5.2.3 *Polarized muon decay*

To compute the energy and the angular distributions of the daughters in the $\mu^-\to e^-\bar{\nu}_e\nu_\mu$ and the $\mu^+\to e^+\nu_e\bar{\nu}_\mu$ decays, we use the WHIZARD Monte Carlo [132] instead of Pythia. WHIZARD includes full spin correlations in particle decays and allows one to specify the direction of the parent muon spin. For each of $\mu^\pm$, we simulate two spin configurations: $\mathbf{s}_\mu = \langle 0,0,-1\rangle$ and $\mathbf{s}_\mu = \langle 0,0,+1\rangle$. In Figure 5.3, we show the double-differential distributions of the polarized μ^- decay secondaries as computed in WHIZARD and compared to the analytical prediction from Equation (1.11). We find a very good agreement between the two, which validates the usage of the WHIZARD Monte Carlo for processing the polarized muon decay at rest. To fill in the 2D MCEq matrices,

[5] Here we use the symbol ς to denote the angular density of neutrinos from the interaction+decay chain, even though we previously reserved this symbol for interactions only.

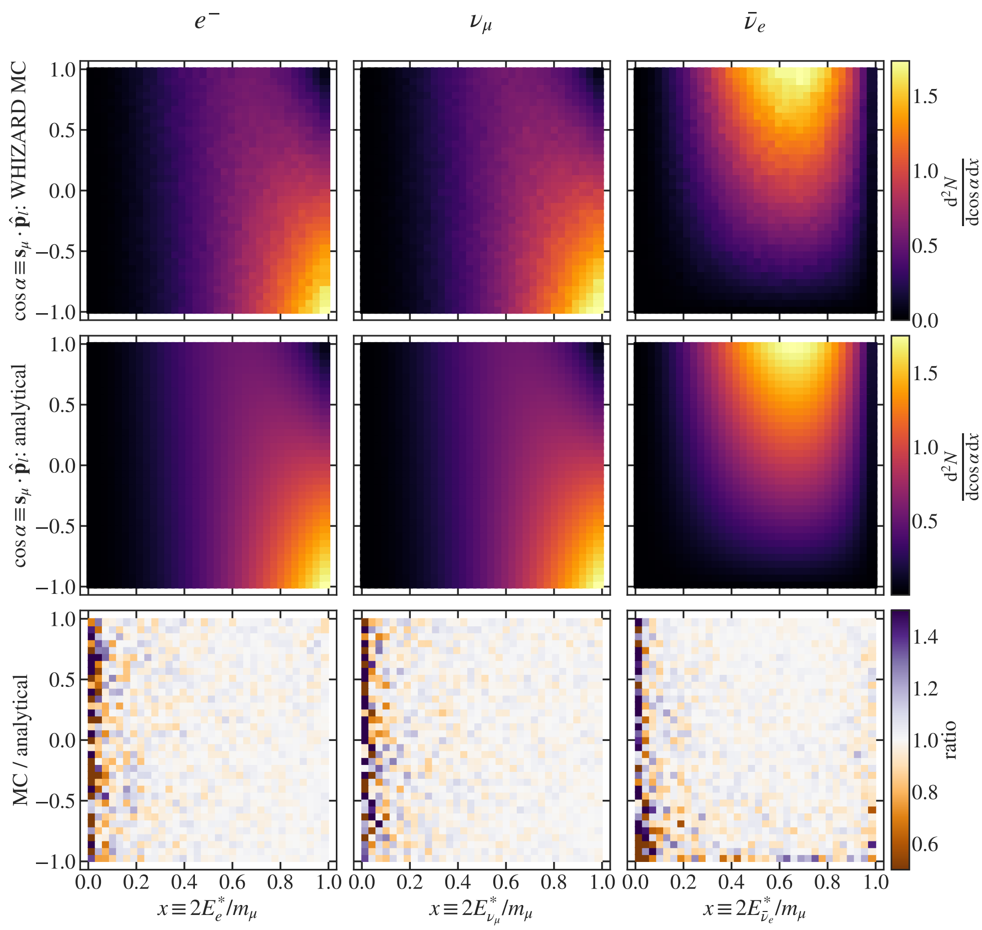

Figure 5.3 – Angular and energy spectra of the polarized μ^- decay secondaries as simulated in the WHIZARD Monte Carlo [132] (top) and computed analytically using Equation (1.11) (middle). The bottom panel shows the ratio of the binned Monte Carlo simulation over the analytical prediction.

we further boost the muons in the two simulated spin configurations to the required kinetic energy along the z direction, thereby obtaining the angular distributions and energy spectra of the secondaries for the left-handed and the right-handed muon parents in the lab frame. Example angular distributions of the $\bar{\nu}_e$ neutrinos resulting from the decay of a 5 GeV μ^- are shown in the left panel of Figure 5.4, where we compare the left-handed, the right-handed, and the unpolarized muon cases. Having restricted the neutrino energy to the $E < 2\,\mathrm{GeV}$ range, we see that both the angular and the energy distributions of neutrinos are visibly affected by the muon polarization. The differences between the three polarization scenarios propagate to the amplitudes of the Hankel modes, as seen from the right panel of Figure 5.4. As expected, the widest distribution (that of μ_L) decays the fastest in the Hankel space, and the

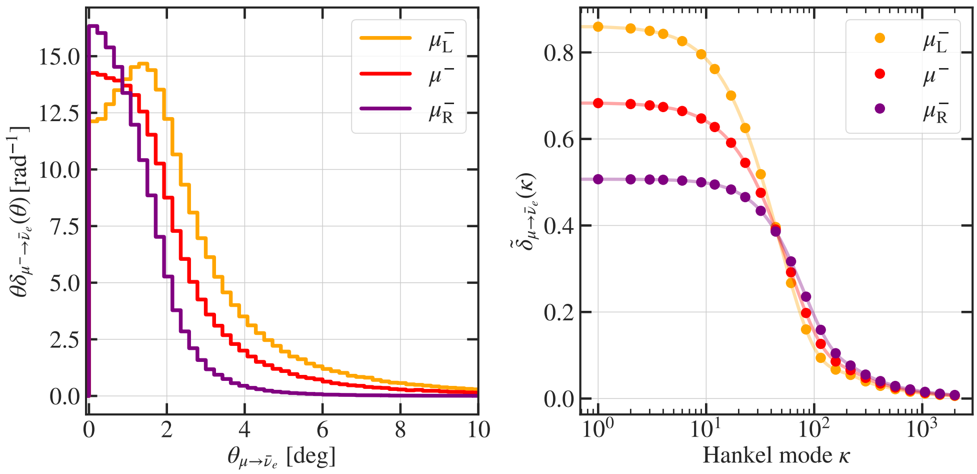

Figure 5.4 – *Left*: The angular distributions of the daughter $\bar{\nu}_e$ in the μ^- decay for three muon polarization configurations (left-handed μ_L^-, unpolarized μ^-, and right-handed μ_R^-). *Right*: Hankel transform of the angular distributions in the left panel, computed numerically via the delta function summation method (see Equation (5.2)).

narrowest one (that of μ_R) has a longer tail extending towards larger values of κ. Once properly histogrammed in terms of both parent muon and secondary neutrino energies, the Hankel amplitudes from Figure 5.4 become the values that we eventually store in the decay coefficients $\tilde{\delta}_{\mu^-_{R,L}\to\nu_\mu}$, $\tilde{\delta}_{\mu^-_{R,L}\to\bar{\nu}_e}$, $\tilde{\delta}_{\mu^+_{R,L}\to\bar{\nu}_\mu}$, and $\tilde{\delta}_{\mu^+_{R,L}\to\nu_e}$ of the 2D MCEq matrices.

5.3 Model interpolation

Following the procedure outlined in Section 5.2, we generate 10^7 events per every primary species and energy bin on the MCEq grid in each of the considered generators of hadronic interactions or decays. Except for UrQMD and DPMJet-III 19.1, our chosen hadronic interaction models are nominally valid down to the primary energies of $E_{\text{thresh}} \simeq 80\,\text{GeV}$, with decreasing applicability below this threshold. For that reason, we create interpolated matrices, where the low energy-compatible models (UrQMD or DPMJet-III 19.1) are used below E_{thresh}, and the high-energy models (either of Sibyll-2.3c, EPOS-LHC, or DPMJet-III 19.1) are used above E_{thresh}. At E_{thresh} and in the two adjacent energy bins (one on each side of E_{thresh}), a linear[6] spline is used to smoothly transition between the low-energy and the high-energy models. An example interpolation between the two energy regimes is shown in Figure 5.5 for the one-dimensional ($E_{\text{secondary}}, E_{\text{primary}}$) histograms of the π^+ yields in the p+^{14}N interactions, and in Figure 5.6 for the angular densities of π^+. This

[6] In this case, "linear" refers to the order-1 spline interpolation on the logarithmic MCEq energy grid.

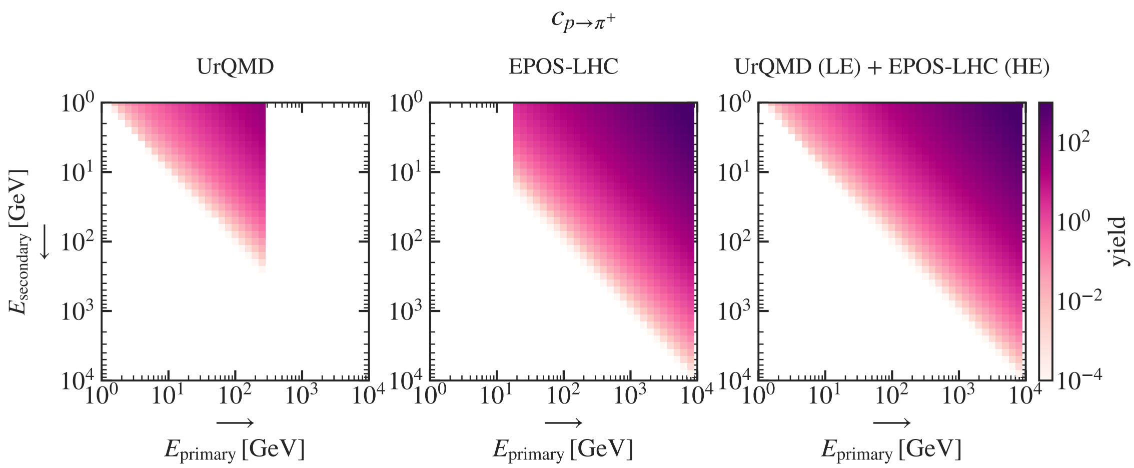

FIGURE 5.5 – Low-energy/high-energy model interpolation for the 1D MCEQ matrices.

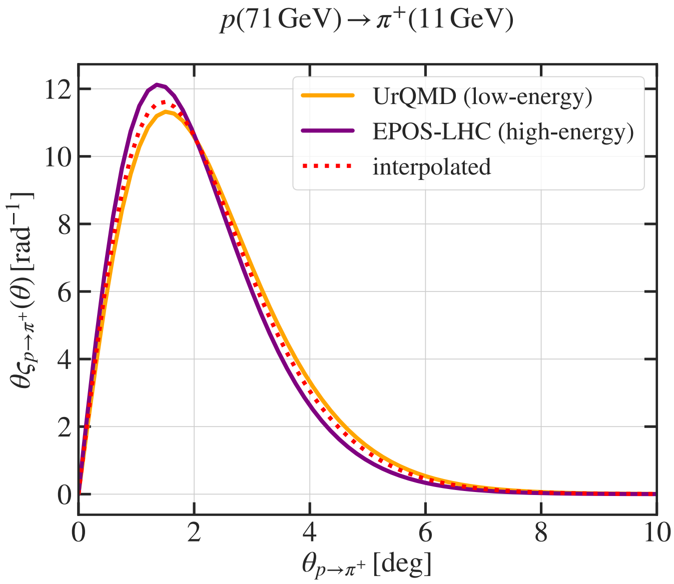

FIGURE 5.6 – Angular density of the secondary π^+ obtained in the p+^{14}N scattering, as simulated in the URQMD and the EPOS-LHC event generators. The protons in the MCEQ energy bin centered at ~70 GeV fall into the intermediate energy regime, where we use a linearly interpolated model as described in text.

step completes the generation of the 2D MCEQ matrices, and they are now ready to be used in the cascade equation solver as described in Chapter 6.

CHAPTER 6

Solving 2D cascade equations with MCEq

6.1 Solution in the Hankel space

6.1.1 *Forward integration*

To integrate Equation (3.12), the 1D MCEq code employs a forward Euler scheme, where the solution to

$$\frac{\mathrm{d}y}{\mathrm{d}X} = f(X, y(X)) \tag{6.1}$$

is computed iteratively in discrete steps of X:

$$y(X_{t+1}) = y(X_t) + f(X_t)\Delta X_t. \tag{6.2}$$

The step size ΔX_t is in general adaptive and depends on X, which is precisely the strategy employed in MCEq to accurately capture the variations in the atmospheric density $\rho_{\mathrm{air}}(X)$. In 2D MCEq, we adopt this strategy for every mode κ of Equation (4.22) separately. The longitudinal evolution of the Hankel-transformed angular densities of the cascade secondaries is therefore written as

$$\begin{aligned}\tilde{\boldsymbol{\phi}}_\kappa(X_{t+1}) &= \tilde{\boldsymbol{\phi}}_\kappa(X_t) - \Delta X_t \boldsymbol{\nabla}_E[\mathrm{diag}(\boldsymbol{\mu}) \cdot \boldsymbol{\phi}_\kappa(X_t)] \\ &+ \Delta X_t \left[(-\mathbb{I} + \mathbf{C}_k)\boldsymbol{\Lambda}_{\mathrm{int}} + \frac{1}{\rho(X_t)}(-\mathbb{I} + \mathbf{D}_k)\boldsymbol{\Lambda}_{\mathrm{dec}}\right]\tilde{\boldsymbol{\phi}}_\kappa(X_t),\end{aligned} \tag{6.3}$$

where X_t and $X_{t+1} = X_t + \Delta X_t$ are two successive slant depth values along the integration path. We thereby evolve the fluxes $\tilde{\boldsymbol{\phi}}_\kappa$ for each κ from $X \simeq 0$, which corresponds to the top of the atmosphere, to X_{final}, which corresponds to the Earth surface level. The exact value of X_{final}, and therefore the number of steps t needed to integrate Equation (6.3), varies depending on the cosmic ray primary axis inclination. Given the same altitude of production, the secondaries in the more horizontal showers have to traverse more atmosphere (compared to the vertical showers) before they hit they ground. For that reason, the near-horizontal showers always take more steps/time to evolve. Equation (6.3) is the main computational task of 2D MCEq which is executed by the user at runtime, as opposed to the pre-generation of the yield matrices, which are made available to the user. Once $\tilde{\phi}(X_{\text{final}}, \kappa)$ is calculated, the final step is to reconstruct the angular densities of $\phi(X_{\text{final}}, \theta)$ using the inverse Hankel transform.

6.1.2 *Muon multiple scattering treatment*

An additional effect not explicitly included in Equation (6.3) is that of the Coulomb scattering of charged particles off of the atomic nuclei in the atmosphere. In the limit of a large number of scatters per unit length traversed by a charged particle, this process is called *multiple scattering*, and the total angular deflection is described by the Molière theory [133]. The calculation by Molière includes full quantum mechanical treatment of the scattering in the Coulomb field of the electron-screened nucleus and yields a power series expansion for the probability density of the deflection angle θ [133, 134]. Including higher terms in the series corresponds to a more accurate treatment of the tails of the distribution. However, to within 2% accuracy, occasional deflections by large angles can be neglected [55], and only the first term in the expansion is kept. This results in a Gaussian approximation of the probability P of a charged projectile deflecting by the space angle θ[1] after traversing ΔX of the atmospheric slant depth:

$$P(\theta, \Delta X) = \frac{1}{\pi \theta_s^2 \Delta X} \cdot \exp\left[\frac{-\theta^2}{\Delta X \theta_s^2}\right], \tag{6.4}$$

where $\theta_s^2 = \frac{1}{\lambda_s}\left(\frac{E_s}{E_{\text{pr,lab}}\beta_{\text{pr}}}\right)^2$, $E_s = 0.021\,\text{GeV}$, $\lambda_s = 37.7\,\text{g}\,\text{cm}^{-2}$, $E_{\text{pr,lab}}$ is the total projectile energy in the lab frame, and β_{pr} – its lab-frame Lorentz velocity factor [55, 135, 136]. In principle, all charged particles (including hadrons) are subject to Coulomb scattering; however, since inelastic scattering dominates the propagation of high-energy hadrons in the atmosphere, the Monte Carlo codes such as CORSIKA include the effect of the Coulomb scattering only

[1] Here we follow the terminology of [135], where the space (unprojected) angle θ is contrasted with the plane (projected) angles θ_x and θ_y, such that $\theta^2 \approx \theta_x^2 + \theta_y^2$. Our $P(\theta, \Delta X)$ is normalized so that $\int_0^{2\pi}\int_0^{\pi/2} P(\theta, \Delta X)\theta\, \mathrm{d}\theta\, \mathrm{d}\varphi = 1$, which is why the normalization factor in Equation (6.4) is different from that of [55].

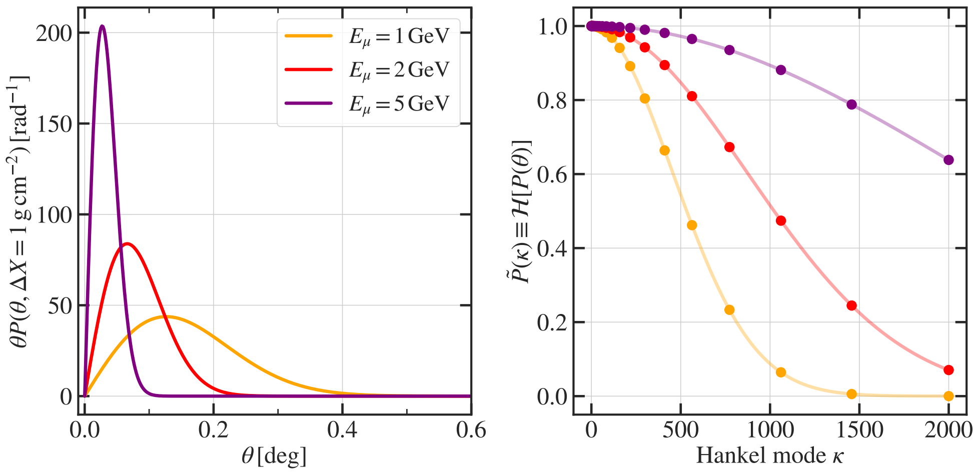

Figure 6.1 – *Left*: Gaussian approximation of the muon deflection angles due to their multiple scattering on atmospheric nuclei (see [55, 134, 135] and Equation (6.4)). *Right*: Hankel transform of the angular distributions in the left panel.

for muons [55]. We adopt the same approach in this work and implement the Gaussian approximation (6.4) in MCEq. In the left panel of Figure 6.1, we show several representative probability densities computed according to Equation (6.4). For illustration, we use $\Delta X = 1\,\mathrm{g\,cm^{-2}}$. In general, however, ΔX varies with X in response to the longitudinal atmospheric density variations, and the width of the muon multiple scattering kernel is variable. While in just $1\,\mathrm{g\,cm^{-2}}$ the expected muon deflection is small ($\mathcal{O}(0.1°)$ at GeV energies), this effect accumulates with the slant depth and results in a noticeable shift of the sea-level muon angular distribution especially in horizontal showers. To incorporate this additional diffusion kernel into the solution of Equation (4.21), we find the Hankel transform of Equation (6.4):

$$\tilde{P}(\kappa, \Delta X) = \exp\left[\frac{-\kappa^2 \Delta X \theta_s^2}{4}\right], \tag{6.5}$$

which is shown in the right panel of Figure 6.1. Equation (6.5) is scaled so that the overall normalization of the muon angular distribution (represented by the $\kappa = 0$ mode) is left intact, which in practice means that the muon energy spectrum is unaffected by the multiple scattering. This is a fair approximation given that the atmospheric nuclei are much heavier than the muon [55]. Since the muon energies are not affected, we can directly multiply Equation (6.5) by the Hankel amplitudes of the muon angular distributions, ϕ_κ^μ [2] after each integration step ΔX. This way, the simplified muon multiple scattering model becomes a natural part of the matrix cascade equations.

[2]This applies to all of the muon species, i.e. $\mu_L^\pm, \mu_R^\pm$, and $\mu^\pm$.

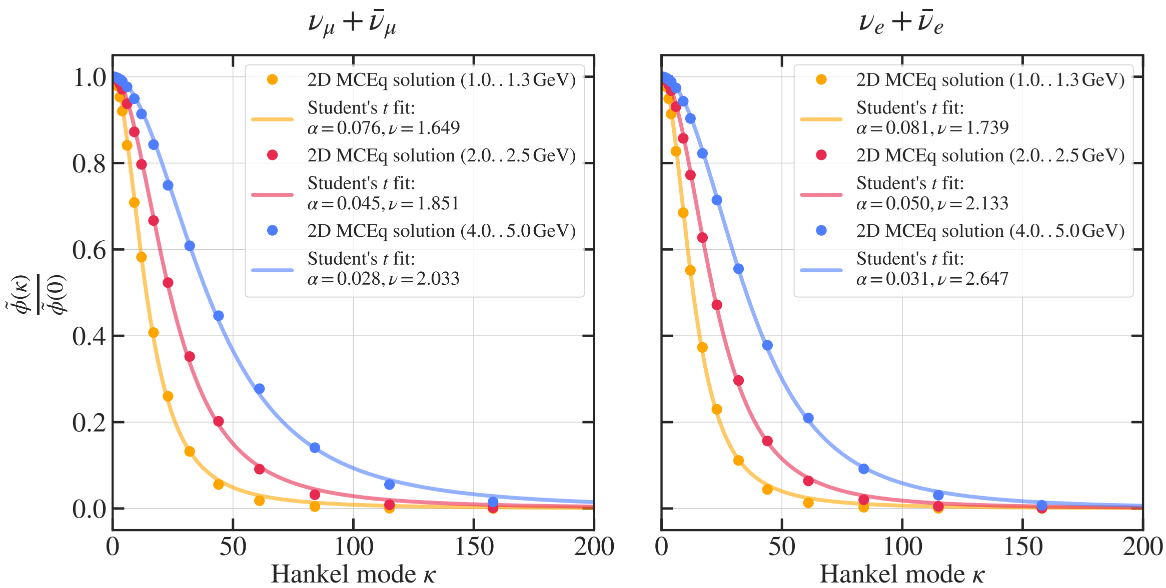

Figure 6.2 – Normalized Hankel amplitudes of the neutrino angular distributions in three different energy bins at the Earth's surface, as computed via 2D MCEq by evolving a 100 GeV proton shower incident at 30°. The markers represent the discrete 2D MCEq solutions in the Hankel space, while the solid lines correspond to the fits with the Student's t probability distribution function (6.7).

6.2 Inverse Hankel transform and solution reconstruction

After the final integration step, the 2D MCEq solver returns the state vector $\tilde{\phi}(X_{\mathrm{final}}, \kappa)$, which contains the flux amplitudes in the Hankel frequency space for all participating cascade particles on the MCEq energy grid. In Figure 6.2, we show example Hankel amplitudes of the $\nu_\mu + \bar{\nu}_\mu$ and $\nu_e + \bar{\nu}_e$ angular distributions obtained after solving Equation (4.22) for a 100 GeV proton shower incident at the zenith angle of 30°[3]. To obtain the solutions as a function of the angle from the shower axis, one needs to further apply the inverse Hankel transform:

$$\begin{aligned}\phi(X_{\mathrm{final}}, \theta) = \mathcal{H}^{-1}\left[\tilde{\phi}(X_{\mathrm{final}}, \kappa)\right](\theta) &\equiv \int_0^\infty \tilde{\phi}(X_{\mathrm{final}}, \kappa) J_0(\kappa\theta)\kappa \,\mathrm{d}\kappa \\ &\simeq \int_0^{\kappa_{\max}} \tilde{\phi}(X_{\mathrm{final}}, \kappa) J_0(\kappa\theta)\kappa \,\mathrm{d}\kappa.\end{aligned} \tag{6.6}$$

The κ grid in 2D MCEq is discrete, and the modes are nearly logarithmically spaced. To accurately compute the integral in Equation (4.15), one needs to

[3]This corresponds to $X_{\mathrm{final}} \approx 1200\,\mathrm{g\,cm^{-2}}$ at the surface, depending on the choice of the atmosphere.

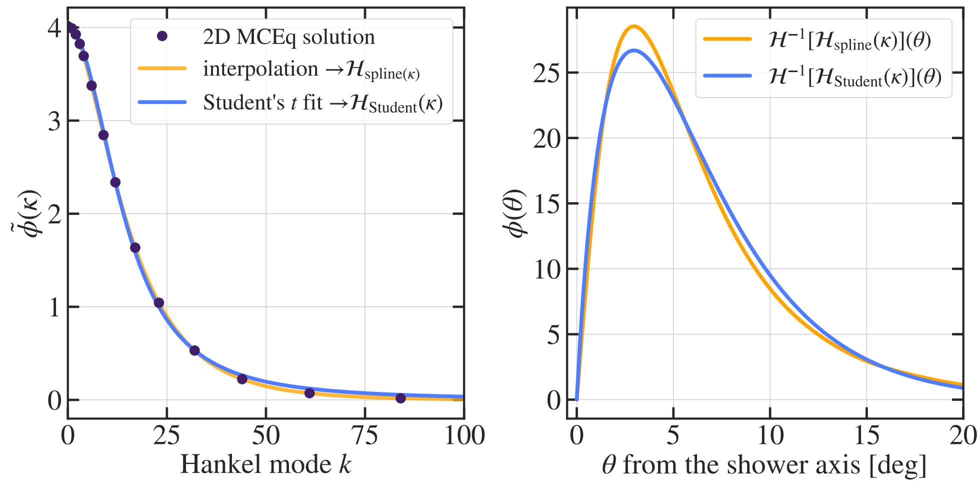

Figure 6.3 – *Left*: Hankel-space 2D MCEq solutions to Equation (4.22) for the 1.0..1.3 GeV $\nu_\mu + \bar{\nu}_\mu$ neutrinos at the Earth's surface, computed with the same initial conditions as in Figure 6.2. The solid lines show the two different continuous approximations to the discrete amplitudes $\tilde{\phi}(\kappa)$, as described in text. *Right*: angular densities of $\nu_\mu + \bar{\nu}_\mu$ obtained via the inverse Hankel transform of the left panel.

come up with a continuous approximation of $\tilde{\phi}(X_{\mathrm{final}}, \kappa)$, for which we have explored two methods. The first method is fitting the Student's t probability distribution function [137–139] to the discrete Hankel amplitudes, as shown in Figure 6.2. The Student's t function is defined as

$$f(\kappa|\alpha,\nu) = \frac{\Gamma\left(\frac{\nu+1}{2}\right)}{\sqrt{\pi\nu}\,\Gamma\left(\frac{\nu}{2}\right)}\left(1 + \frac{(\alpha\kappa)^2}{\nu}\right)^{-\frac{(\nu+1)}{2}}, \tag{6.7}$$

where Γ is the gamma function, ν is the degrees-of-freedom parameter, and α is the scaling parameter we introduced to account for the different widths of the distributions. We find that all of the Hankel space solutions at $\mathcal{O}(\mathrm{GeV})$ energies are well-fit by the Student's t function. If all of the angular distributions of the MCEq cascade secondaries at all altitudes were well-described by Equation (6.7), only two parameters (α and ν) would be required to explain the shapes of the angular distributions. In this case only three Hankel modes would be necessary to uniquely determine α and ν and find the continuous functional form of $\tilde{\phi}(\kappa)$. Since we are not aware of the *a priori* reason why the solutions to the two-dimensional cascade equation would always result in Student's t-like functions, we have compared this method to a straightforward cubic spline in the Hankel space. Figure 6.3 compares the two methods in both the Hankel space and the real (angular) space. We see that while the Student's t fit gives a strikingly good qualitative representation of the overall shape of $\tilde{\phi}(\kappa)$, it is still only an approximation which is optimal in the least-squares sense and is not designed to pass through all the points exactly. The spline interpolation, on the other hand, by construction returns the input $\tilde{\phi}(\kappa)$ amplitudes at the spline knots. The differences between the two methods can already be seen in the Hankel space but are even more visible in the angular space, where the inverse Hankel transform of the spline interpolation results in a more peaked/narrower angular distribution compared to the Student's t fit. Given that the spline interpolation matches the input Hankel amplitudes better, and is capable of capturing the negative amplitudes[4] as in the middle panel of Figure 5.2, we expect it to be a better estimator of the true angular density. While the ground truth of the neutrino angular densities is not known, it is possible to put the two methods to test using a toy function. We report the results of this test in Appendix B (Figure B.3), which confirm that the spline interpolation does in fact yield a more accurate angular density estimate. We therefore proceed with this method for the reconstruction of the angular-space solutions of 2D MCEq, evaluating the cubic spline on an oversampled κ grid to form a continuous approximation. The different oversampling resolutions n_{oversamp} are explored in Figure B.4; in this work, we settle on a linearly spaced grid of 10,000 points[5] between $\kappa_0 = 0$ and $\kappa_{23} = 2000$ for the evaluation of the integral in Equation (6.6).

We note that the reconstruction of angular densities of high-energy secondaries (with kinetic energies of 10 GeV and above), as well as those created very early in the cascade evolution, must be treated with care if the starting angular distribution of the primaries is narrow (e.g. delta function-like). In the high-energy regime, the secondaries are created very close to the primary particle axis, while in the low-X regime, the cascade has not yet had a chance to sufficiently spread in θ. This means that the angular distributions of such secondaries will be too narrow to be accurately reconstructed even with $\kappa_{\mathrm{max}} = 2000$, and the direct application of Equation (6.6) may result in the characteristic "ringing." We therefore recommend that the method described in this section is applied to reconstructing the angular distributions of $\lesssim 10$ GeV secondaries at slant depths of several kilometers into the atmosphere, and that the 1D approximation is used at high energies/altitudes.

[4] This is not the case for the Student's t function, which is positive for all κ.
[5] This corresponds to $n_{\mathrm{oversamp}} = 5$.

IV

Benchmarking and interpretation

CHAPTER 7

Benchmarking against CORSIKA

7.1 Experimental setup

To validate our solutions to the two-dimensional matrix cascade equations via 2D MCEq, we use the CORSIKA v7.7410 Monte Carlo code [55] as a benchmark. We aim to compare the angular distributions of the GeV-scale atmospheric neutrinos and muons generated in the cosmic-ray induced air showers. All of our simulations are run for a single angle of incidence of the cosmic ray primary flux, and the secondary particle angular distributions are computed with respect to the primary particle axis.

To make these comparisons as fair as possible, we effectively disable[1] the geomagnetic field in CORSIKA by setting $B_x = B_z = 10^{-5}\,\mu\mathrm{T}$. This is done because the geomagnetic field and the respective curving of the charged particle trajectories are not implemented in 2D MCEq at the time of writing. We also match the choice of hadronic interaction models by using UrQMD [124] as the low-energy model and EPOS-LHC [126] as the high-energy model in both CORSIKA and 2D MCEq. The transition energy is set to the default value of 80 GeV, which means a sharp transition between the two hadronic interaction models in CORSIKA and a smooth interpolation between the models in 2D MCEq (see Section 5.3). Some discrepancies between the two codes are therefore possible due to the different implementations of the

[1] CORSIKA requires $|\mathbf{B}| > 0$, which is why we set the individual components to negligibly small values instead of 0.

low-energy/high-energy model transition as well as the different low-energy model versions[2].

Our typical setup for the lepton flux benchmarking consists of a proton primary incident onto the Earth's atmosphere at a certain inclination angle θ_0. We test both vertical ($\theta_0 = 0°$) and inclined ($\theta_0 \in \{30°, 60°, 80°\}$) showers; for $\theta_0 \geq 60°$, we use CORSIKA compiled with the CURVED option. The energy of the proton either is fixed at a certain value (e.g. 100 GeV) or follows a spectrum with a realistic power-law dependence (e.g. $\propto E^{-2.7}$). In CORSIKA, the azimuthal angle of incidence is fixed at $\varphi_0 = 0$ for concreteness in the computation of space angle between the primary proton and the secondary lepton directions. The height of the first interaction of the proton with the atmospheric nuclei is set to 112.8 km in both MCEq and CORSIKA. The atmospheric density as a function of the slant depth X is modelled according to the Linsley parametrization of the US Standard atmosphere [55]. The continuous energy losses of the charged particles due to ionization follow the Bethe-Bloch prescription [135, 140] in both codes, and the Gauss approximation (as per Section 6.1.2) is employed for muon multiple scattering.

For each considered permutation of initial conditions and hadronic interaction models in the above setup, we simulate ~1 million events in CORSIKA with different random seeds. This lets us gather enough statistics for the low-energy muons and neutrinos at several observation altitudes. The corresponding binned angular distributions are compared directly to the angular probability densities obtained with 2D MCEq by solving Equation (4.22).

7.2 BENCHMARKING RESULTS

In this section, we present the results of the MCEq-CORSIKA comparisons for three representative sets of initial conditions:

- 100 GeV proton shower incident at 30° (Figures 7.1 and 7.2);
- $E^{-2.7}$ proton spectrum sampled between 10 GeV and 10 TeV and incident at 30° (Figures 7.3 and 7.4);
- 100 GeV proton shower incident at 80° (Figures 7.5 and 7.6),

as simulated with the UrQMD+EPOS-LHC hadronic model combination. The rest of the results exhibit similar features and are reported in Appendix C. We provide both the angular distributions and the energy spectra of $\nu_e + \bar{\nu}_e$, $\nu_\mu + \bar{\nu}_\mu$, and $\mu^- + \mu^+$, where the energy spectra are extracted from 2D MCEq as the $\kappa = 0$ mode of the 2D cascade equation solution (see Section 4.2.2). For all showers with the 60° inclination or less, the comparisons are performed at 3 observation altitudes (15 km, 5 km, and 0 km above the Earth's surface) and in 3 energy bins (centered at ~1, 2, and 5 GeV). For showers with a larger inclination, only the solutions at the Earth's surface ($h = 0$ km) are recorded.

[2] CORSIKA uses the older UrQMD-1.3, while our 2D MCEq matrices were produced with the newer UrQMD-3.4 model accessible via the impy interface [3].

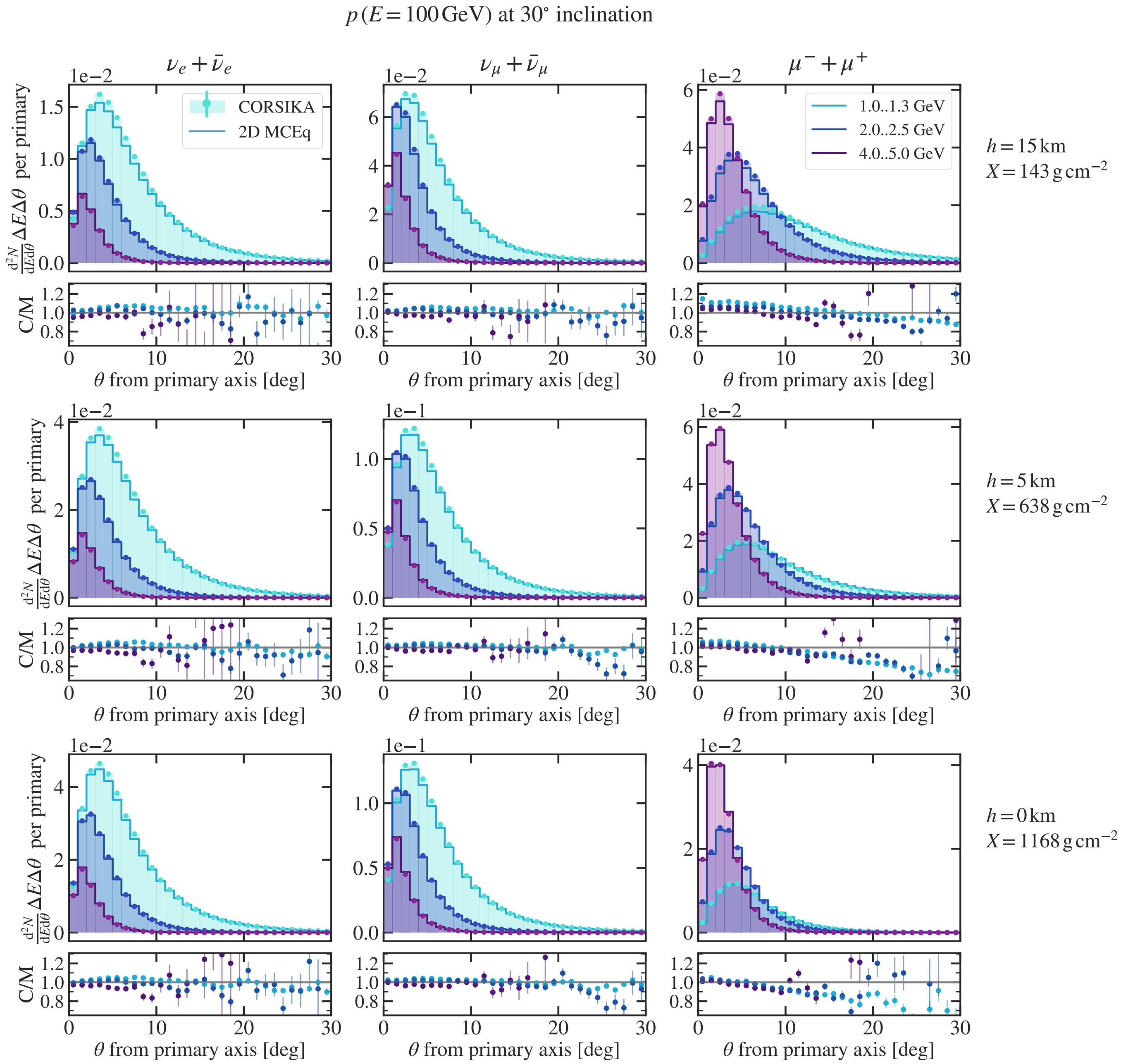

FIGURE 7.1 – Angular distributions of atmospheric leptons in a proton-induced air shower ($E_0 = 100\,\mathrm{GeV}$, $\theta_0 = 30°$), as computed numerically in 2D MCEQ (solid line) and simulated in the CORSIKA Monte Carlo (filled histograms with errorbars). The angle θ on the x axis is the angle a given secondary makes with the direction of the primary proton. The different colors correspond to the different energy bands, and the bottom sub-panel in each plot shows the ratio of CORSIKA ("C") to MCEQ ("M").

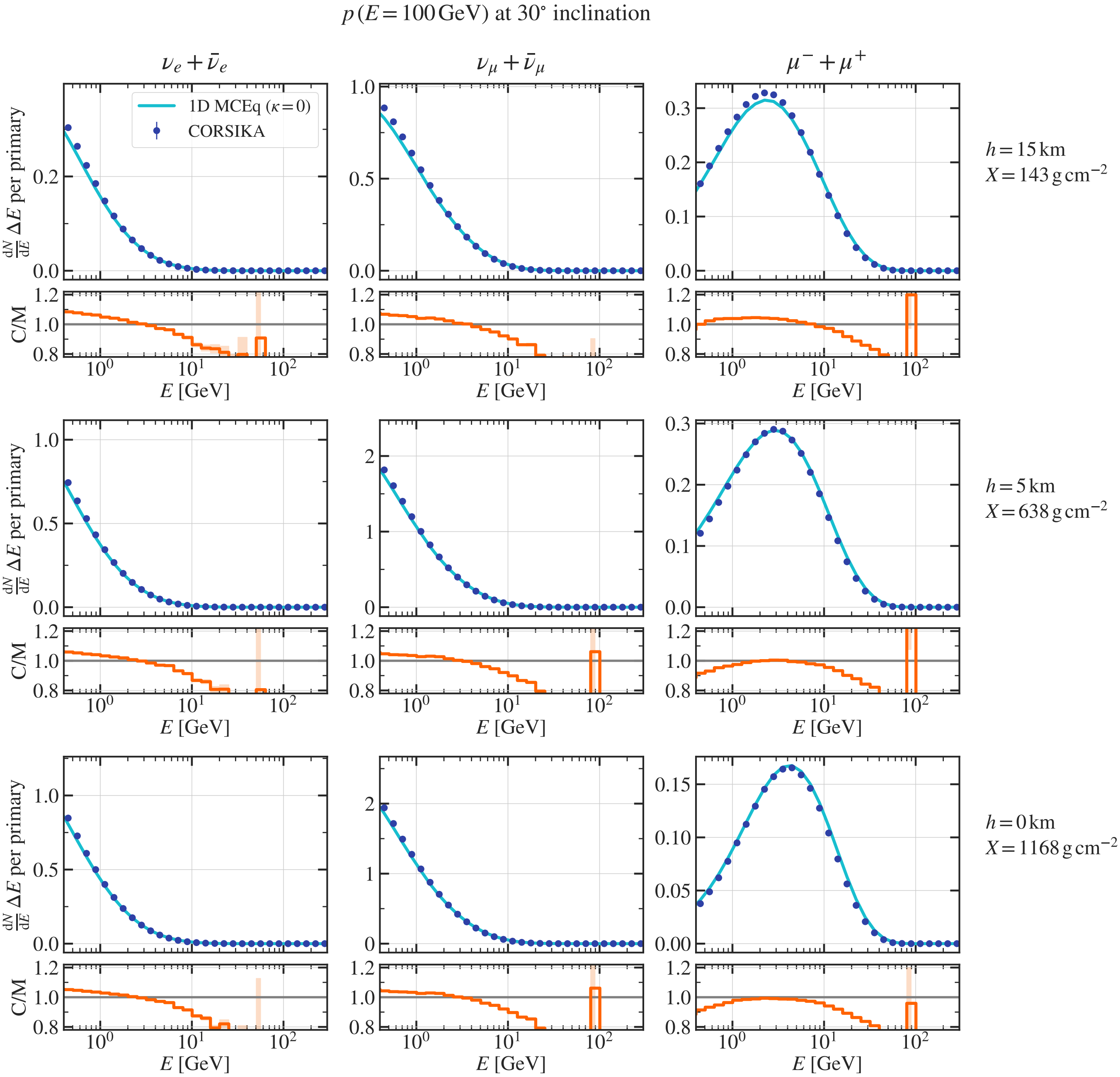

Figure 7.2 – Energy spectra of atmospheric leptons in a proton-induced air shower (E_0 = 100 GeV, θ_0 = 30°), as computed numerically in 1D MCEq (solid line) and simulated in the CORSIKA Monte Carlo (filled markers). Here, "1D MCEq" corresponds to the κ = 0 slice of the 2D MCEq solution. The bottom sub-panel in each plot shows the ratio of CORSIKA ("C") to MCEq ("M").

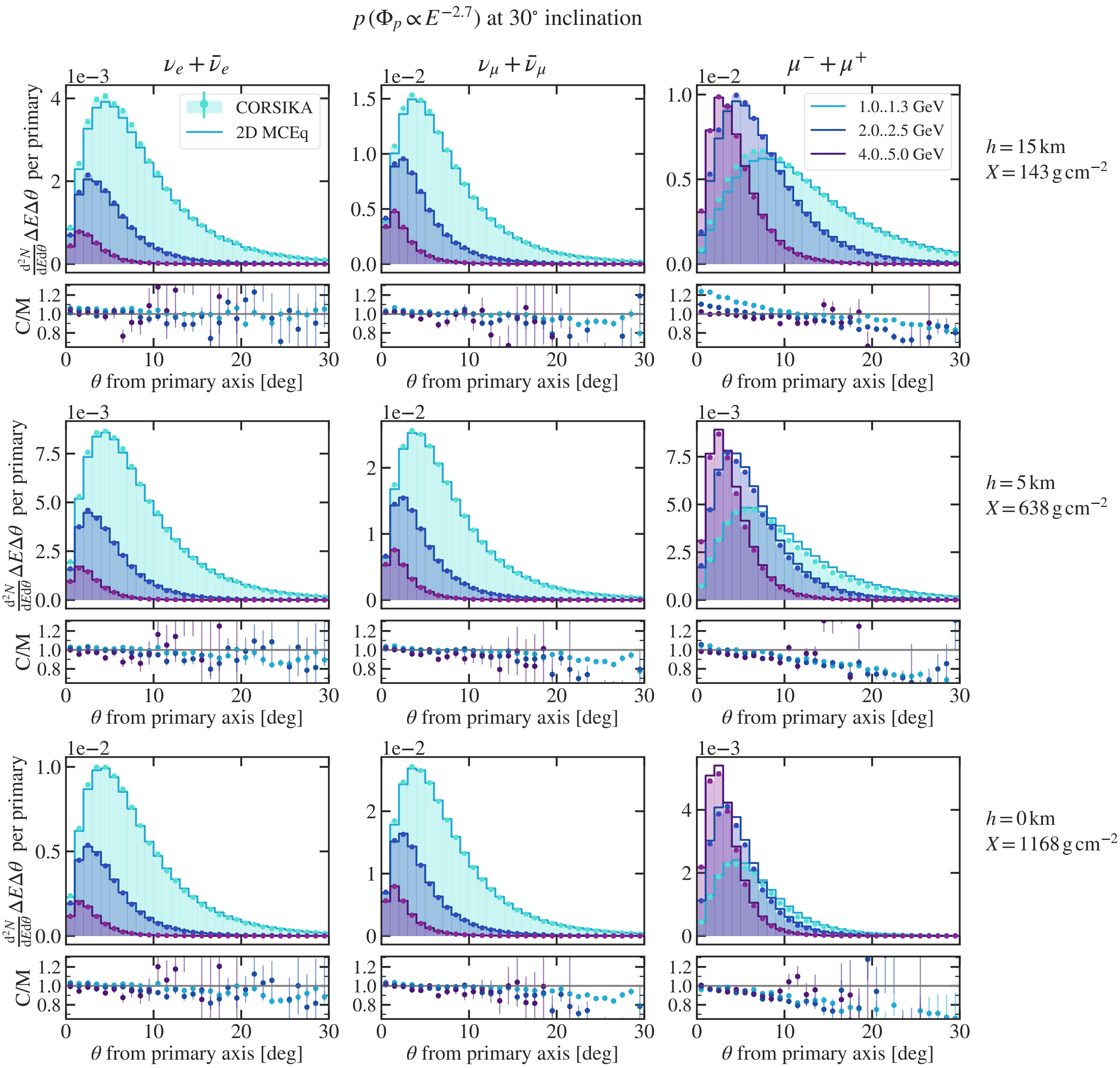

FIGURE 7.3 – Same as Figure 7.1, but for the initial proton energies sampled from the $E^{-2.7}$ spectrum.

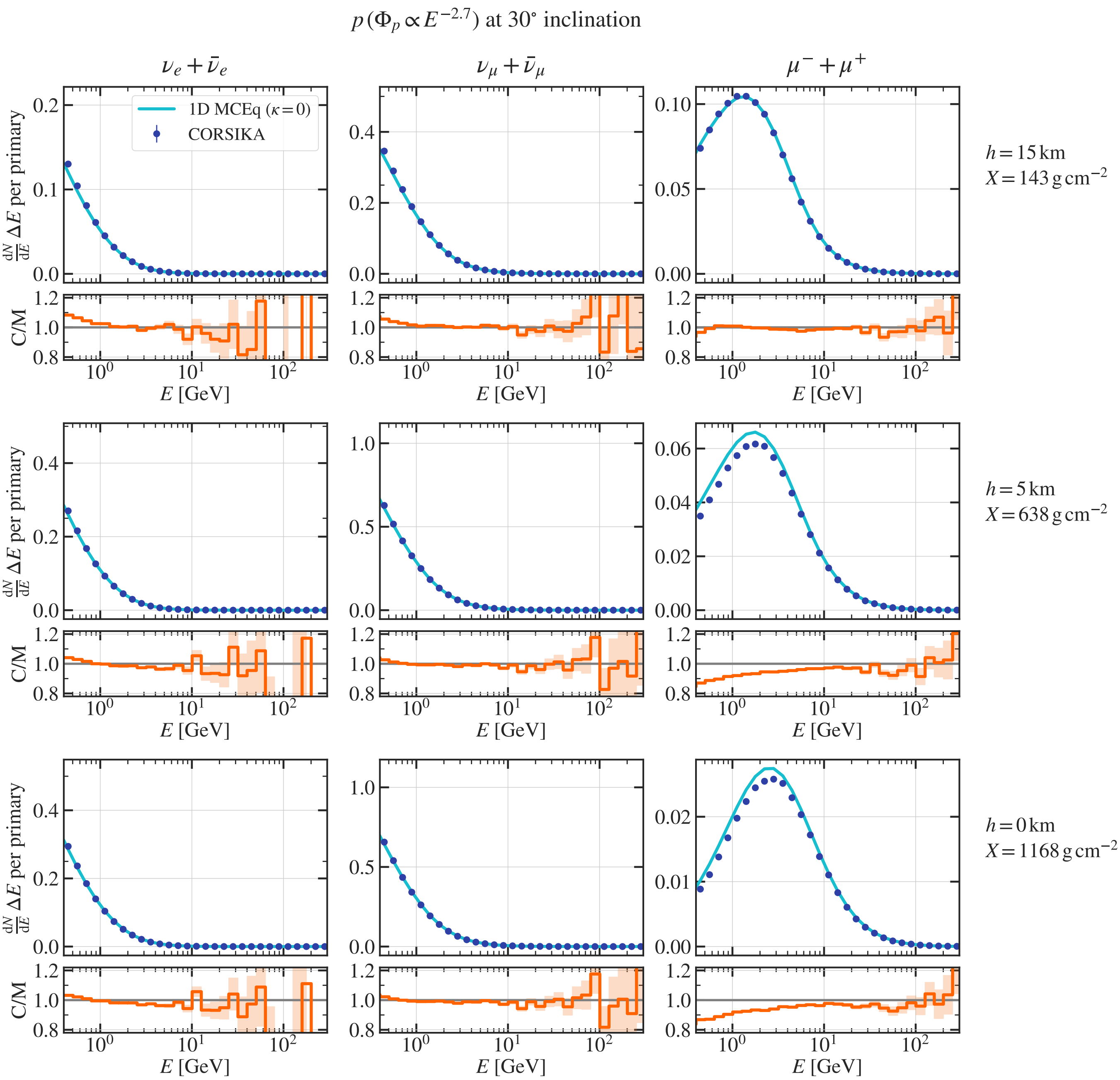

FIGURE 7.4 – Same as Figure 7.2, but for the initial proton energies sampled from the $E^{-2.7}$ spectrum.

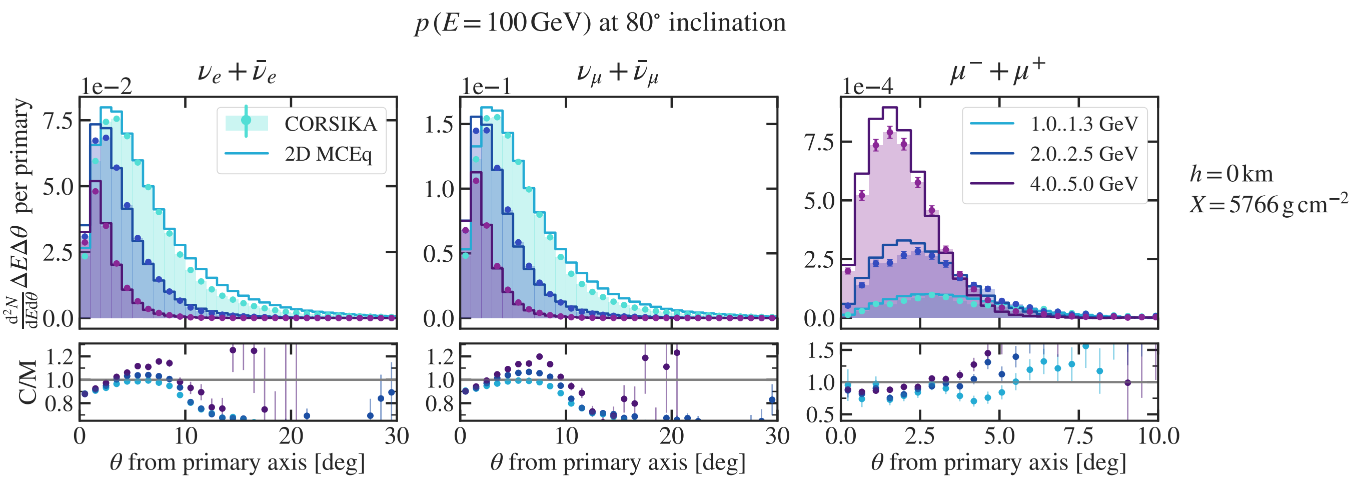

FIGURE 7.5 – Same as Figure 7.1, but for the 80° shower inclination.

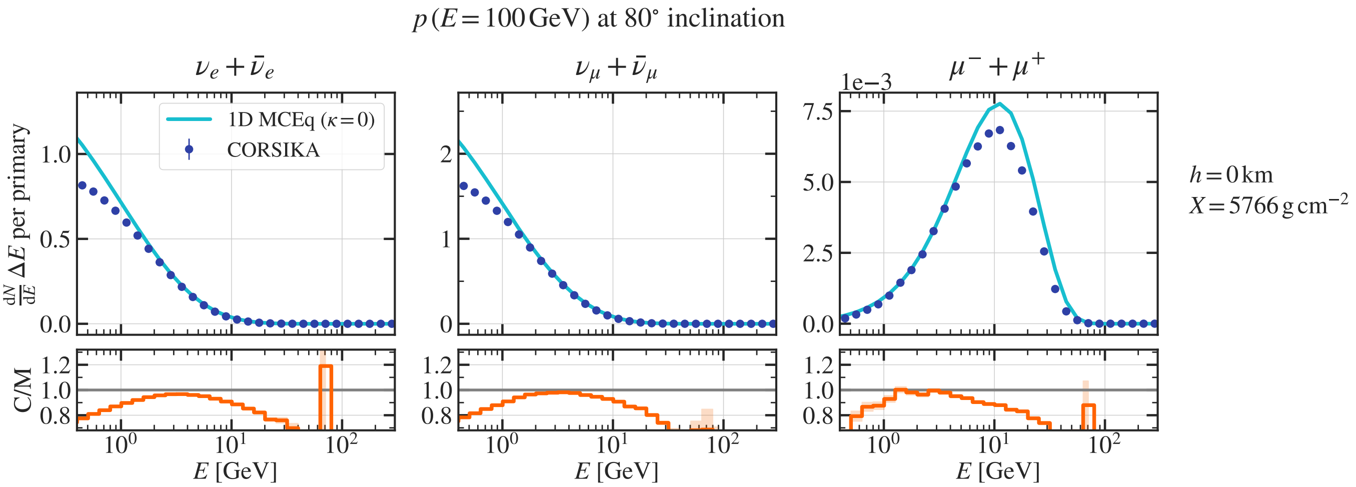

FIGURE 7.6 – Same as Figure 7.2, but for the 80° shower inclination.

We make several observations from the presented cross-checks:

- The angular distributions of $\mathcal{O}$(GeV) neutrinos agree very well between CORSIKA and 2D MCEQ at the medium (30°) inclination at all observation altitudes for both the fixed-energy proton and the power law proton spectrum initial conditions, with at most 5 – 10% discrepancies between the two codes. The same behaviour is observed for the 0° and the 60° inclinations, which we show in Figure C.2 and Figure C.3, respectively.
- The neutrino energy spectra at the ≤ 60° inclinations are also in a very good agreement between CORSIKA and MCEQ in the 1–10 GeV regime, with at most 10% discrepancies. However, the CORSIKA-to-MCEQ

ratio shows a clear energy dependence in the fixed-energy shower case, and the discrepancy increases further at energies above 10 GeV. For the $E^{-2.7}$ spectrum, the energy dependence of the CORSIKA-to-MCEQ ratio is a lot milder. The disagreements in the energy spectra between CORSIKA and 1D MCEQ have been previously discovered and investigated in detail by the MCEQ development team[3] (see e.g. Figure C.9), and their origin is not fully understood.

- At medium inclinations, the angular distributions of muons exhibit a characteristic tilt in the CORSIKA-to-MCEQ ratio, with increasingly smaller C/M values at larger angles with respect to the shower axis. This tilt exists to a very small degree also in the neutrino angular distributions (e.g. in Figure 7.4), which is natural since some of the neutrinos come from the muon decays.
- Among all cases presented, the near-horizontal showers exhibit the largest discrepancy between CORSIKA and MCEQ, which differ by as much as 20% when comparing neutrino angular densities at the Earth's surface. The ratio of the estimated angular densities acquires a strong angular dependence, and the discrepancies in both < 1 GeV and > 10 GeV energy spectra of all leptons are more pronounced than at medium inclinations. Neither of these effects are "remedied" by switching to the $E^{-2.7}$ spectrum, as shown in Figures C.4 and C.8. This is not surprising since the horizontal showers develop over longer distances in the atmosphere, and any existing discrepancies between the two codes might accumulate.

Thus, setting aside the very good agreement of the neutrino angular distributions originating from the showers at medium inclinations, we have two main categories of the CORSIKA-MCEQ discrepancies: the tilt of the muon angular distribution ratios at medium inclinations (as in Figure 7.1), and the tilt of both neutrino and muon angular distribution ratios for near-horizontal showers (as in Figure 7.5). The two aspects do not necessarily have the same origin. In the remainder of this chapter, we speculate on several possible sources of the disagreement, including the low-energy/high-energy model transition implementation; the differences in the low-energy model implementation (UrQMD); the geometry of the observation planes used to record the particle information; and the distance-dependent effects such as muon multiple scattering and ionization energy losses.

[3] A. Fedynitch, personal communication, October 2022. Figure C.9 contains the supporting evidence from the unpublished work of A. Fedynitch (reproduced with permission).

7.3 MCEQ-CORSIKA DISCREPANCIES

Low-energy/high-energy model transition

It could be possible that the slightly different implementations of the transition between the low-energy ($\lesssim 80\,\text{GeV}$) and the high-energy ($\gtrsim 80\,\text{GeV}$) hadronic models – in our case UrQMD and EPOS-LHC, respectively – contribute to the MCEq-CORSIKA discrepancies. To test this, we simulated a 50 GeV proton shower in both codes, as in this regime only the low-energy model is active. The results are presented in Figures C.1 and C.5, which show that the characteristic "muon tilt" at all altitudes does not disappear in the pure low-energy regime, and that the $\mathcal{O}(10\%)$ discrepancies in the energy spectra remain. This rules out the low-energy/high-energy model transition as the possible source of disagreement. This is also unlikely to cause the discrepancies observed for the near-horizontal showers, since the $E^{-2.7}$ spectrum at 80° (Figure C.4) is low-energy dominated and exhibits the same issue.

Low-energy model implementation

Another possible source of disagreement could hide in the different implementations/versions of the low-energy model itself. CORSIKA v.77410 uses the older UrQMD-1.3, while we use UrQMD-3.4. To see what kind of an impact the choice of the low-energy hadronic model has on the angular distributions and the spectra of atmospheric leptons, we performed a test in MCEq where the low-energy model was switched to DPMJet-III 19.1. The results of this test are reported in Appendix D.1. We find that the shape of the angular dependence of the DPMJet-III 19.1 / UrQMD ratio resembles that found for CORSIKA / MCEq at the 80° inclination. However, the MCEq-to-MCEq comparisons exhibit this shape at both medium and high inclinations, whereas in CORSIKA-to-MCEq this shape becomes apparent only at 80°. The magnitude of the MCEq-to-MCEq ratio with different hadronic models is also smaller than that of CORSIKA-to-MCEq for both the angular densities and the energy spectra. We therefore conclude that the similarities between the results of the hadronic model impact test in MCEq and the benchmarking of MCEq against CORSIKA are likely a coincidence. A dedicated comparison performed between the different UrQMD versions, or with another low-energy model in CORSIKA, is warranted.

Geometry of the recording plane

In 2D MCEq, all the Hankel modes (and therefore, all the secondary particle angles) are longitudinally evolved according to the same cascade equation (4.22). This approach bakes in an implicit assumption that the secondaries travel the same distance between two subsequent slant depth steps X_t and X_{t+1}, regardless of which angle they make with the shower axis. The distance

$\Delta X = X_{t+1} - X_t$, however, is always computed *along* the shower axis, and the secondaries that deflect from the core by large angles (e.g. 20°) naturally travel longer distances before they reach the next integration step. This implies, in particular, that the scattered hadrons have more matter to interact with and that the muons lose energy over a longer path. The current implementation of the "observation plane" in MCEq is effectively a circle of radius X (centered at the point of first interaction), which does not take into account the increase in the travel path of the deflected secondaries. This is effect is, however, naturally taken into account in CORSIKA, where the observation planes are flat at medium inclinations and reflect the curvature of the Earth at high inclinations. This could at least qualitatively explain the deficit of the muons at large angles in CORSIKA compared to MCEq, i.e., the "muon tilt" from Figures 7.1 and 7.3. However, it does not explain the *excess* of the muons at small angles (i.e., close to the shower axis), where the two geometries are identical.

Muon multiple scattering

We can consider the possibility of muon multiple scattering contributing to the discrepancy between CORSIKA and MCEq, since it is an effect that accumulates with distance as per Equation (6.4) and the agreement between the two codes is noticeably worse for the near-horizontal showers. In our tests, the Gauss approximation (i.e. the zeroth-order Molière theory) is employed in both CORSIKA and MCEq, and we are not aware of any conceptual or quantitative differences between the two implementations. We test the impact of the muon multiple scattering being turned on/off in MCEq in Section 6.1.2. We find that inclusion of multiple scattering does produce the expected shift of the muon distribution compared to the no-scattering case, and the resulting shape of the distribution ratio is similar to that observed in the near-horizontal shower case in Figure 7.5. However, if the muons were scattered to larger angles in CORSIKA than prescribed by the Gauss approximation (e.g. if the full Molière theory is used in practice despite the settings), we would see a similar shape also in Figures 7.1 and 7.3, where instead we observe a tilt in the opposite direction. In addition, the neutrino angular distributions are affected very little by muon multiple scattering, while the CORSIKA/MCEq ratio for neutrinos shows a strong angular dependence at the 80° inclination. Finally, muon multiple scattering by construction does not affect the muon or the neutrino energies (which we have also verified practically), and therefore cannot explain the discrepancies in the energy spectra. Considering these arguments, we do not find any evidence that muon multiple scattering is driving the observed differences between CORSIKA and MCEq.

Muon energy losses

The implementations of the energy losses in CORSIKA and MCEq are supposed to match exactly as they are described by the standard physics of electromagnetic interactions, namely the Bethe-Bloch description of the charged particle passage through matter. However, previous investigations[4] into the 1D MCEq-CORSIKA agreement suggest that the muon energy losses in CORSIKA when measured directly from the muon propagation Monte Carlo are not in a perfect agreement with the Particle Data Group (PDG) reference for the muon $\langle \frac{\mathrm{d}E}{\mathrm{d}X} \rangle$ in dry air [141]. Specifically, at high inclinations, the stopping powers estimated from CORSIKA are smaller than the PDG reference values. Intuitively, this should result in the excess of muons in CORSIKA compared to MCEq, as the latter does reproduce the $\langle \frac{\mathrm{d}E}{\mathrm{d}X} \rangle$ values from PDG. This is not what we observe in our tests, where the energy spectra in CORSIKA are consistently *under*estimated compared to MCEq. Still, we flag the energy loss implementation in CORSIKA as inconsistent with a standard reference and suggest that this is looked at more closely in future studies.

[4] A. Fedynitch, personal communication, October 2022. Figure C.10 contains the supporting evidence from the unpublished work of A. Fedynitch (reproduced with permission).

V

Summary and outlook

Summary

This thesis focused on the evolution of the cosmic ray-induced atmospheric air showers with applications to atmospheric neutrino flux modelling. Atmospheric neutrinos of GeV-scale energies, which originate from the disintegration of mesons and muons in the air showers, provide the main source of signal for neutrino oscillation studies in several modern experiments. The upcoming upgrades or expansions of these experiments will give birth to facilities such as the IceCube-Upgrade, KM3NeT/ORCA, and Hyper-Kamiokande, all of which will be sensitive to neutrino energies of a few GeV and below. This prompted us to focus specifically on the $\mathcal{O}$(GeV) regime when modelling the fluxes of atmospheric neutrinos. A significant portion of this thesis was also dedicated to atmospheric muons, which, besides being every particle physicist's irreducible background, are one of neutrinos' immediate parents and contribute plenty of complex physics to the cascade evolution.

For atmospheric neutrino oscillation studies, the flux of neutrinos prior to oscillations must be modelled in terms of both the energy spectrum and the angular distributions, as the neutrino arrival direction serves as a proxy for travelled distance and thereby couples directly to the oscillation probability. At the $\mathcal{O}$(GeV) scales, the angular distributions of the hadronic cascade secondaries, including neutrinos, become significantly affected by the air shower development geometry. This comprises the effects such as the bending of the charged particle trajectories in the Earth's magnetic field and the deflection of the cascade secondaries from the direction of the primary particle. The main outcome of this thesis is having developed the methodology and a practical software tool to tackle the latter aspect. This tool was dubbed "2D MCEq," which represents a two-dimensional (2D) extension to the existing MCEq (Matrix Cascade Equations) code. We have successfully achieved the goal set out for this software, which was to complement the longitudinal-only evolution of the air showers in 1D MCEq with the angular development.

The 2D MCEq tool is based on a novel numerical method for hadronic cascade evolution, which consists in successive two-dimensional convolutions of the particle angular densities with the pre-generated scattering kernels. We have significantly simplified this problem by reformulating it in the spectral domain, where the continuous angular variable is replaced with a set of discrete frequency modes. To achieve this, we have identified the correct kind of a spectral transform and the convolution theorem applicable to our case, thereby formulating the two-dimensional cascade theory in both the angular

and the frequency spaces. This approach fits naturally into the 1D MCEQ framework, and its complexity scales linearly with the number of frequency modes included into the system of coupled cascade equations.

The 2D MCEQ code includes all important hadronic and leptonic physics for atmospheric neutrino flux modelling – including inelastic interactions of hadrons with the atmospheric nuclei, decays of unstable particles (including production of polarized muons and polarized muon decay), energy losses due to ionization, and muon multiple scattering. We have benchmarked the angular distributions obtained with 2D MCEQ against CORSIKA, which is the reference Monte Carlo code in the air shower modelling domain. Our results show that the neutrino angular distributions in the two codes agree within 1-10% percent at low-to-medium air shower inclinations ($\lesssim 60°$), while up to 20% discrepancies were observed for the near-horizontal showers. Further, we found that the muon angular distributions exhibit a small bias/shift with respect to one another when compared between the two codes at large deflections from the shower axis. While the origin of these discrepancies is not fully understood, we have proposed and eliminated several hypotheses regarding the possible sources of discrepancy. On the MCEQ side, one remaining candidate is the implementation of the "recording plane" geometry, which does not currently reflect the fact that the significantly deflected secondaries travel longer distances towards a given observation level. On the CORSIKA side, a follow-up investigation into the muon energy losses due to ionization is recommended, as they were found to disagree with the standard reference values in an external study.

Given the very high level of agreement with CORSIKA in most of our test cases and a significant computational advantage of the numerical solution over the Monte Carlo approach, 2D MCEQ provides a very appealing alternative for atmospheric neutrino flux calculations. The computational cost of the 2D MCEQ calculations at the current stage is between several CPU-seconds for vertical showers and 1 CPU-minute for the near-horizontal showers, compared to multiple CPU-hours it takes to gather sufficient statistics for inclusive flux calculations via the Monte Carlo simulations. Our tool therefore opens the pathway to fast exploration of the systematic uncertainties on the angular distributions of atmospheric leptons, including those associated with the hadronic interaction models and the cosmic ray primary flux.

Outlook

The future of the 2D MCEq calculations is three-dimensional. Practically, to compute the full-sky angular distributions of atmospheric neutrinos necessary for neutrino oscillation studies, the angular development of the individual air showers available via 2D MCEq will have to be combined with the spherical geometry of the Earth's atmosphere as well as the initial angular distribution of the cosmic ray primaries. This will imply the integration over the cosmic ray showers starting from every location on the sky and propagating towards the Earth in all directions. A complete three-dimensional calculation will additionally have to take into account the geomagnetic cutoff for the cosmic ray primaries (i.e. restricting their arrival directions depending on energy and the observation location) as well as the deflection the hadronic cascade secondaries in the geomagnetic field. The Monte Carlo studies suggest that the geomagnetic effects will have more impact on the low-energy atmospheric neutrino fluxes in the upgoing (Earth-crossing) region compared to the impact of the geometrical (2D) effects in the same portion of the phasespace, which is yet to be verified via a numerical approach.

The final goal of a numerical three-dimensional atmospheric neutrino flux calculation is to fully control all of the inputs to and all of the machinery of the modelling process, such that the impact of individual ingredients or their correlations can be tested on short time scales without any associated statistical uncertainties or "unknown unknowns" typically baked into the large-scale Monte Carlo simulations. The ultimate impact on the neutrino oscillation studies will be in the reduction of the systematic uncertainty associated with the atmospheric flux predictions, which contribute multiple nuisance parameters to the experimental neutrino oscillation measurements. Breaking down this degeneracy will help push these measurements towards improved sensitivities, while simultaneously clearing up the phasespace for the Beyond the Standard Model physics searches with $\mathcal{O}$(GeV) atmospheric neutrinos.

VI

Appendices

APPENDIX A

Mathematical preliminaries

A.1 Transformation matrices

A.1.1 *Transformation rules for vectors*

The matrix applying the rotation of a four-vector by an angle θ about the x axis is given by:

$$R^{x}_{\mu\nu}(\theta) = \begin{pmatrix} 1 & 0 & 0 & 0 \\ 0 & 1 & 0 & 0 \\ 0 & 0 & \cos\theta & -\sin\theta \\ 0 & 0 & \sin\theta & \cos\theta \end{pmatrix} \tag{A.1}$$

The matrix describing the boost of a four-vector into the frame moving with velocity v along the z axis, such that its Lorentz factors are $\beta(v)$ and $\gamma(v)$, is:

$$\Lambda^{z}_{\mu\nu}(v) = \begin{pmatrix} \gamma(v) & 0 & 0 & -\gamma(v)\beta(v) \\ 0 & 1 & 0 & 0 \\ 0 & 0 & 1 & 0 \\ -\gamma(v)\beta(v) & 0 & 0 & \gamma(v) \end{pmatrix} \tag{A.2}$$

A.1.2 *Transformation rules for spinors*

The matrix describing the boost of the left-chiral Weyl spinor ψ_{L} along the z axis reads:

$$\Lambda^{\mathrm{L},z}_{ab}(\phi) = \begin{pmatrix} e^{\frac{\phi}{2}} & 0 \\ 0 & e^{-\frac{\phi}{2}} \end{pmatrix}, \tag{A.3}$$

where $\phi = \tanh^{-1}(\beta(\mathrm{v})$ is the rapidity of the boost and the subscripts (a, b) refer to the two components of the spinor. Similarly, for the right-chiral spinor ψ_{R}:

$$\Lambda^{\mathrm{R},z}_{ab}(\phi) = \begin{pmatrix} e^{-\frac{\phi}{2}} & 0 \\ 0 & e^{\frac{\phi}{2}} \end{pmatrix} \tag{A.4}$$

The rotation matrices (e.g. by an angle θ about the x axis) are identical for the left-chiral and the right-chiral spinors:

$$R^{\mathrm{L},x}_{ab}(\theta) = R^{\mathrm{R},x}_{ab}(\theta) = \begin{pmatrix} \cos\frac{\theta}{2} & i\sin\frac{\theta}{2} \\ i\sin\frac{\theta}{2} & \cos\frac{\theta}{2} \end{pmatrix} \tag{A.5}$$

APPENDIX B

Hankel transform implementation

As discussed in Section 5.2, we compute the Hankel transforms of the angular densities of the secondary particles coming out of the event generators numerically via the "delta function summation" method. The method consists in adding up the Hankel transforms of the Dirac delta functions $\underline{\delta}$ corresponding to the generated angles θ one-by-one, thereby providing a *kernelless* density estimate. The reliability of such an estimate depends on the number of delta functions n_δ being summed. To prove this, we define a toy function $\phi(\theta)$,

$$\phi(\theta) = \mathcal{N}\theta^b \cdot e^{-a\theta} \tag{B.1}$$

over the domain $\theta \in [0, \pi/2]$, which closely resembles the shape of the angular densities of the actual secondaries obtained in the solutions to the 2D MCEq equations (see e.g. Figure 6.3 and Section 7.2). The normalization factor $\mathcal{N}$ in Equation (B.1) ensures that $\int_0^{\pi/2} \phi(\theta)\mathrm{d}\theta = 1$. We set the true parameters to $\{a = 20; b = 1\}$ and draw θ_i samples ($i = 1..n_\delta$) from the $\phi(\theta)$ distribution. We then compute the Hankel transforms of the obtained θ_i distributions via

$$\tilde{\phi}(\kappa_j) = \frac{1}{n_\delta}\sum_{i=1}^{n_\delta} \mathcal{H}\left[\frac{1}{\theta_i}\underline{\delta}(\theta - \theta_i)\right](\kappa_j) = \frac{1}{n_\delta}\sum_{i=1}^{n_\delta} J_0(\kappa_j\theta_i) \tag{B.2}$$

for the discrete modes κ_j. Finally, we apply the inverse Hankel transform to $\tilde{\phi}(\kappa_j)$, which requires a continuous approximation $\tilde{\phi}(\kappa_j) \to \tilde{\phi}(\kappa)$. In Figures B.1 and B.2, we provide the results of the $\phi(\theta)$ reconstruction using different values of n_δ, which correspond to the spline-based and the Student t-based continuous approximations of $\tilde{\phi}(\kappa_j)$ as described in Section 6.2. We see that the accuracy of the spline-based continuous approximation to $\tilde{\phi}(\kappa)$ depends heavily on the number of the Hankel-transformed delta functions $\underline{\delta}$ entering Equation (B.2), i.e., the number of samples drawn from the distribution. This dependence is much more mild for the Student t-based reconstruction, which provides a very good estimate of the true density even for n_δ as low as 10^2. However, as shown in Figure B.3, the accuracy of the spline-based reconstruction near the peak of the $\phi(\theta)$ distribution is better than that of the Student t-based reconstruction for the largest tested n_δ. This is why we select the spline approximation to $\tilde{\phi}(\kappa)$ when converting the 2D MCEq Hankel modes to the angular densities of the cascade secondaries.

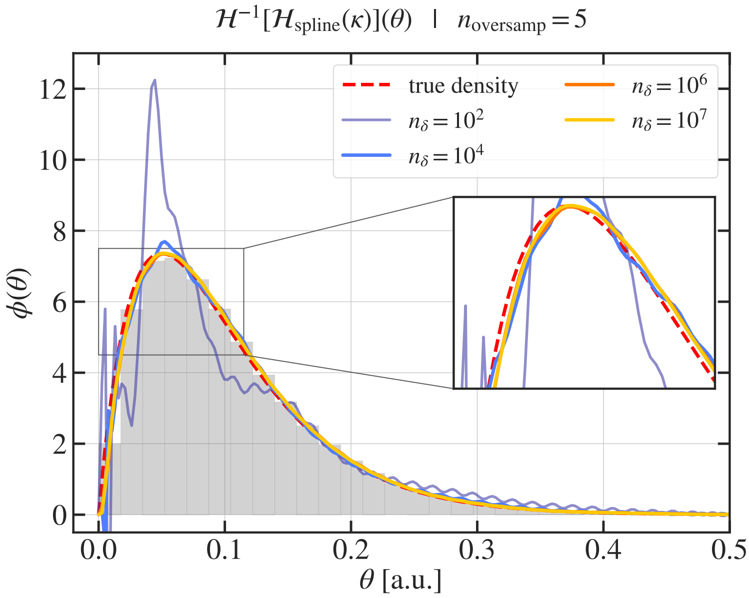

Figure B.1 – The accuracy of the probability density reconstruction for the toy distribution (B.1) via the delta function summation using different numbers of deltas (n_δ). Here, the continuous approximation to the numerical Hankel transform is found via the cubic spline prior to evaluating the integral in Equation (6.6).

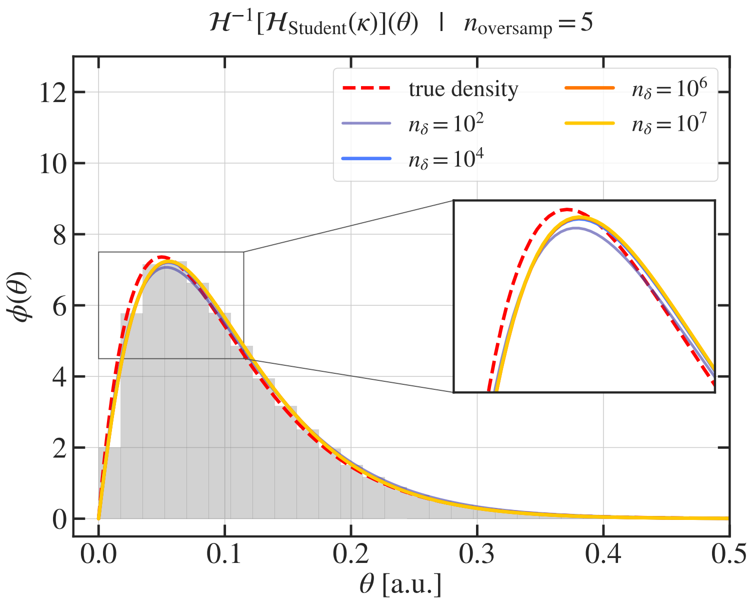

Figure B.2 – Same as Figure B.1, but with the continuous approximation to the numerical Hankel transform found via the Student's t fit (see Equation (6.7)).

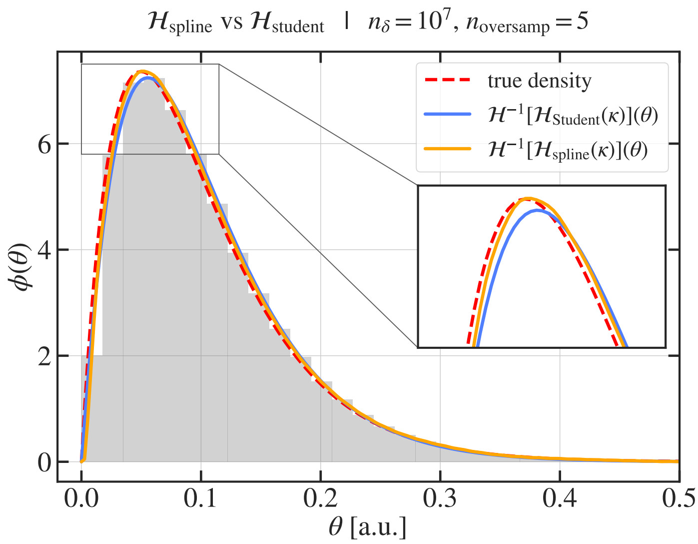

FIGURE B.3 – The reconstruction of the probability density (B.1) via the inverse Hankel transform of the Student's t- and the spline-based continuous extensions of (B.2).

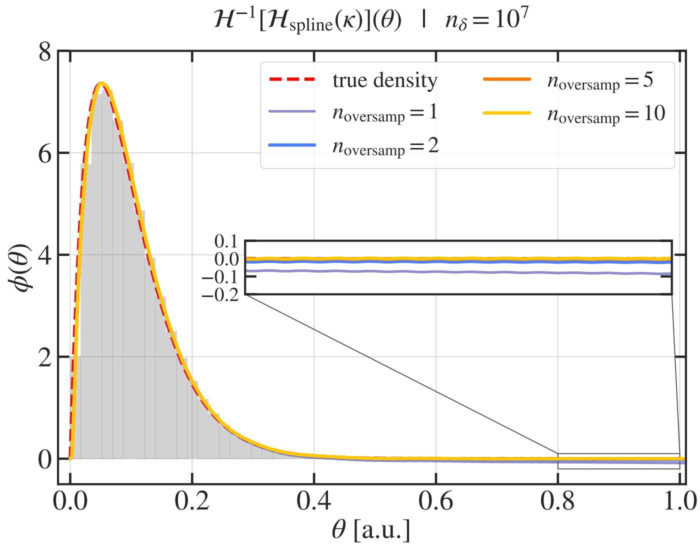

FIGURE B.4 – The effect of the oversampling resolution on the reconstruction of (B.1).

Finally, we note that our tests in Figures B.1 to B.3 use the oversampled κ grid for the evaluation of $\mathcal{H}^{-1}$ integral. This grid is linearly spaced between $\kappa_{\text{min}} = 0$ and $\kappa_{\text{max}} = 2000$, and the total number of grid points is $n_{\text{oversamp}} \cdot \kappa_{\text{max}} + 1$. Testing $n_{\text{oversamp}} = \{1, 2, 5, 10\}$ in Figure B.4, we find that $n_{\text{oversamp}} \leq 2$ results in an undesirable artefact around the reconstructed distribution tails, namely the slope towards $\phi(\theta) < 0$. Since probability density functions can never take negative values, we choose $n_{\text{oversamp}} = 5$ to remove this artefact.

APPENDIX C

MCEq-CORSIKA COMPARISONS (CONTINUED)

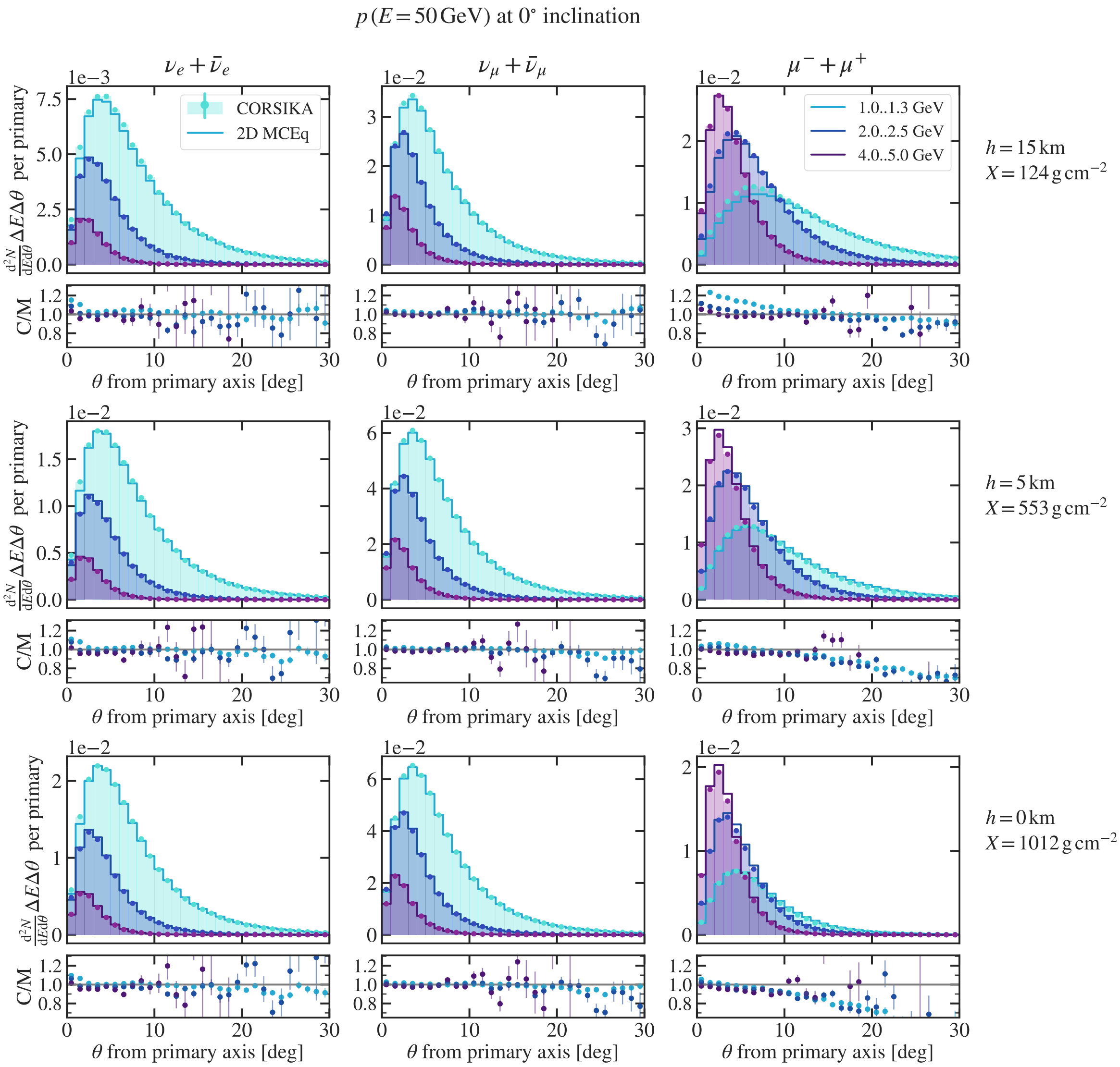

FIGURE C.1 – Angular distributions of atmospheric leptons in a proton-induced air shower ($E_0 = 50\,\mathrm{GeV}$, $\theta_0 = 0°$), as computed in 2D MCEq (solid line) and simulated in CORSIKA (filled histogram). "C/M" stands for the CORSIKA/MCEq ratio.

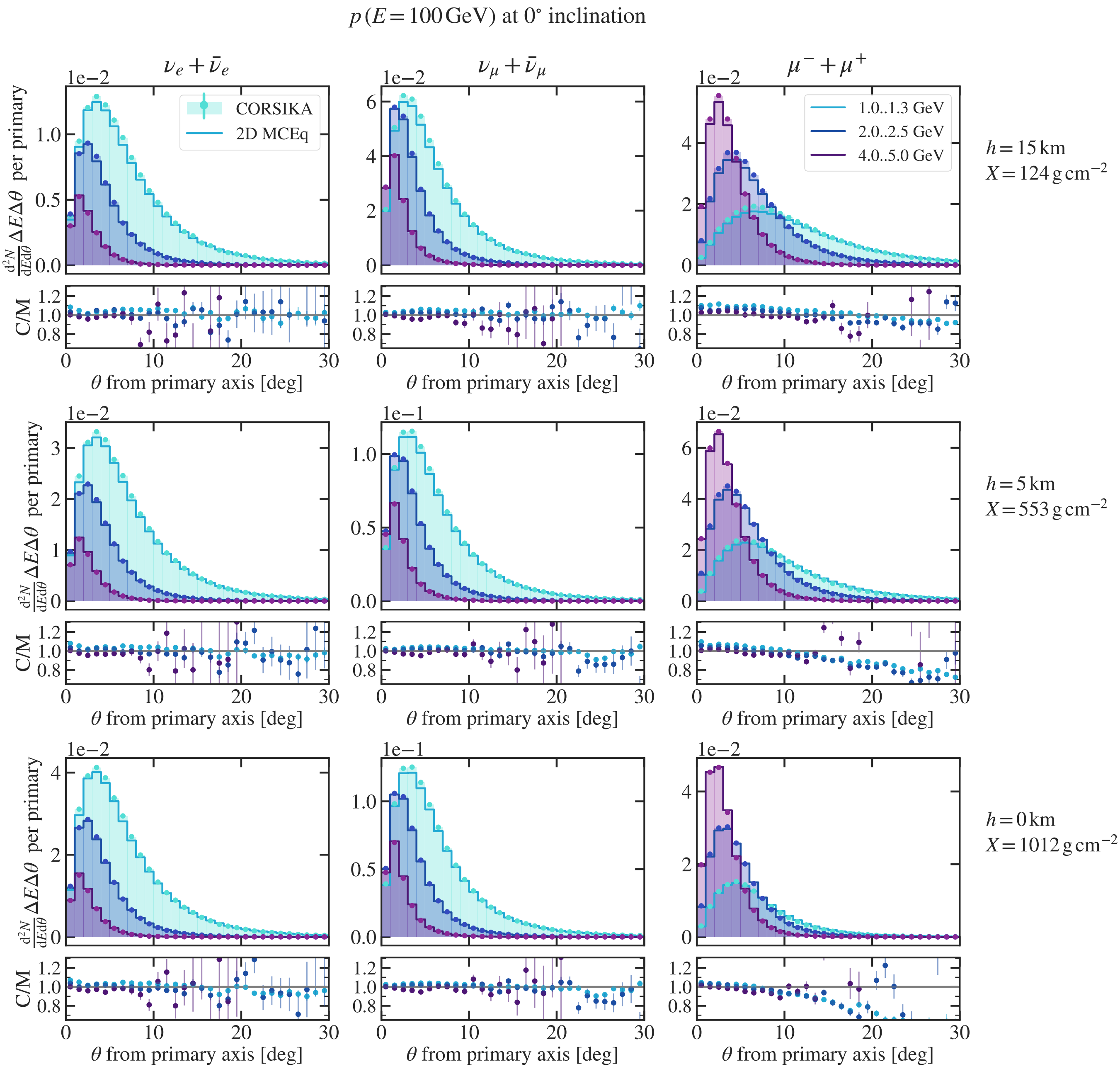

FIGURE C.2 – Same as Figure C.1, but for the primary proton energy $E_0 = 100\,\text{GeV}$.

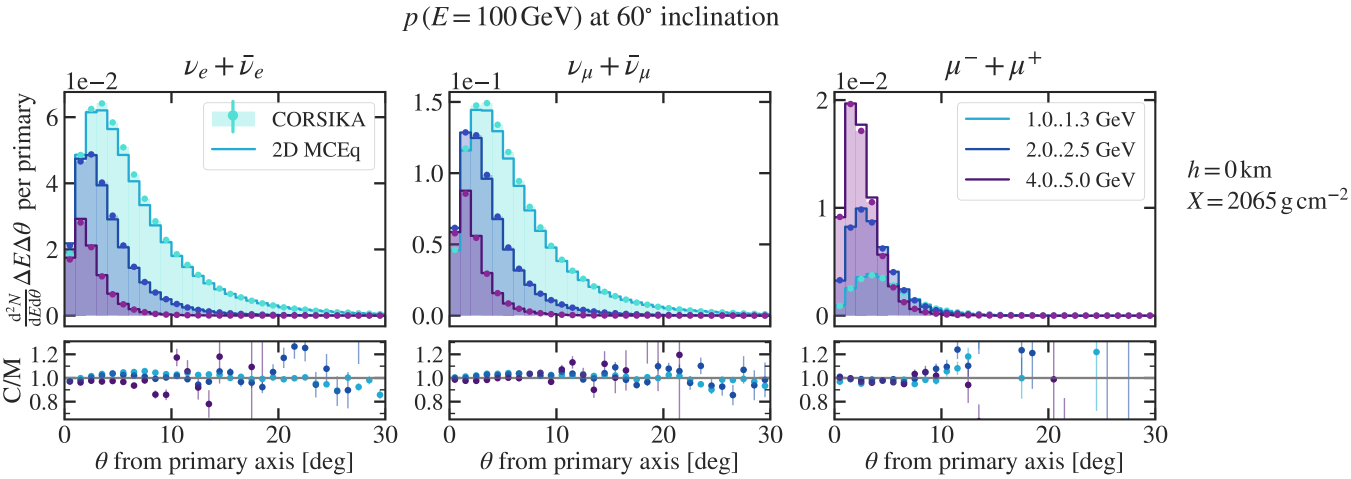

Figure C.3 – Same as Figure C.1, but for the primary proton energy $E_0 = 100\,\mathrm{GeV}$ and inclination $\theta_0 = 60°$.

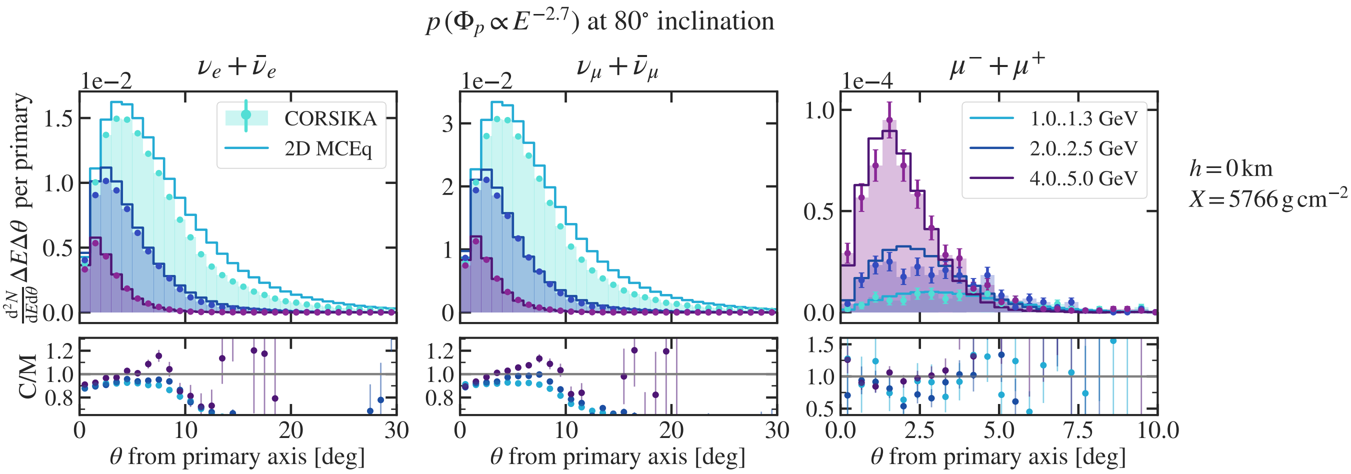

Figure C.4 – Same as Figure C.1, but for the primary proton energies sampled from the $E^{-2.7}$ spectrum and inclination $\theta_0 = 80°$.

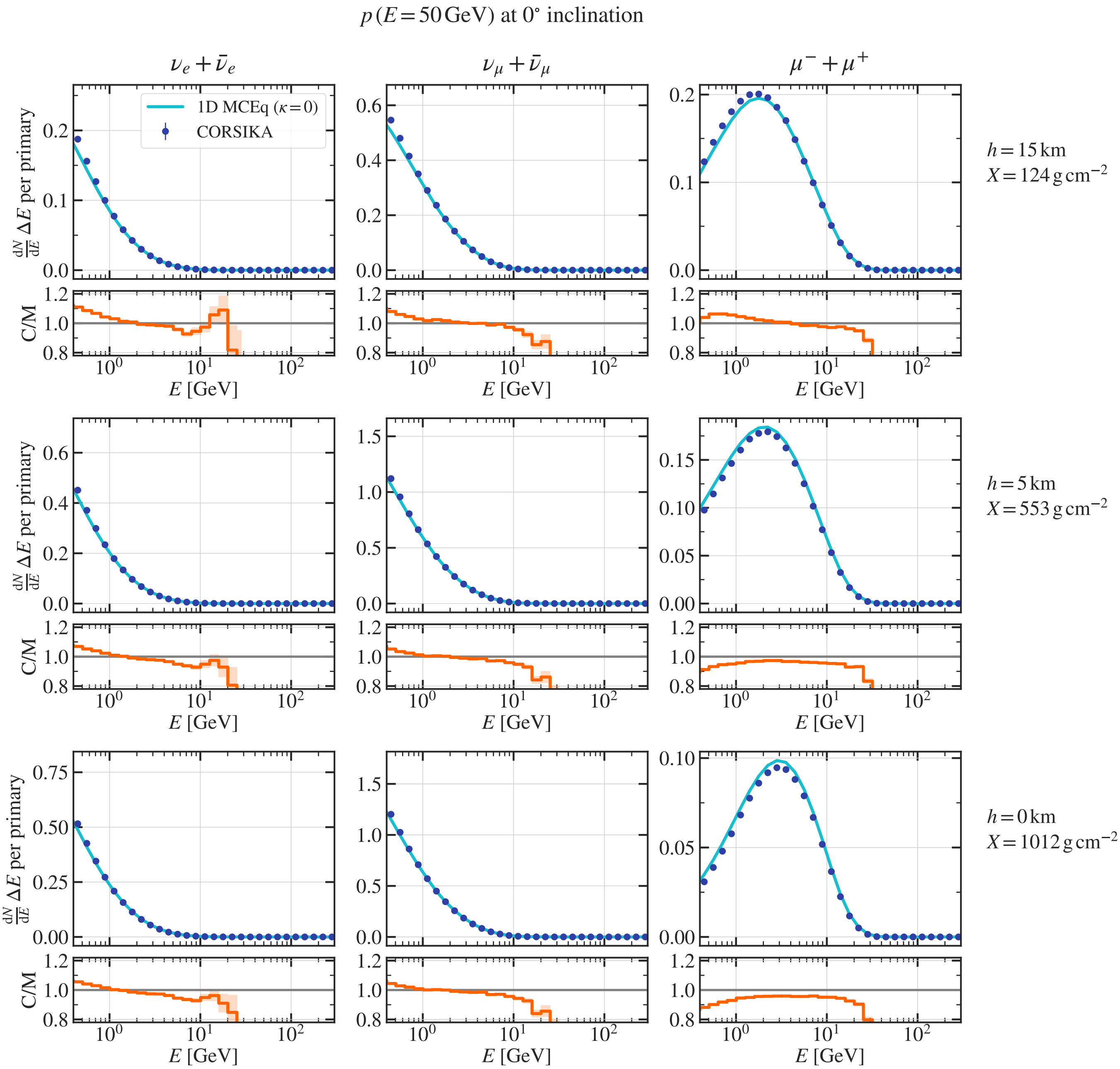

Figure C.5 – Energy spectra of atmospheric leptons in a proton-induced air shower ($E_0 = 50\,\mathrm{GeV}$, $\theta_0 = 0°$), as computed in 1D MCEq (solid line) and simulated in CORSIKA (filled markers). Here, "1D MCEq" corresponds to the $\kappa = 0$ slice of the 2D MCEq solution. "C/M" stands for the CORSIKA/MCEq ratio.

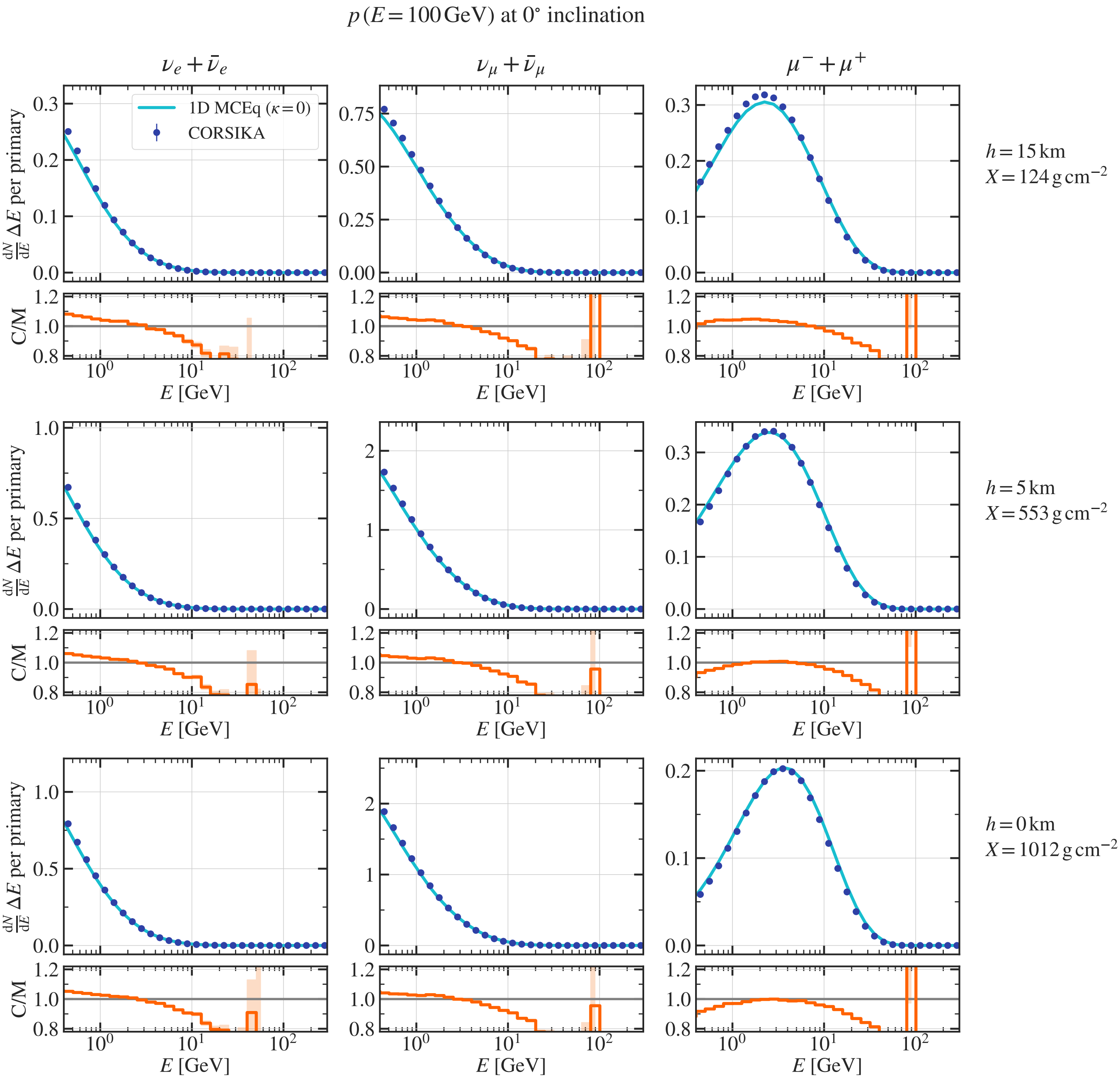

FIGURE C.6 – Same as Figure C.5, but for the primary proton energy $E_0 = 100\,\mathrm{GeV}$.

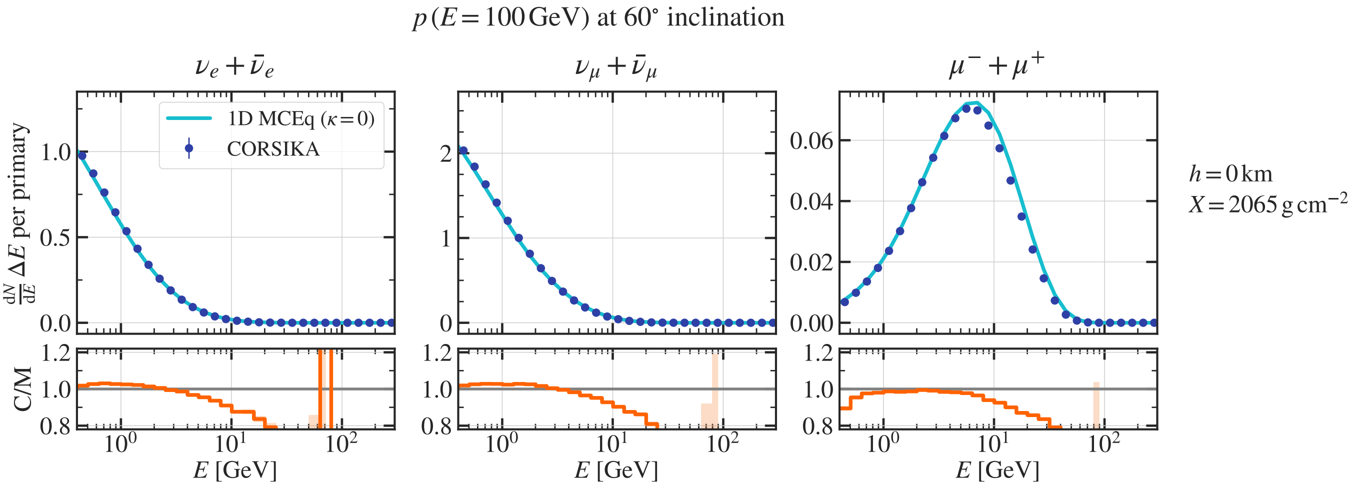

Figure C.7 – Same as Figure C.5, but for the primary proton energy $E_0 = 100\,\mathrm{GeV}$ and inclination $\theta_0 = 60°$.

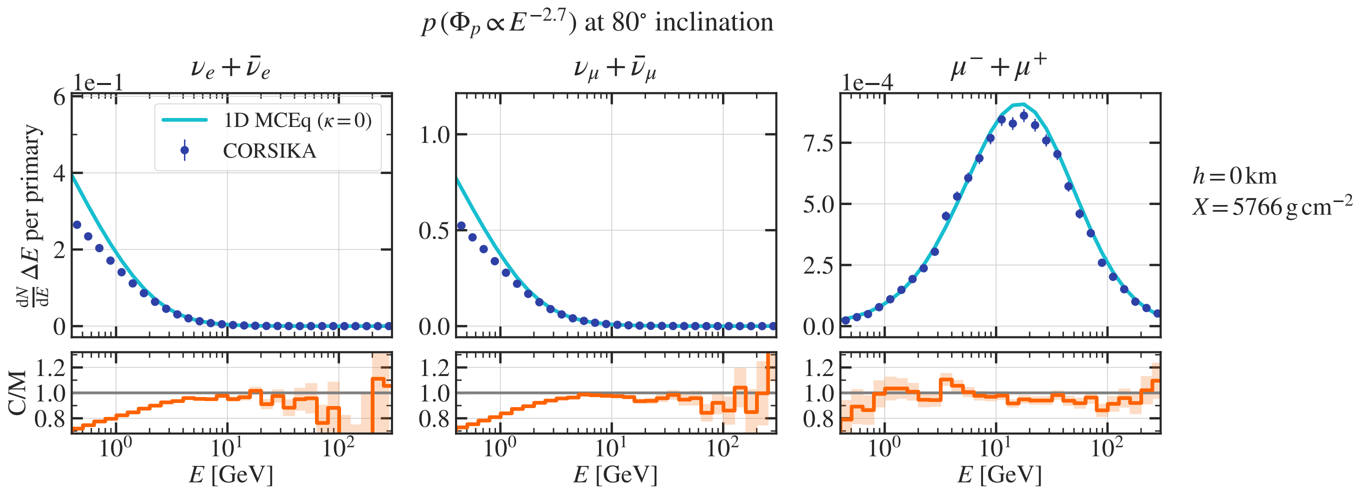

Figure C.8 – Same as Figure C.5, but for the primary proton energies sampled from the $E^{-2.7}$ spectrum and inclination $\theta_0 = 80°$.

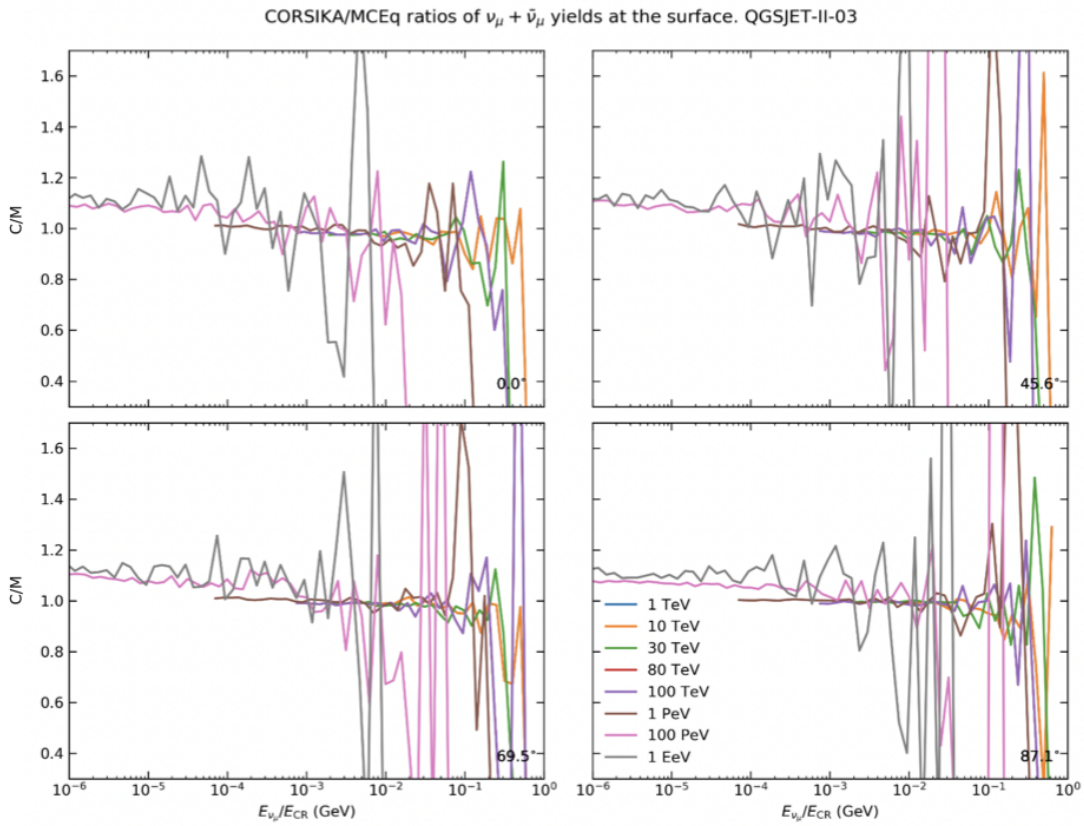

Figure C.9 – CORSIKA/MCEq ratios of the $\nu_\mu + \bar{\nu}_\mu$ yields in the proton-induced showers at different energies and inclinations. The x axis shows the ratio of the secondary neutrino energy to the primary proton energy. The plot is reproduced from an unpublished study on 1D MCEq-CORSIKA comparisons with permission from the author (A. Fedynitch).

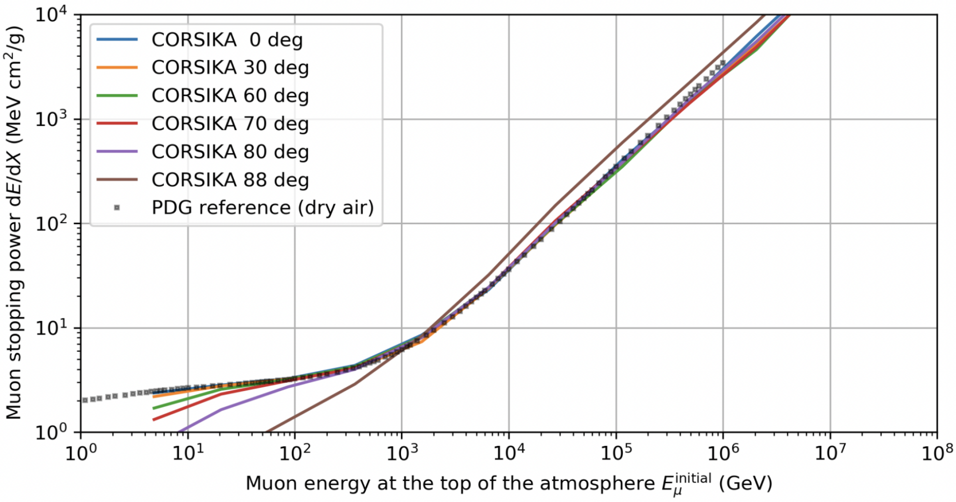

Figure C.10 – Comparison of the muon energy losses (ionization + radiative) from the muon propagation simulations in CORSIKA and the standard Particle Data Group reference for muon energy losses in dry air [141]. The plot is reproduced from an unpublished study on 1D MCEq-CORSIKA comparisons with permission from the author (A. Fedynitch).

APPENDIX D

MCEQ PHYSICS IMPACT

D.1 THE IMPACT OF THE HADRONIC INTERACTION MODEL CHOICE

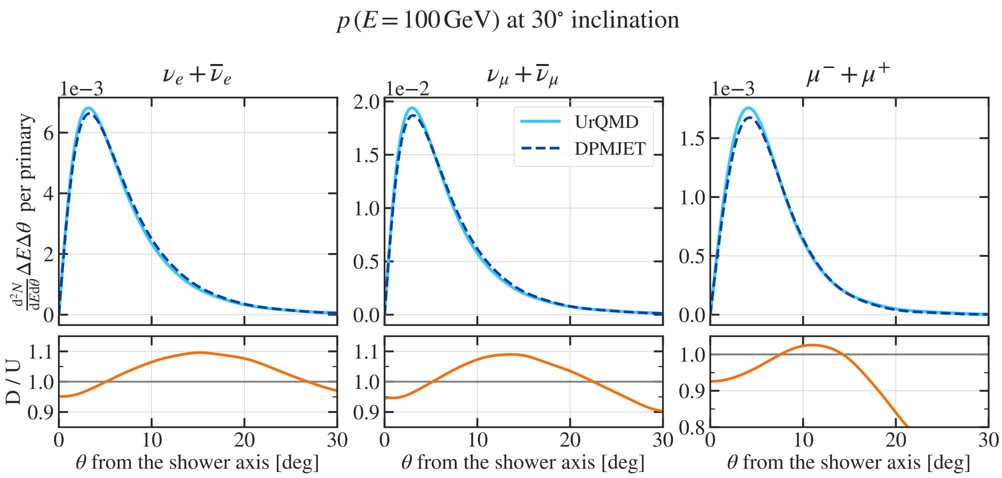

FIGURE D.1 – Comparison of the 2D MCEQ angular distributions of 1.0..1.3 GeV atmospheric leptons in a proton-induced shower ($E_0 = 100\,\text{GeV}$, $\theta_0 = 30°$) evolved with two different low-energy hadronic interaction models: URQMD ("U") and DPMJET-III 19.1 ("D"). The solutions are shown at the Earth's surface; $\Delta\theta = 0.15°$.

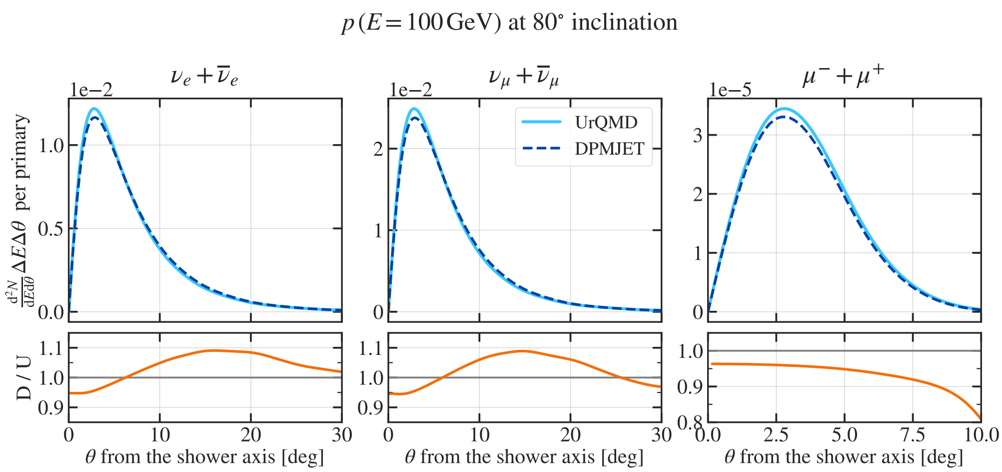

FIGURE D.2 – Same as Figure D.1, but for the 80° inclination.

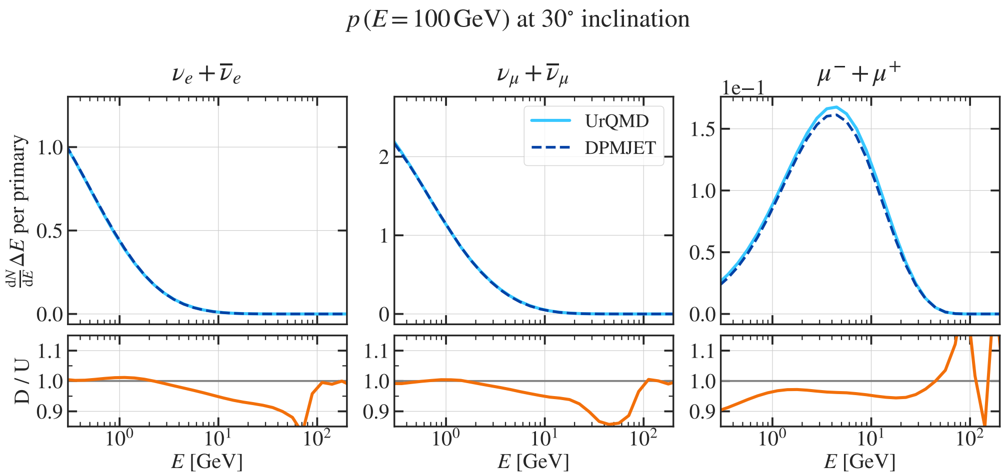

Figure D.3 – Comparison of the 1D MCEq energy spectra of atmospheric leptons in a proton-induced shower ($E_0 = 100\,\mathrm{GeV}$, $\theta_0 = 30°$) evolved with two different low-energy hadronic interaction models: UrQMD ("U") and DPMJet-III 19.1 ("D"). The solutions are shown at the Earth's surface.

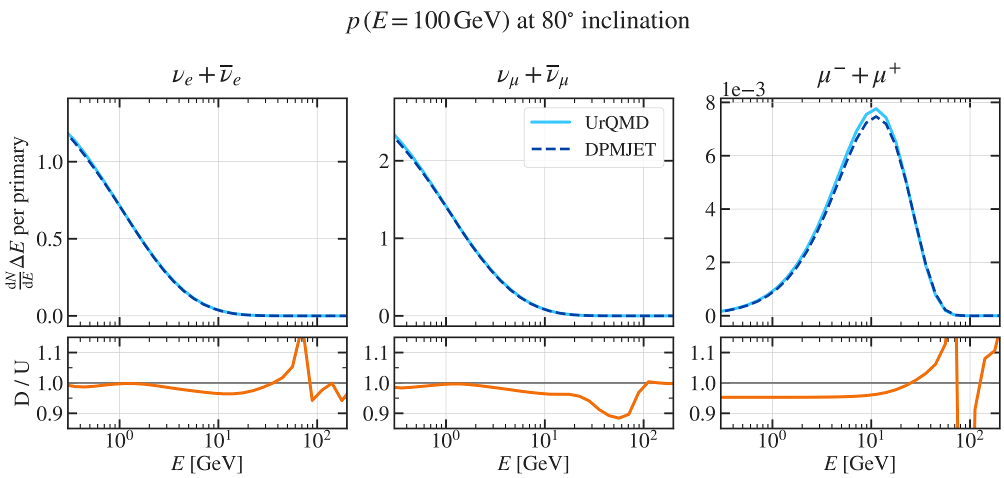

Figure D.4 – Same as Figure D.3, but for the 80° inclination.

D.2 THE IMPACT OF MUON PHYSICS

D.2.1 *Muon multiple scattering*

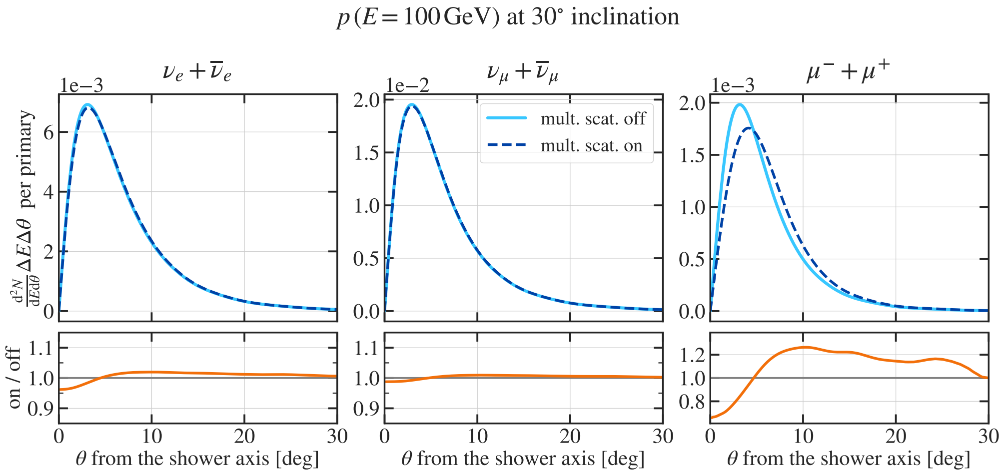

FIGURE D.5 – Comparison of the 2D MCEQ angular distributions of 1.0..1.3 GeV atmospheric leptons in a proton-induced shower ($E_0 = 100\,\mathrm{GeV}$, $\theta_0 = 30°$) evolved with/without muon multiple scattering ("on"/"off"). The solutions are shown at the Earth's surface; $\Delta\theta = 0.15°$.

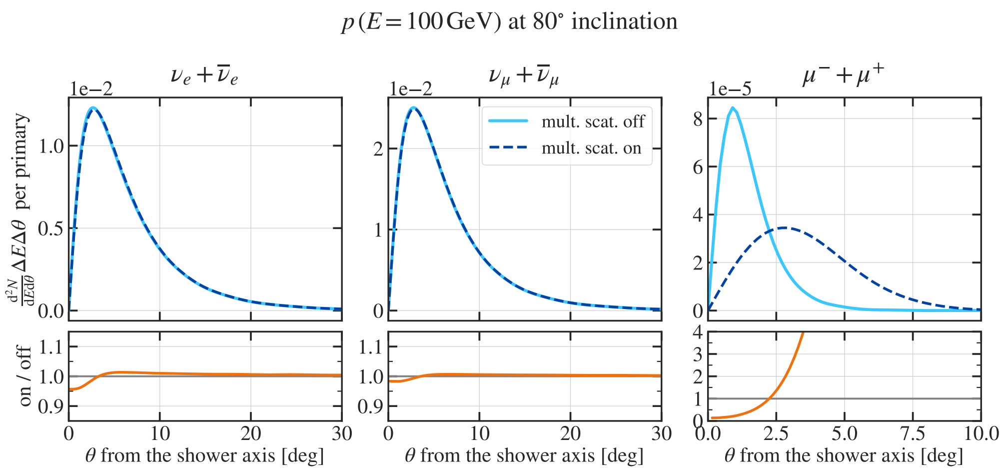

FIGURE D.6 – Same as Figure D.5, but for the 80° inclination.

D.2.2 *Muon polarization*

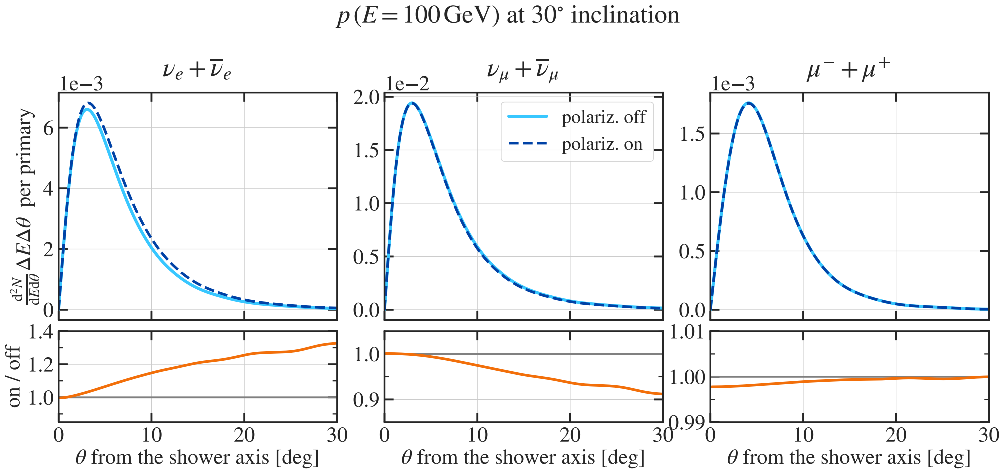

Figure D.7 – Comparison of the 2D MCEq angular distributions of 1.0..1.3 GeV atmospheric leptons in a proton-induced shower (E_0 = 100 GeV, θ_0 = 30°) evolved with/without muon polarization ("on"/"off"). The solutions are shown at the Earth's surface; $\Delta\theta$ = 0.15°.

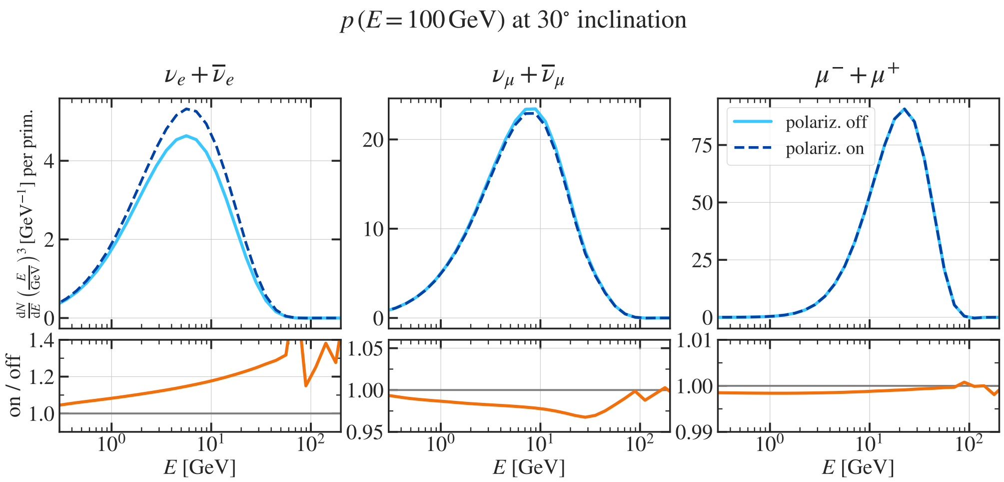

Figure D.8 – Comparison of the 1D MCEq energy spectra of atmospheric leptons in a proton-induced shower (E_0 = 100 GeV, θ_0 = 30°) evolved with/without muon polarization ("on"/"off"). The solutions are shown at the Earth's surface.

PROCEEDINGS OF SCIENCE
ONLINE ICRC 2021 THE ASTROPARTICLE PHYSICS CONFERENCE Berlin | Germany
37th International Cosmic Ray Conference 12–23 July 2021

A Numerical Approach to Angular Distributions in Hadronic Cascades

Tetiana Kozynets,[a,*] **Anatoli Fedynitch**[b] **and D. Jason Koskinen**[a]

[a] *Niels Bohr Institute, University of Copenhagen, Blegdamsvej 17, 2100 Copenhagen Ø, Denmark*

[b] *Institute for Cosmic Ray Research, University of Tokyo, 5-1-5 Kashiwa-no-ha, Kashiwa, Chiba 277-8582, Japan*

E-mail: tetiana.kozynets@nbi.ku.dk, afedyni@icrr.u-tokyo.ac.jp, koskinen@nbi.ku.dk

Hadronic interactions of highly energetic projectiles in matter induce rich cascades of daughter particles, an example being atmospheric neutrinos produced in cosmic ray air showers. Fully analytical modelling of such cascades, due to the amount and the complexity of the coupled processes involved, is infeasible, while Monte Carlo simulations remain computationally expensive. These complications are mitigated in the numerical Matrix Cascade Equations (MCEQ) code, which reaches Monte Carlo-like precision at extremely low computational costs. Previously, the MCEQ framework has included longitudinal-only development of the hadronic cascades.

To accurately model secondaries at MeV-GeV energies in particle cascades, we extend the one-dimensional cascade equation solver to 2D by including angular development. The distributions are computed via the spectral methods and compared to those produced with the Monte Carlo cascade codes. The potential applications of this study include fast numerical calculations of particle fluxes in air showers and atmospheric lepton flux calculations, which will benefit simulation chains of the cosmic ray and neutrino experiments.

37th International Cosmic Ray Conference (ICRC 2021)
July 12th – 23rd, 2021
Online – Berlin, Germany

*Presenter

© Copyright owned by the author(s) under the terms of the Creative Commons Attribution-NonCommercial-NoDerivatives 4.0 International License (CC BY-NC-ND 4.0).

PoS(ICRC2021)1209

1. Introduction

Hadronic interactions of energetic projectiles in matter produce a wealth of daughter particles, whose subsequent reinteractions and/or decays result in a hadronic cascade. Such processes are central to the evolution of the cosmic ray air showers and form a natural environment to probe fundamental particle physics across a wide range of energies, from MeV to PeV. A particularly important byproduct of the atmospheric hadronic cascades are neutrinos, which, at the energies of $O(10\,\mathrm{GeV})$ and below, provide the leading signal for neutrino oscillation measurements. The angular distributions of neutrinos at these energies depend on the complete three-dimensional treatment of atmospheric neutrino production [1–5]. This presents one of the many physics cases where including both longitudinal and lateral components into hadronic cascade modelling is necessary.

The modern hadronic cascade codes are predominantly Monte Carlo based. These include e.g. FLUKA [6], GEANT4 [7], and PHITS [8] general purpose simulation packages for arbitrary materials, as well as dedicated atmospheric air shower codes such as CORSIKA [9] and AIRES [10]. A sophisticated treatment of the individual particle interactions in such codes comes with high computational costs. The complexity of the Monte Carlo solvers also makes immediate and comprehensive benchmarking of the different codes against each other rather difficult. These limitations make the existence of a precise, fast, and customizable hadronic cascade code particularly appealing.

A natural mathematical formulation of the cascade development problem is through the coupled differential equations for particle propagation, interaction, and decay. A current state-of-the-art software employing such an approach is the Matrix Cascade Equations (MCEQ) code[1], which formulates the transport equations in the matrix form [11–13]. Up until now, MCEQ has provided only longitudinal cascade development. To extend its applications to the low-energy atmospheric neutrino flux modelling as well as air-shower and radiation dose calculations, we focus on including the angular component into the MCEQ framework. This study demonstrates that multi-dimensional hadronic cascade development can be well modeled as a sequence of angular convolutions.

2. Overview of the Matrix Cascade Equations and the MCEq Code

The longitudinal evolution of a hadronic cascade is governed by the 1D multi-species Boltzmann transport equation. Discretizing this equation in energy allows one to put the probabilities of interaction and decay processes in a matrix form and to solve for the particle fluxes $\mathbf{\Phi}$ on a fixed energy grid. Explicitly, for a cascade particle h, the differential spectrum $\Phi^h_{E_i} \equiv \frac{\mathrm{d}N^h_{E_i}}{\mathrm{d}E}$ evolves as a function of the traversed slant depth X according to

$$\frac{\mathrm{d}\Phi^h_{E_i}(X)}{\mathrm{d}X} = -\frac{\Phi^h_{E_i}(X)}{\lambda^h_{\mathrm{int},E_i}} - \frac{\Phi^h_{E_i}(X)}{\lambda^h_{\mathrm{dec},E_i}(X)} \tag{1a}$$

$$+ \sum_{E_k \geq E_i} \sum_l \frac{c_{l(E_k)\to h(E_i)}}{\lambda^l_{\mathrm{int},E_k}} \Phi^l_{E_k}(X) + \sum_{E_k \geq E_i} \sum_l \frac{d_{l(E_k)\to h(E_i)}}{\lambda^l_{\mathrm{dec},E_k}(X)} \Phi^l_{E_k}(X). \tag{1b}$$

The particle h in the energy bin E_i can undergo inelastic collisions in the target medium and decay into other species following (1a), with the corresponding probabilities defined by the interaction

[1] https://github.com/afedynitch/MCEq

PoS(ICRC2021)1209

length $\lambda^h_{\mathrm{int},E_i}$ and the decay length $\lambda^h_{\mathrm{dec},E_i}$. The same particle can also be produced by other cascade species l with energies $E_k \geq E_i$ through interactions or decays as per (1b). The probabilities of producing the secondary h are represented as the yield coefficients $c_{l(E_k)\to h(E_i)}$ and $d_{l(E_k)\to h(E_i)}$. The equations for the different particle species are coupled and can be solved in a matrix form by the forward propagation of Eq. (1) in X, which is further detailed in [11, 13].

In MCEQ, the coefficients $c_{l(E_k)\to h(E_i)}$ and $d_{l(E_k)\to h(E_i)}$ are derived directly from event generators by histogramming the yields of h from an l-target collision or a decay of l as a function of E_i/E_k. For l-target collisions, interaction models such as EPOS-LHC [14], URQMD [15], and DPMJET-III [16] can be employed, while PYTHIA 8 [17] is used to handle the kinematics of decays.

3. Angular Cascade Development in the MCEq Framework: "2D MCEq"

3.1 Evolving the Cascades via Sequential Angular Convolutions

In Section 2, the spectra $\Phi^h_{E_i}$ entering the cascade equation are integrated over the angle θ that the secondaries make with the primary axis. We now wish to evolve the spectra as a function of θ in addition to the slant depth X. In what follows, we will consider only forward-going particles, i.e. those with $0 \leq \theta \leq \pi/2$, and assume azimuthal symmetry *wrt.* the initial particle direction. Defining $\phi^h_{E_i}(X,\theta) \equiv \frac{\mathrm{d}N^h_{E_i}(X,\theta)}{\mathrm{d}E\mathrm{d}\theta}$, we can expand Eq. (1) as

$$\begin{aligned}\frac{\mathrm{d}\phi^h_{E_i}(X,\theta)}{\mathrm{d}X} &= -\frac{\phi^h_{E_i}(X,\theta)}{\lambda^h_{\mathrm{int},E_i}} - \frac{\phi^h_{E_i}(X,\theta)}{\lambda^h_{\mathrm{dec},E_i}(X)} \\ &+ \sum_{E_k\geq E_i}\sum_{l}\int_0^{\pi/2}\frac{\varsigma_{l(E_k,\theta')\to h(E_i,\theta)}}{\lambda^l_{\mathrm{int},E_k}}\phi^l_{E_k}(X,\theta')\mathrm{d}\theta' \\ &+ \sum_{E_k\geq E_i}\sum_{l}\int_0^{\pi/2}\frac{\delta_{l(E_k,\theta')\to h(E_i,\theta)}}{\lambda^l_{\mathrm{dec},E_k}(X)}\phi^l_{E_k}(X,\theta')\mathrm{d}\theta'.\end{aligned} \tag{2}$$

The new double-differential yield coefficients are normalized through integration over θ to match the particle yield coefficients of 1D MCEQ

$$c_{l(E_k)\to h(E_i)} \equiv \int_0^{\pi/2}\varsigma_{l(E_k,\theta')\to h(E_i,\theta)}\mathrm{d}(\theta-\theta') = \int_0^{\pi/2}\varsigma_{l(E_k,0)\to h(E_i,\theta)}\mathrm{d}\theta. \tag{3}$$

As we restrict ourselves to $0 \leq \theta \leq \pi/2$ and set particle fluxes outside this domain to 0, the integration bounds may well be extended to the periodic $-\pi..\pi$ interval. This lets us formulate the collision integral in terms of the circular convolution operator $\circledast$:

$$\int_0^{\pi/2}\varsigma_{l(E_k,\theta')\to h(E_i,\theta)}\phi^l_{E_k}(X,\theta')\mathrm{d}\theta' \equiv [\varsigma_{l(E_k)\to h(E_i)} \circledast \phi^l_{E_k}](\theta) \tag{4}$$

The inclusion of the angular variable then becomes a straightforward extension of the 1D MCEQ functionality. As before, one proceeds by simulating the $l(E_k)$-target collision events or the decays of $l(E_k)$ in a Monte Carlo event generator. An extra step in the 2D case is to keep track of the angular distribution $\varsigma_{l(E_k)\to h(E_i)}(\theta)$ when histogramming the yields of the particle h in the $l(E_k) \to h(E_i)$

PoS(ICRC2021)1209

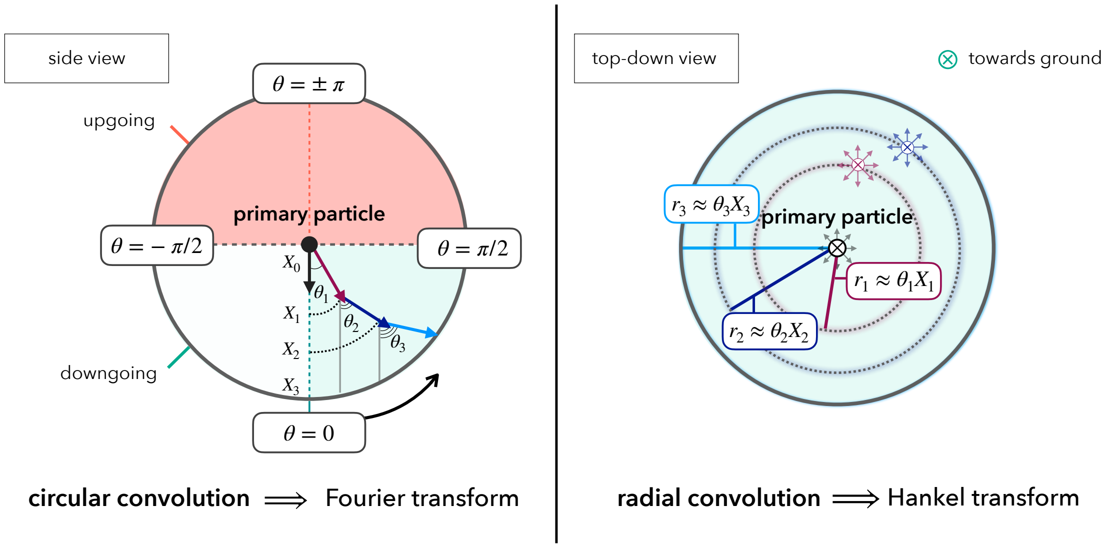

Figure 1: Two different views on the evolution of a hadronic cascade in the longitudinal (X) and angular (θ) dimensions. In both cases, the primary particle (e.g. a cosmic ray proton) is injected at $\theta = 0$ and $X_0 = 0$. At a depth X_i, the secondaries make an angle θ_i with the primary axis. On the left panel, θ is treated as a quasi-periodic circular variable, which we restrict to the forward ($|\theta| \leq \pi/2$) region. On the right panel, θ_i is interpreted as the radius of the circle containing the secondaries at X_i. This leads to the appearance of either circular or radial convolution operators in Eq. (4), which correspondingly translate to either Fourier or Hankel transforms in the spectral formulation of the problem (see Section 3.2).

process. The probability density of the outgoing secondary angle with respect to the primary direction then acts as a convolution kernel for Eq. (4).

Note that if we instead defined $\phi^h_{E_i}(X,\theta) \equiv \frac{\mathrm{d}N^h_{E_i}(X,\theta)}{\mathrm{d}E\,\sin\theta\,\mathrm{d}\theta} \approx \frac{\mathrm{d}N^h_{E_i}(X,\theta)}{\mathrm{d}E\,\theta\,\mathrm{d}\theta}$ for small θ, the linear integration in θ in Eqs. (2) to (4) would be replaced by the radial one: $\mathrm{d}\theta \to \theta\mathrm{d}\theta$, and the "1D" circular convolution operator ($\circledast$) would change to the "2D" radial convolution operator ($**$). These two different approaches to the angular evolution of particle cascades are illustrated in Fig. 1.

3.2 The Spectral Convolution Method

Depending on the energies involved in a hadronic cascade, the angle θ that a daughter particle makes with its immediate parent may vary significantly and span several orders of magnitude. Thus, if the convolutions were performed on a uniform θ grid, the latter would have to be discretized very finely to capture the processes at all angular scales, presenting a major computational challenge. A convenient way to get around this complication is to bring the 2D cascade equation to the spectral domain, where the particle fluxes are given as a function of frequency f. Specifically, in case of the circular convolutions, one can Fourier-transform both sides of Eq. (2), so that $\tilde{\phi}^h_{E_i}(X,f) \equiv \mathcal{F}[\phi^h_{E_i}(X,\theta)](f)$ and $\tilde{\varsigma}_{l(E_k)\to h(E_i)}(f) \equiv \mathcal{F}[\varsigma_{l(E_k)\to h(E_i)}(\theta)](f)$. Then, via the convolution theorem, the circular convolution $\circledast$ transforms into simple multiplication:

PoS(ICRC2021)1209

$$\frac{\mathrm{d}\tilde{\phi}^h_{E_i}(X,f)}{\mathrm{d}X} = -\frac{\tilde{\phi}^h_{E_i}(X,f)}{\lambda^h_{\mathrm{int},E_i}} - \frac{\tilde{\phi}^h_{E_i}(X,f)}{\lambda^h_{\mathrm{dec},E_i}(X)} + \sum_{E_k \geq E_i}\sum_l \frac{[\tilde{\varsigma}_{l(E_k)\to h(E_i)} \cdot \tilde{\phi}^l_{E_k}](f)}{\lambda^l_{\mathrm{int},E_k}} + \sum_{E_k \geq E_i}\sum_l \frac{[\tilde{\delta}_{l(E_k)\to h(E_i)} \cdot \tilde{\phi}^l_{E_k}](f)}{\lambda^l_{\mathrm{dec},E_k}(X)}. \tag{5}$$

For the 2D radial convolutions (as in the right panel of Fig. 1), the equivalent transform is the Hankel transform $\mathcal{H}$ [18, 19]. With discrete transforms, a finite number N of frequencies f_n is implied in Eq. (5), and the multiplication $[\tilde{\varsigma}_{l(E_k)\to h(E_i)} \cdot \tilde{\phi}^l_{E_k}](f)$ is performed independently for each f_n. This means that 2D cascade equation in MCEQ will preserve the matrix form and the computational advantages of the 1D MCEQ solution, albeit now requiring one to solve N matrix equations in parallel for each frequency mode or assembling a larger block-diagonal sparse matrix.

4. Validation and Benchmarking

To validate the numerical approach developed in Section 3.2, we solve Eq. (5) for a 100 GeV proton primary injected into the Earth's atmosphere at $\theta_0 = 0$ and the altitude $h_0 = 112.5$ km ($X_0 = 0\,\mathrm{g\,cm^{-2}}$). For the atmospheric profile, we choose the Linsley parametrization of the US Standard atmosphere. The combination of DPMJET-III 19.1 [2] ($E_i \leq 80$ GeV) and EPOS-LHC ($E_i > 80$ GeV) hadronic interaction models is used to generate the yields of the secondary particles as a function of their energy and angle relative to their immediate primary. To run the interaction models we use the new IMPY interface [3]. The energy grid is log-spaced following [11] and extends from 1 GeV to 2 TeV. The electromagnetic processes, including multiple scattering of the shower muons, as well as the deflection of charged particles in the geomagnetic field are not taken into account. For both of the convolution approaches, we use $N \simeq 400$ frequency modes f_n, and obtain the final fluxes in the θ space through the respective inverse transforms ($\mathcal{F}^{-1}$ or $\mathcal{H}^{-1}$) of $\tilde{\phi}^h_{E_i}(X, f_n)$.

For benchmarking, we use the CORSIKA Monte Carlo code, v.7.7410 [9], and perform 170,000 simulations of proton showers using the same atmospheric profile. As in MCEQ, EPOS-LHC is the high-energy (≥ 80 GeV) hadronic interaction model. At lower energies, CORSIKA is set to URQMD since DPMJET-III is not supported. The geomagnetic field is disabled, while the muon multiple scattering remains present in the simulations.

Fig. 2 shows the resulting angular distributions of the secondary muons from CORSIKA and those obtained via the method from Section 3.2 ("2D MCEQ"). We find a good agreement between the angular distributions obtained with 2D MCEQ (via the radial convolution and the Hankel transform) and CORSIKA for all altitudes and energy bins considered. These results are further cross-checked against the AIRES Monte Carlo [10] and the circular (Fourier) convolution method for 2D MCEQ in Fig. 3. The angle-integrated muon spectra are given in Fig. 4. We observe that the angular distributions returned by the circular convolution method are in a worse agreement with both CORSIKA and AIRES than the radial convolution. With the circular convolution, one consistently obtains more widely spread secondaries than predicted by both Monte Carlo codes. This is an intuitive

[2] https://github.com/DPMJET
[3] https://github.com/impy-project

PoS(ICRC2021)1209

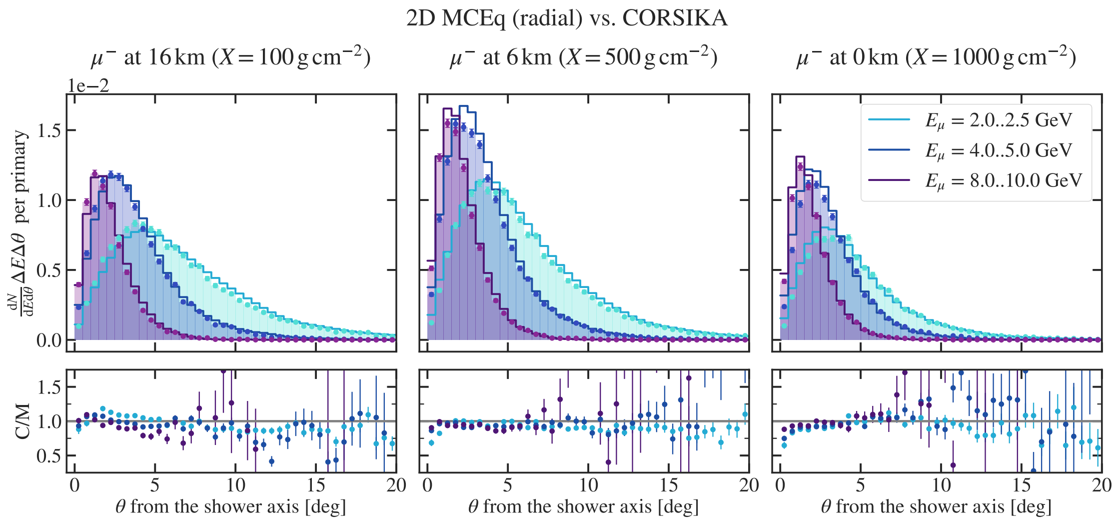

Figure 2: The angular distributions of secondary muons at three different altitudes: the numerical solution of Eq. (5) via MCEQ (solid line) as compared to the output of the CORSIKA simulations (shaded histogram). The primary particle inducing the hadronic cascade is a 100 GeV proton. The CORSIKA results are shown with their respective statistical errorbars. The MCEQ solution uses the radial (Hankel) convolution approach. The bottom panel provides the ratio of the CORSIKA:MCEQ angular spectra integrated within the 0.5° bins.

consequence of the fact that the secondary particle angle can only increase at each propagation step (i.e. the rotation illustrated in the left panel of Fig. 1 is performed strictly counter-clockwise). At $\theta = 0$, such a deficiency of the circular convolution approach turns out to be particularly problematic, and the bias of the respective angular spectra is most evident in the low-energy hadrons (top left panel of Fig. 3). This is expected as the angles of the hadronic interaction secondaries relative to their primaries are larger than the angles of the decay daughters relative to their parents. As the result, each circular convolution introduces a larger error for interactions than for decays.

Finally, we note that the CORSIKA and AIRES distributions are not fully in agreement with each other. This discrepancy could be attributed to the fact that AIRES employs a different hadronic interaction model, namely the Hillas splitting algorithm [20], at low energies, while the high-energy hadronic interaction model (EPOS-LHC) is matched with those of CORSIKA and MCEQ. At present, elucidating the origin of any disagreement between the two Monte Carlo codes falls beyond the scope of this work.

5. Conclusions

This study focused on extending MCEQ, a state-of-the-art numerical code for hadronic cascade evolution, to two dimensions. By treating angular development as a sequence of convolutions, we naturally incorporated it into the MCEQ framework. We compared two spectral convolution methods and benchmarked them against two Monte Carlo cascade codes, using an example of a proton-induced air shower. A very good agreement between the "2D MCEQ" solution and the output from a standard Monte Carlo code was reached. This suggests that our tool has a significant potential to be used as a fast and accurate alternative to the Monte Carlo cascade development approaches.

PoS(ICRC2021)1209

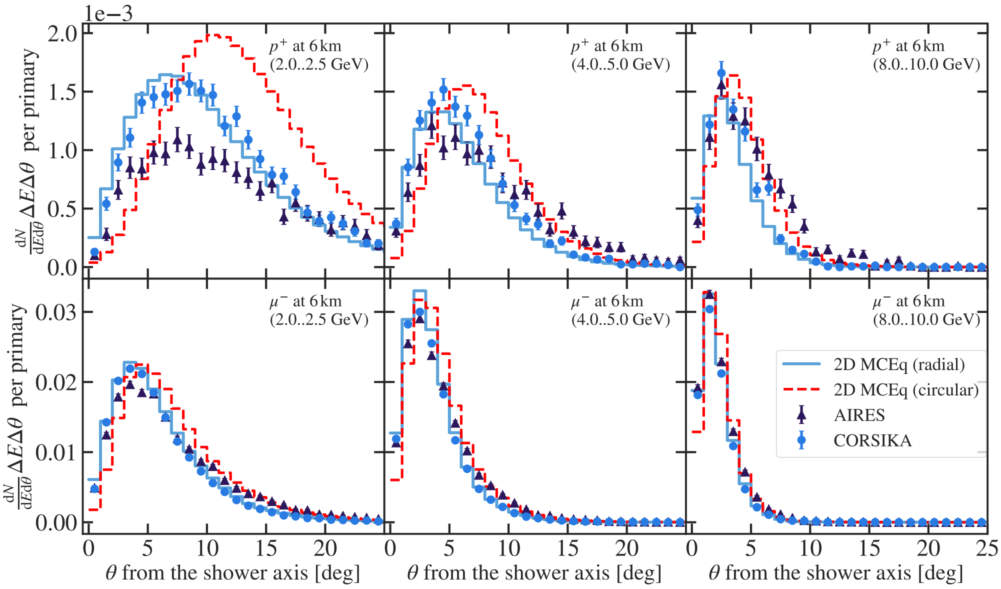

Figure 3: Comparison of the angular distributions of the secondary particles in a 100 GeV proton air shower as evaluated by the two numerical methods from this study (solid and dashed lines) and the two benchmark Monte Carlo codes (barred markers). The best agreement is reached between the 2D MCEQ solution with the radial convolution method and CORSIKA, which is most prominent in low-energy muons and protons.

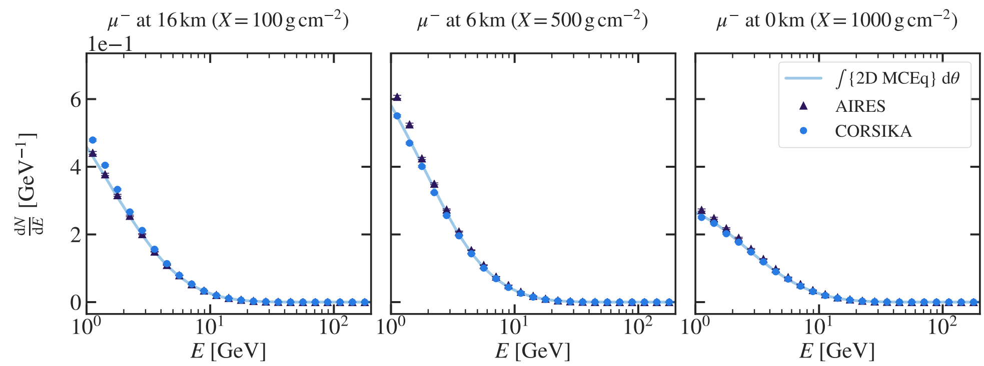

Figure 4: Angle-integrated muon spectra from 2D MCEQ (radial convolution method) as compared to those from CORSIKA and AIRES Monte Carlo simulations. All three codes are found to be in agreement.

6. Acknowledgements

TK and DJK acknowledge support from the Carlsberg Foundation (project no. 117238). AF acknowledges support from the JSPS (KAKENHI 19F19750).

References

[1] V. Agrawal, T.K. Gaisser, P. Lipari and T. Stanev, *Phys. Rev. D* **53** (1996) 1314.

[2] G.D. Barr, T.K. Gaisser, P. Lipari, S. Robbins and T. Stanev, *Phys. Rev. D* **70** (2004) 023006.

PoS(ICRC2021)1209

[3] M. Honda, T. Kajita, K. Kasahara, S. Midorikawa and T. Sanuki, *Phys. Rev. D* **75** (2007) 043006.

[4] M. Honda, M.S. Athar, T. Kajita, K. Kasahara and S. Midorikawa, *Phys. Rev. D* **92** (2015) 023004.

[5] P. Lipari, *Astropart. Phys.* **14** (2000) 153.

[6] G. Battistoni, J. Bauer, T.T. Boehlen, F. Cerutti, M.P.W. Chin, R. Dos Santos Augusto et al., *Front. Oncol.* **6** (2016) .

[7] S. Agostinelli et al., *Nucl. Instrum. Methods Phys. Res. A* **506** (2003) 250.

[8] T. Sato et al., *J. Nucl. Sci. Technol.* **55** (2018) 684.

[9] D. Heck, J. Knapp, J.N. Capdevielle, G. Schatz and T. Thouw, *Tech. Rep. FZKA-6019* (1998) .

[10] S.J. Sciutto, *arXiv:astro-ph/9911331* (2019) .

[11] A. Fedynitch, R. Engel, T.K. Gaisser, F. Riehn and T. Stanev, *arXiv:1503.00544* (2015) .

[12] A. Fedynitch, *Cascade equations and hadronic interactions at very high energies*, Ph.D. thesis, KIT, Karlsruhe, Dept. Phys., Nov., 2015.

[13] A. Fedynitch, F. Riehn, R. Engel, T.K. Gaisser and T. Stanev, *Phys. Rev. D* **100** (2019) 103018.

[14] T. Pierog, I. Karpenko, J.M. Katzy, E. Yatsenko and K. Werner, *Phys. Rev. C* **92** (2015) 034906.

[15] M. Bleicher, E. Zabrodin, C. Spieles, S.A. Bass, C. Ernst, S. Soff et al., *J. Phys. G: Nucl. Part. Phys.* **25** (1999) 1859.

[16] S. Roesler, R. Engel and J. Ranft, in *Advanced Monte Carlo for Radiation Physics, Particle Transport Simulation and Applications*, A. Kling, F.J.C. Baräo, M. Nakagawa, L. Távora and P. Vaz, eds., (Berlin, Heidelberg), pp. 1033–1038, Springer, 2001.

[17] T. Sjöstrand, S. Ask, J.R. Christiansen, R. Corke, N. Desai, P. Ilten et al., *Comput. Phys. Commun.* **191** (2015) 159.

[18] N. Baddour, *J. Opt. Soc. Am. A* **26** (2009) 1767.

[19] M. Guizar-Sicairos and J.C. Gutiérrez-Vega, *JOSA A* **21** (2004) 53.

[20] A.M. Hillas in *Proc. of the Paris Workshop on Cascade Simulations*, J. Linsley and A.M. Hillas, eds., p. 39 (1981).

PoS(ICRC2021)1209

Bibliography

[1] A. Fedynitch et al. "Calculation of conventional and prompt lepton fluxes at very high energy". In: *EPJ Web Conf.* 99 (2015). Ed. by D. Berge et al., p. 08001. DOI: 10.1051/epjconf/20159908001. arXiv: 1503.00544 [hep-ph].

[2] A. Fedynitch et al. "Hadronic interaction model sibyll 2.3c and inclusive lepton fluxes". In: *Phys. Rev. D* 100.10 (2019), p. 103018. DOI: 10.1103/PhysRevD.100.103018. arXiv: 1806.04140 [hep-ph].

[3] IMPY: *Hadronic Interaction Models in Python*. 2022. URL: https://github.com/impy-project/impy (visited on 09/05/2022).

[4] T. Kozynets, A. Fedynitch, and D. J. Koskinen. "A Numerical Approach to Angular Distributions in Hadronic Cascades". In: *PoS* ICRC2021 (2021), p. 1209. DOI: 10.22323/1.395.1209.

[5] T. Kozynets. *A Novel Numerical Approach to Angular Distributions of Atmospheric Neutrinos*. June 2022. DOI: 10.5281/zenodo.6767375. URL: https://doi.org/10.5281/zenodo.6767375.

[6] C. A. Coulomb. *Mémoires sur l'électricité et la magnétisme*. fre. Paris : Chez Bachelier, 1789. URL: http://archive.org/details/mmoiressurllectr00coul (visited on 08/14/2022).

[7] J. Elster and H. Geitel. "Ueber Elektricitätszerstreuung in der Luft". en. In: *Annalen der Physik* 307.7 (1900), pp. 425–446. ISSN: 1521-3889. DOI: 10.1002/andp.19003070702. URL: https://onlinelibrary.wiley.com/doi/abs/10.1002/andp.19003070702 (visited on 08/14/2022).

[8] M. Walter and A. W. Wolfendale. "Early history of cosmic particle physics". en. In: *The European Physical Journal H* 37.3 (Aug. 2012), pp. 323–358. ISSN: 2102-6467. DOI: 10.1140/epjh/e2012-30020-1. URL: https://doi.org/10.1140/epjh/e2012-30020-1 (visited on 08/14/2022).

[9] T. Wulf. "Über den Ursprung der in der Atmosphäre vorhandenen γ-Strahlung". In: *Physik Z* 10 (1909), pp. 997–1003.

[10] H. Becquerel. "Sur les radiations invisibles émises par les corps phosphorescents". In: *Comptes rendus* 122.1896 (1896), pp. 501–503. URL: http://gallica.bnf.fr/ark:/12148/bpt6k30780.image.f503.

[11] D. Pacini. “La radiazione penetrante alla superficie ed in seno alle acque”. In: *Nuovo Cimento* 3 (Dec. 1912), pp. 93–100. DOI: 10.1007/BF02957440. URL: https://ui.adsabs.harvard.edu/abs/1912NCim....3..93P (visited on 08/14/2022).

[12] D. Pacini. “La radiation pénétrante sur la mer”. fr. In: *Le Radium* 8.8 (Aug. 1911). Publisher: MASSON ET CIE, Editeurs, pp. 307–312. ISSN: 0370-3223. DOI: 10.1051/radium:0191100808030701. URL: http://dx.doi.org/10.1051/radium:0191100808030701 (visited on 08/14/2022).

[13] D. Pacini. *Penetrating Radiation at the Surface of and in Water*. Number: arXiv:1002.1810 arXiv:1002.1810 [astro-ph, physics:physics]. Aug. 2017. DOI: 10.48550/arXiv.1002.1810. URL: http://arxiv.org/abs/1002.1810 (visited on 08/14/2022).

[14] F. Linke. “Luftelektrische Messungen bei zwölf Ballonfahrte”. In: *Abhandlungen der Gesellschaft der Wissenschaften in Göttingen Mathematisch-Physikalische Klasse* 3 (1904), pp. 1–90.

[15] T. Wulf. “Beobachtungen über Strahlung hoher Durchdringungsfähigkeit auf dem Eiffelturm”. In: *Physik Z* 11 (1910), pp. 811–813.

[16] A. Gockel. “Luftelektrische Beobachtungen bei einer Ballonfahrt”. In: *Physik Z* 11 (1910), pp. 280–282.

[17] A. Gockel. “Messungen der durchdringenden Strahlung bei Ballonfahrten”. In: *Physik Z* 12 (1911), pp. 595–597.

[18] V. F. Hess. “Über Beobachtungen der durchdringenden Strahlung bei sieben Freiballonfahrten”. In: *Phys. Z.* 13 (1912), pp. 1084–1091.

[19] W. Kolhörster. “Messungen der durchdringenden Strahlung am Erdboden und bei Ballonfahrten in grösseren Höhen”. German. In: *Phys. Z.* 14 (1914). OCLC: 257569088, pp. 1153–1155.

[20] W. Kolhörster. “Messungen der durchdringenden Strahlungen bis in Höhen von 9300 m”. In: *Verh. Deutsche Phys. Gesellschaft* 16 (1914), pp. 719–721.

[21] E. Regener. “Intensity of Cosmic Radiation in the High Atmosphere”. en. In: *Nature* 130.3279 (Sept. 1932). Number: 3279 Publisher: Nature Publishing Group, pp. 364–364. ISSN: 1476-4687. DOI: 10.1038/130364a0. URL: https://www.nature.com/articles/130364a0 (visited on 08/14/2022).

[22] D. Skobelzyn. “Über eine neue Art sehr schneller β-Strahlen”. de. In: *Zeitschrift für Physik* 54.9 (Sept. 1929), pp. 686–702. ISSN: 0044-3328. DOI: 10.1007/BF01341600. URL: https://doi.org/10.1007/BF01341600 (visited on 10/13/2022).

[23] H. Geiger and W. Müller. "Elektronenzählrohr zur Messung schwächster Aktivitäten". de. In: *Naturwissenschaften* 16.31 (Aug. 1928), pp. 617–618. ISSN: 1432-1904. DOI: 10.1007/BF01494093. URL: https://doi.org/10.1007/BF01494093 (visited on 10/13/2022).

[24] W. Bothe and W. Kolhörster. "Das Wesen der Höhenstrahlung". de. In: *Zeitschrift für Physik* 56.11 (Nov. 1929), pp. 751–777. ISSN: 0044-3328. DOI: 10.1007/BF01340137. URL: https://doi.org/10.1007/BF01340137 (visited on 08/15/2022).

[25] A. H. Compton and R. N. Turner. "Cosmic Rays on the Pacific Ocean". In: *Phys. Rev.* 52 (8 Oct. 1937), pp. 799–814. DOI: 10.1103/PhysRev.52.799. URL: https://link.aps.org/doi/10.1103/PhysRev.52.799.

[26] B. Rossi. "Über den Ursprung der durchdringenden Korpuskularstrahlung der Atmosphäre". de. In: *Zeitschrift für Physik* 68.1 (Jan. 1931), pp. 64–84. ISSN: 0044-3328. DOI: 10.1007/BF01392728. URL: https://doi.org/10.1007/BF01392728 (visited on 10/13/2022).

[27] L. Alvarez and A. H. Compton. "A Positively Charged Component of Cosmic Rays". In: *Phys. Rev.* 43 (10 May 1933), pp. 835–836. DOI: 10.1103/PhysRev.43.835. URL: https://link.aps.org/doi/10.1103/PhysRev.43.835.

[28] B. Rossi. "Arcetri, 1928 – 1932". en. In: *Early History of Cosmic Ray Studies: Personal Reminiscences with Old Photographs*. Ed. by Y. Sekido and H. Elliot. Astrophysics and Space Science Library. Dordrecht: Springer Netherlands, 1985, pp. 53–73. ISBN: 978-94-009-5434-2. DOI: 10.1007/978-94-009-5434-2_7. URL: https://doi.org/10.1007/978-94-009-5434-2_7 (visited on 10/13/2022).

[29] M. Schein, W. P. Jesse, and E. O. Wollan. "The Nature of the Primary Cosmic Radiation and the Origin of the Mesotron". In: *Physical Review* 59.7 (Apr. 1941). Publisher: American Physical Society, pp. 615–615. DOI: 10.1103/PhysRev.59.615. URL: https://link.aps.org/doi/10.1103/PhysRev.59.615 (visited on 08/15/2022).

[30] L. Bonolis. "Walther Bothe and Bruno Rossi: The birth and development of coincidence methods in cosmic-ray physics". In: *American Journal of Physics* 79.11 (Nov. 2011). Publisher: American Association of Physics Teachers, pp. 1133–1150. ISSN: 0002-9505. DOI: 10.1119/1.3619808. URL: https://aapt.scitation.org/doi/10.1119/1.3619808 (visited on 08/15/2022).

[31] B. Rossi. "Über die Eigenschaften der durchdringenden Korpuskularstrahlung im Meeresniveau". de. In: *Zeitschrift für Physik* 82.3 (Mar. 1933), pp. 151–178. ISSN: 0044-3328. DOI: 10.1007/BF01341486. URL: https://doi.org/10.1007/BF01341486 (visited on 08/16/2022).

[32] K. Schmeiser and W. Bothe. "Die harten Ultrastrahlschauer". In: *Annalen der Physik* 424.1-2 (1938), pp. 161–177. DOI: https://doi.org/10.1002/andp.19384240119. eprint: https://onlinelibrary.wiley.com/doi/pdf/10.1002/andp.19384240119. URL: https://onlinelibrary.wiley.com/doi/abs/10.1002/andp.19384240119.

[33] P. Auger et al. "Extensive Cosmic-Ray Showers". In: *Rev. Mod. Phys.* 11 (3-4 July 1939), pp. 288–291. DOI: 10.1103/RevModPhys.11.288. URL: https://link.aps.org/doi/10.1103/RevModPhys.11.288.

[34] K.-H. Kampert and A. A. Watson. "Extensive air showers and ultra high-energy cosmic rays: a historical review". In: *The European Physical Journal H* 37.3 (July 2012), pp. 359–412. DOI: 10.1140/epjh/e2012-30013-x. URL: https://doi.org/10.1140%2Fepjh%2Fe2012-30013-x.

[35] T. K. Gaisser, T. Stanev, and S. Tilav. "Cosmic Ray Energy Spectrum from Measurements of Air Showers". In: *Front. Phys. (Beijing)* 8 (2013), pp. 748–758. DOI: 10.1007/s11467-013-0319-7. arXiv: 1303.3565 [astro-ph.HE].

[36] B. Peters. "Primary cosmic radiation and extensive air showers". English. In: *Nuovo Cimento* 22.4 (Nov. 1961). Institution: Univ. of Copenhagen. ISSN: 0029-6341. DOI: 10.1007/BF02783106. URL: https://www.osti.gov/biblio/4817971 (visited on 10/13/2022).

[37] H. J. Bhabha, W. Heitler, and N. F. Mott. "The passage of fast electrons and the theory of cosmic showers". In: *Proceedings of the Royal Society of London. Series A - Mathematical and Physical Sciences* 159.898 (Apr. 1937). Publisher: Royal Society, pp. 432–458. DOI: 10.1098/rspa.1937.0082. URL: https://royalsocietypublishing.org/doi/10.1098/rspa.1937.0082 (visited on 10/13/2022).

[38] C. D. Anderson and S. H. Neddermeyer. "Cloud Chamber Observations of Cosmic Rays at 4300 Meters Elevation and Near Sea-Level". In: *Phys. Rev.* 50 (4 Aug. 1936), pp. 263–271. DOI: 10.1103/PhysRev.50.263. URL: https://link.aps.org/doi/10.1103/PhysRev.50.263.

[39] S. H. Neddermeyer and C. D. Anderson. "Note on the Nature of Cosmic-Ray Particles". In: *Phys. Rev.* 51 (10 May 1937), pp. 884–886. DOI: 10.1103/PhysRev.51.884. URL: https://link.aps.org/doi/10.1103/PhysRev.51.884.

[40] H. Yukawa. "On the Interaction of Elementary Particles I". In: *Proc. Phys. Math. Soc. Jap.* 17 (1935), pp. 48–57. DOI: 10.1143/PTPS.1.1. URL: https://www.jstage.jst.go.jp/article/ppmsj1919/17/0/17_0_48/_pdf/-char/en.

[41] H. A. Bethe and L. W. Nordheim. "On the Theory of Meson Decay". In: *Phys. Rev.* 57 (11 June 1940), pp. 998–1006. DOI: 10.1103/PhysRev.57.998. URL: https://link.aps.org/doi/10.1103/PhysRev.57.998.

[42] G. P. S. Occhialini and C. F. Powell. "Nuclear disintegration produced by slow charged particles of small mass". In: *Nature* 159 (1947), pp. 186–190. DOI: 10.1038/159186a0.

[43] D. H. Perkins. "Nuclear disintegration by meson capture". In: *Nature* 159 (1947), pp. 126–127. DOI: 10.1038/159126a0.

[44] G. D. Rochester and C. C. Butler. "Evidence for the Existence of New Unstable Elementary Particles". In: *Nature* 160 (1947), pp. 855–857. DOI: 10.1038/160855a0.

[45] C. V. Achar et al. "Detection of muons produced by cosmic ray neutrinos deep underground". In: *Phys. Lett.* 18 (1965), pp. 196–199. DOI: 10.1016/0031-9163(65)90712-2.

[46] F. Reines et al. "Evidence for high-energy cosmic ray neutrino interactions". In: *Phys. Rev. Lett.* 15 (1965), pp. 429–433. DOI: 10.1103/PhysRevLett.15.429.

[47] J. Chadwick. "Intensitätsverteilung im magnetischen Spectrum der β-Strahlen von radium B + C". ger. In: 16 (1914), p. 383.

[48] C. D. Ellis, W. A. Wooster, and E. Rutherford. "The average energy of disintegration of radium E". In: *Proceedings of the Royal Society of London. Series A, Containing Papers of a Mathematical and Physical Character* 117.776 (Dec. 1927). Publisher: Royal Society, pp. 109–123. DOI: 10.1098/rspa.1927.0168. URL: https://royalsocietypublishing.org/doi/10.1098/rspa.1927.0168 (visited on 10/13/2022).

[49] W. Pauli. "Dear radioactive ladies and gentlemen". In: *Phys. Today* 31N9 (1978), p. 27.

[50] Q. R. Ahmad et al. "Direct evidence for neutrino flavor transformation from neutral current interactions in the Sudbury Neutrino Observatory". In: *Phys. Rev. Lett.* 89 (2002), p. 011301. DOI: 10.1103/PhysRevLett.89.011301. arXiv: nucl-ex/0204008.

[51] Y. Fukuda et al. "Evidence for oscillation of atmospheric neutrinos". In: *Phys. Rev. Lett.* 81 (1998), pp. 1562–1567. DOI: 10.1103/PhysRevLett.81.1562. arXiv: hep-ex/9807003.

[52] F. J. Escrihuela et al. "On the description of nonunitary neutrino mixing". In: *Phys. Rev. D* 92.5 (2015). [Erratum: Phys.Rev.D 93, 119905 (2016)], p. 053009. DOI: 10.1103/PhysRevD.92.053009. arXiv: 1503.08879 [hep-ph].

[53] O. G. Miranda and J. W. F. Valle. "Neutrino oscillations and the seesaw origin of neutrino mass". In: *Nucl. Phys. B* 908 (2016), pp. 436–455. DOI: 10.1016/j.nuclphysb.2016.03.027. arXiv: 1602.00864 [hep-ph].

[54] T. Sarkar. "Effect of non-unitary neutrino mixing in Lorentz violation and dark NSI". In: (Sept. 2022). arXiv: 2209.10233 [hep-ph].

[55] D. Heck et al. "CORSIKA: A Monte Carlo code to simulate extensive air showers". In: (Feb. 1998).

[56] S. J. Sciutto. "AIRES: A system for air shower simulations". In: (Nov. 1999). DOI: 10.13140/RG.2.2.12566.40002. arXiv: astro-ph/9911331.

[57] M. Honda et al. "Improvement of low energy atmospheric neutrino flux calculation using the JAM nuclear interaction model". In: *Phys. Rev. D* 83 (2011), p. 123001. DOI: 10.1103/PhysRevD.83.123001. arXiv: 1102.2688 [astro-ph.HE].

[58] G. D. Barr et al. "A Three - dimensional calculation of atmospheric neutrinos". In: *Phys. Rev. D* 70 (2004), p. 023006. DOI: 10.1103/PhysRevD.70.023006. arXiv: astro-ph/0403630.

[59] M. Honda et al. "Atmospheric neutrino flux calculation using the NRLMSISE-00 atmospheric model". In: *Phys. Rev. D* 92.2 (2015), p. 023004. DOI: 10.1103/PhysRevD.92.023004. arXiv: 1502.03916 [astro-ph.HE].

[60] M. Honda et al. "Reduction of the uncertainty in the atmospheric neutrino flux prediction below 1 GeV using accurately measured atmospheric muon flux". In: *Phys. Rev. D* 100.12 (2019), p. 123022. DOI: 10.1103/PhysRevD.100.123022. arXiv: 1908.08765 [astro-ph.HE].

[61] T. K. Gaisser, R. Engel, and E. Resconi. *Cosmic Rays and Particle Physics*. Cambridge University Press, 2016.

[62] A. Fedynitch. "Cascade equations and hadronic interactions at very high energies". PhD thesis. KIT, Karlsruhe, Dept. Phys., Nov. 2015. DOI: 10.5445/IR/1000055433.

[63] P. Lipari. "The Geometry of atmospheric neutrino production". In: *Astropart. Phys.* 14 (2000), pp. 153–170. DOI: 10.1016/S0927-6505(00)00129-8. arXiv: hep-ph/0002282.

[64] Y. Tserkovnyak et al. "A Three-dimensional calculation of atmospheric neutrino fluxes". In: *Astropart. Phys.* 18 (2003), pp. 449–461. DOI: 10.1016/S0927-6505(02)00159-7. arXiv: hep-ph/9907450.

[65] G. Battistoni et al. "A Three-dimensional calculation of atmospheric neutrino flux". In: *Astropart. Phys.* 12 (2000), pp. 315–333. DOI: 10.1016/S0927-6505(99)00110-3. arXiv: hep-ph/9907408.

[66] A. Ishihara. "The IceCube Upgrade - Design and Science Goals". In: *PoS* ICRC2019 (2021), p. 1031. doi: 10.22323/1.358.1031. arXiv: 1908.09441 [astro-ph.HE].

[67] K. Abe et al. "Letter of Intent: The Hyper-Kamiokande Experiment — Detector Design and Physics Potential —". In: (Sept. 2011). arXiv: 1109.3262 [hep-ex].

[68] S. Adrian-Martinez et al. "Letter of intent for KM3NeT 2.0". In: *J. Phys. G* 43.8 (2016), p. 084001. doi: 10.1088/0954-3899/43/8/084001. arXiv: 1601.07459 [astro-ph.IM].

[69] K. J. Kelly et al. "Sub-GeV Atmospheric Neutrinos and CP-Violation in DUNE". In: *Phys. Rev. Lett.* 123.8 (2019), p. 081801. doi: 10.1103/PhysRevLett.123.081801. arXiv: 1904.02751 [hep-ph].

[70] A. Abusleme et al. "JUNO sensitivity to low energy atmospheric neutrino spectra". In: *Eur. Phys. J. C* 81 (2021), p. 10. doi: 10.1140/epjc/s10052-021-09565-z. arXiv: 2103.09908 [hep-ex].

[71] M. Thomson. *Modern particle physics*. New York: Cambridge University Press, 2013. isbn: 978-1-107-03426-6.

[72] A. J. Larkoski. *Elementary Particle Physics: An Intuitive Introduction*. Cambridge University Press, June 2019. isbn: 978-1-108-49698-8, 978-1-108-57940-7.

[73] P. Langacker. *The Standard Model and Beyond*. Taylor & Francis, 2017. isbn: 978-1-4987-6322-6, 978-1-4987-6321-9, 978-0-367-57344-7, 978-1-315-17062-6. doi: 10.1201/b22175.

[74] J. Schwichtenberg. *No-Nonsense Quantum Field Theory: A Student-Friendly Introduction*. en. Google-Books-ID: 4AjbDwAAQBAJ. No-Nonsense Books, Mar. 2020.

[75] D. Griffiths. *Introduction to elementary particles*. 2008. isbn: 978-3-527-40601-2.

[76] J. Ellis. "Outstanding questions: Physics beyond the Standard Model". In: *Phil. Trans. Roy. Soc. Lond. A* 370 (2012), pp. 818–830. doi: 10.1098/rsta.2011.0452.

[77] Y. Gouttenoire. "Beyond the Standard Model Cocktail". In: (July 2022). arXiv: 2207.01633 [hep-ph].

[78] P. Draper, I. G. Garcia, and M. Reece. "Snowmass White Paper: Implications of Quantum Gravity for Particle Physics". In: *2022 Snowmass Summer Study*. Mar. 2022. arXiv: 2203.07624 [hep-ph].

[79] A. Addazi et al. "Quantum gravity phenomenology at the dawn of the multi-messenger era—A review". In: *Prog. Part. Nucl. Phys.* 125 (2022), p. 103948. doi: 10.1016/j.ppnp.2022.103948. arXiv: 2111.05659 [hep-ph].

[80] R. L. Workman et al. "Review of Particle Physics". In: *PTEP* 2022 (2022), p. 083C01. DOI: 10.1093/ptep/ptac097.

[81] C. S. Wu et al. "Experimental Test of Parity Conservation in β Decay". In: *Phys. Rev.* 105 (1957), pp. 1413–1414. DOI: 10.1103/PhysRev.105.1413.

[82] R. P. Feynman. "The behavior of hadron collisions at extreme energies". In: *Conf. Proc. C* 690905 (1969), pp. 237–258.

[83] M. Gell-Mann. "The Eightfold Way: A Theory of strong interaction symmetry". In: (Mar. 1961). DOI: 10.2172/4008239.

[84] G. Zweig. "An SU(3) model for strong interaction symmetry and its breaking. Version 2". In: *Develoments in the Quark Theory of Hadrons. Vol. 1. 1964 - 1978*. Ed. by D. B. Lichtenberg and S. P. Rosen. Feb. 1964, pp. 22–101.

[85] *DESY News: The most precise picture of the proton*. en. URL: https://www.desy.de/news/news_search/index_eng.html?openDirectAnchor=829 (visited on 10/19/2022).

[86] A. Deur, S. J. Brodsky, and G. F. de Teramond. "The QCD Running Coupling". In: *Nucl. Phys.* 90 (2016), p. 1. DOI: 10.1016/j.ppnp.2016.04.003. arXiv: 1604.08082 [hep-ph].

[87] G. Altarelli and G. Parisi. "Asymptotic Freedom in Parton Language". In: *Nucl. Phys. B* 126 (1977), pp. 298–318. DOI: 10.1016/0550-3213(77)90384-4.

[88] L. A. Harland-Lang et al. "Parton distributions in the LHC era: MMHT 2014 PDFs". In: *Eur. Phys. J. C* 75.5 (2015), p. 204. DOI: 10.1140/epjc/s10052-015-3397-6. arXiv: 1412.3989 [hep-ph].

[89] A. M. Cooper-Sarkar. "PDF Fits at HERA". In: *PoS* EPS-HEP2011 (2011), p. 320. DOI: 10.22323/1.134.0320. arXiv: 1112.2107 [hep-ph].

[90] T. Regge. "Introduction to complex orbital momenta". en. In: *Il Nuovo Cimento (1955-1965)* 14.5 (Dec. 1959), pp. 951–976. ISSN: 1827-6121. DOI: 10.1007/BF02728177. URL: https://doi.org/10.1007/BF02728177 (visited on 10/19/2022).

[91] I. I. Pomeranchuk. "Equality of the nucleon and antinucleon total interaction cross section at high energies". en. In: *Journal of Experimental and Theoretical Physics* 34 (1958), p. 725. URL: https://cds.cern.ch/record/406311 (visited on 10/19/2022).

[92] L. A. Tompkins. "A Measurement of the proton-proton inelastic scattering cross-section at $\sqrt{s}$ =7 TeV with the ATLAS detector at the LHC". en. PhD thesis. UC Berkeley, 2011. URL: https://escholarship.org/uc/item/4m34b24r (visited on 10/19/2022).

[93] A. Donnachie and P. V. Landshoff. "Total cross-sections". In: *Phys. Lett. B* 296 (1992), pp. 227–232. DOI: 10.1016/0370-2693(92)90832-O. arXiv: hep-ph/9209205.

[94] R. J. Glauber and G. Matthiae. "High-energy scattering of protons by nuclei". In: *Nucl. Phys. B* 21 (1970), pp. 135–157. DOI: 10.1016/0550-3213(70)90511-0.

[95] H.-U. Bengtsson and T. Sjostrand. "The Lund Monte Carlo for Hadronic Processes: Pythia Version 4.8". In: *Comput. Phys. Commun.* 46 (1987), p. 43. DOI: 10.1016/0010-4655(87)90036-1.

[96] P. Lipari. "Lepton spectra in the earth's atmosphere". In: *Astropart. Phys.* 1 (1993), pp. 195–227. DOI: 10.1016/0927-6505(93)90022-6.

[97] S. Mine. "Systematic measurement of the spin-polarization of the cosmic-ray muons". English. PhD thesis. Institute for Nuclear Study, University of Tokyo, 1996. URL: https://repository.dl.itc.u-tokyo.ac.jp/record/2005339/files/A12180.pdf.

[98] M. Goldhaber, L. Grodzins, and A. W. Sunyar. "Helicity of Neutrinos". In: *Phys. Rev.* 109 (1958), pp. 1015–1017. DOI: 10.1103/PhysRev.109.1015.

[99] L. P. Roesch et al. "Direct measurement of the helicity of the muonic neutrino". en. In: *American Journal of Physics* 50.10 (June 1998). Publisher: American Association of Physics TeachersAAPT, p. 931. ISSN: 0002-9505. DOI: 10.1119/1.13016. URL: https://aapt.scitation.org/doi/abs/10.1119/1.13016 (visited on 10/21/2022).

[100] D. Buskulic et al. "Correlation measurements in $Z \rightarrow \tau^+\tau^-$ and the τ neutrino helicity". en. In: *Physics Letters B* 321.1 (Jan. 1994), pp. 168–176. ISSN: 0370-2693. DOI: 10.1016/0370-2693(94)90345-X. URL: https://www.sciencedirect.com/science/article/pii/037026939490345X (visited on 10/21/2022).

[101] D. Buskulic et al. "Michel parameters and τ neutrino helicity from decay correlations in $Z \rightarrow \tau^+\tau^-$". en. In: *Physics Letters B* 346.3 (Mar. 1995), pp. 379–388. ISSN: 0370-2693. DOI: 10.1016/0370-2693(95)00107-V. URL: https://www.sciencedirect.com/science/article/pii/037026939500107V (visited on 10/21/2022).

[102] J. P. Alexander et al. "Determination of the Michel parameters and the τ neutrino helicity in τ decay". en. In: *Physical Review D* 56.9 (Nov. 1997), pp. 5320–5329. ISSN: 0556-2821, 1089-4918. DOI: 10.1103/PhysRevD.56.5320. URL: https://link.aps.org/doi/10.1103/PhysRevD.56.5320 (visited on 10/21/2022).

[103] K. Abe et al. "Measurement of the tau-neutrino helicity and the Michel parameters in polarized e+ e- collisions". In: *Phys. Rev. Lett.* 78 (1997), pp. 4691–4696. DOI: 10.1103/PhysRevLett.78.4691. arXiv: hep-ex/9701020.

[104] S. C. Curran, J. Angus, and A. L. Cockcroft. "Beta Spectrum of Tritium". en. In: *Nature* 162.4112 (Aug. 1948). Number: 4112 Publisher: Nature Publishing Group, pp. 302–303. ISSN: 1476-4687. DOI: 10.1038/162302a0. URL: https://www.nature.com/articles/162302a0 (visited on 10/21/2022).

[105] M. Aker et al. "Improved Upper Limit on the Neutrino Mass from a Direct Kinematic Method by KATRIN". In: *Phys. Rev. Lett.* 123.22 (2019), p. 221802. DOI: 10.1103/PhysRevLett.123.221802. arXiv: 1909.06048 [hep-ex].

[106] J. A. Formaggio, A. L. C. de Gouvêa, and R. G. H. Robertson. "Direct Measurements of Neutrino Mass". In: *Phys. Rept.* 914 (2021), pp. 1–54. DOI: 10.1016/j.physrep.2021.02.002. arXiv: 2102.00594 [nucl-ex].

[107] S. Alam et al. "Completed SDSS-IV extended Baryon Oscillation Spectroscopic Survey: Cosmological implications from two decades of spectroscopic surveys at the Apache Point Observatory". In: *Phys. Rev. D* 103.8 (2021), p. 083533. DOI: 10.1103/PhysRevD.103.083533. arXiv: 2007.08991 [astro-ph.CO].

[108] T. M. C. Abbott et al. "Dark Energy Survey Year 3 results: Cosmological constraints from galaxy clustering and weak lensing". In: *Phys. Rev. D* 105.2 (2022), p. 023520. DOI: 10.1103/PhysRevD.105.023520. arXiv: 2105.13549 [astro-ph.CO].

[109] N. Palanque-Delabrouille et al. "Hints, neutrino bounds and WDM constraints from SDSS DR14 Lyman-α and Planck full-survey data". In: *JCAP* 04 (2020), p. 038. DOI: 10.1088/1475-7516/2020/04/038. arXiv: 1911.09073 [astro-ph.CO].

[110] M. C. Gonzalez-Garcia, M. Maltoni, and T. Schwetz. "NuFIT: Three-Flavour Global Analyses of Neutrino Oscillation Experiments". In: *Universe* 7.12 (2021), p. 459. DOI: 10.3390/universe7120459. arXiv: 2111.03086 [hep-ph].

[111] S. M. Bilenky. "Neutrino in Standard Model and beyond". In: *Phys. Part. Nucl.* 46.4 (2015), pp. 475–496. DOI: 10.1134/S1063779615040024. arXiv: 1501.00232 [hep-ph].

[112] M. Bustamante. "NuOscProbExact: a general-purpose code to compute exact two-flavor and three-flavor neutrino oscillation probabilities". In: (2019). arXiv: 1904.12391 [hep-ph].

[113] I. Esteban et al. "The fate of hints: updated global analysis of three-flavor neutrino oscillations". In: *JHEP* 09 (2020), p. 178. DOI: 10.1007/JHEP09(2020)178. arXiv: 2007.14792 [hep-ph].

[114] H. P. Dembinski et al. "Data-driven model of the cosmic-ray flux and mass composition from 10 GeV to 10^{11} GeV". In: *PoS* ICRC2017 (2018), p. 533. DOI: 10.22323/1.301.0533. arXiv: 1711.11432 [astro-ph.HE].

[115] J. Albrecht et al. "The Muon Puzzle in cosmic-ray induced air showers and its connection to the Large Hadron Collider". In: *Astrophys. Space Sci.* 367.3 (2022), p. 27. DOI: 10.1007/s10509-022-04054-5. arXiv: 2105.06148 [astro-ph.HE].

[116] S. Bravo. *IceCube unveils the world's most precise search for mysterious new neutrino interactions*. en-US. Jan. 14, 2022. URL: https://icecube.wisc.edu/news/research/2022/01/icecube-unveils-the-worlds-most-precise-search-for-mysterious-new-neutrino-interactions/ (visited on 10/21/2022).

[117] M. G. Aartsen et al. "Measurement of the multi-TeV neutrino cross section with IceCube using Earth absorption". In: *Nature* 551 (2017), pp. 596–600. DOI: 10.1038/nature24459. arXiv: 1711.08119 [hep-ex].

[118] J. M. Picone et al. "NRLMSISE-00 empirical model of the atmosphere: Statistical comparisons and scientific issues". In: *Journal of Geophysical Research (Space Physics)* 107.A12, 1468 (Dec. 2002), p. 1468. DOI: 10.1029/2002JA009430.

[119] M. Wallraff and C. Wiebusch. "Calculation of oscillation probabilities of atmospheric neutrinos using nuCraft". In: *Comput. Phys. Commun.* 197 (2015), pp. 185–189. DOI: 10.1016/j.cpc.2015.07.010. arXiv: 1409.1387 [astro-ph.IM].

[120] A. M. Dziewonski and D. L. Anderson. "Preliminary reference earth model". In: *Phys. Earth Planet. Interiors* 25 (1981), pp. 297–356. DOI: 10.1016/0031-9201(81)90046-7.

[121] S. P. Mikheyev and A. Y. Smirnov. "Resonance Amplification of Oscillations in Matter and Spectroscopy of Solar Neutrinos". In: *Sov. J. Nucl. Phys.* 42 (1985), pp. 913–917.

[122] L. Wolfenstein. "Neutrino Oscillations in Matter". In: *Phys. Rev. D* 17 (1978), pp. 2369–2374. DOI: 10.1103/PhysRevD.17.2369.

[123] S. Roesler, R. Engel, and J. Ranft. "The Monte Carlo event generator DPMJET-III". In: *International Conference on Advanced Monte Carlo for Radiation Physics, Particle Transport Simulation and Applications (MC 2000)*. Dec. 2000, pp. 1033–1038. DOI: 10.1007/978-3-642-18211-2_166. arXiv: hep-ph/0012252.

[124] S. A. Bass et al. "Microscopic models for ultrarelativistic heavy ion collisions". In: *Prog. Part. Nucl. Phys.* 41 (1998), pp. 255–369. DOI: 10.1016/S0146-6410(98)00058-1. arXiv: nucl-th/9803035.

[125] F. Riehn et al. "A new version of the event generator Sibyll". In: *PoS* ICRC2015 (2016), p. 558. DOI: 10.22323/1.236.0558. arXiv: 1510.00568 [hep-ph].

[126] T. Pierog et al. "EPOS LHC: Test of collective hadronization with data measured at the CERN Large Hadron Collider". In: *Phys. Rev. C* 92.3 (2015), p. 034906. DOI: 10.1103/PhysRevC.92.034906. arXiv: 1306.0121 [hep-ph].

[127] C. Bierlich et al. "A comprehensive guide to the physics and usage of PYTHIA 8.3". In: (Mar. 2022). arXiv: 2203.11601 [hep-ph].

[128] N. Baddour. "Operational and convolution properties of two-dimensional Fourier transforms in polar coordinates". In: *J. Opt. Soc. Am. A* 26.8 (Aug. 2009), pp. 1767–1777. DOI: 10.1364/JOSAA.26.001767.

[129] J. Lang and B. Frank. "Fast logarithmic Fourier-Laplace transform of nonintegrable functions". In: *Physical Review E* 100.5 (Nov. 2019). DOI: 10.1103/physreve.100.053302. URL: https://doi.org/10.1103%2Fphysreve.100.053302.

[130] A. J. S. Hamilton. "Uncorrelated modes of the nonlinear power spectrum". In: *Mon. Not. Roy. Astron. Soc.* 312 (2000), pp. 257–284. DOI: 10.1046/j.1365-8711.2000.03071.x. arXiv: astro-ph/9905191.

[131] G. V. Haines and A. G. Jones. "Logarithmic Fourier transformation". In: *Geophysical Journal International* 92.1 (Jan. 1988), pp. 171–178. ISSN: 0956-540X. DOI: 10.1111/j.1365-246X.1988.tb01131.x. eprint: https://academic.oup.com/gji/article-pdf/92/1/171/1832736/92-1-171.pdf. URL: https://doi.org/10.1111/j.1365-246X.1988.tb01131.x.

[132] W. Kilian, T. Ohl, and J. Reuter. "WHIZARD: Simulating Multi-Particle Processes at LHC and ILC". In: *Eur. Phys. J. C* 71 (2011), p. 1742. DOI: 10.1140/epjc/s10052-011-1742-y. arXiv: 0708.4233 [hep-ph].

[133] G. Moliere. In: *Zeitschrift für Naturforschung A* 3.2 (1948), pp. 78–97. DOI: doi:10.1515/zna-1948-0203. URL: https://doi.org/10.1515/zna-1948-0203.

[134] H. A. Bethe. "Moliere's theory of multiple scattering". In: *Phys. Rev.* 89 (1953), pp. 1256–1266. DOI: 10.1103/PhysRev.89.1256.

[135] D. E. Groom and S. R. Klein. "Passage of particles through matter". en. In: *The European Physical Journal C* 15.1-4 (Mar. 2000), pp. 163–173. ISSN: 1434-6044, 1434-6052. DOI: 10.1007/BF02683419. URL: http://link.springer.com/10.1007/BF02683419 (visited on 09/26/2022).

[136] B. B. Rossi. *High-energy particles*. eng. Prentice-Hall physics series. Englewood Cliffs, N.J: Prentice-Hall, 1952.

[137] Student. "The Probable Error of a Mean". In: *Biometrika* 6.1 (1908), pp. 1–25. ISSN: 00063444. URL: http://www.jstor.org/stable/2331554 (visited on 10/28/2022).

[138] J. Lüroth. "Vergleichung von zwei Werthen des wahrscheinlichen Fehlers". In: *Astronomische Nachrichten* 87.14 (1876), pp. 209–220. DOI: https://doi.org/10.1002/asna.18760871402. eprint: https://onlinelibrary.wiley.com/doi/pdf/10.1002/asna.18760871402. URL: https://onlinelibrary.wiley.com/doi/abs/10.1002/asna.18760871402.

[139] F. R. Helmert. "Die Genauigkeit der Formel von Peters zur Berechnung des wahrscheinlichen Beobachtungsfehlers directer Beobachtungen gleicher Genauigkeit". In: *Astronomische Nachrichten* 88.8-9 (1876), pp. 113–131. DOI: https://doi.org/10.1002/asna.18760880802. eprint: https://onlinelibrary.wiley.com/doi/pdf/10.1002/asna.18760880802. URL: https://onlinelibrary.wiley.com/doi/abs/10.1002/asna.18760880802.

[140] E. Segrè et al. *Experimental nuclear physics. volume I*. eng. OCLC: 494335476. New York, London: John Wiley & sons ; Chapman & Hall, 1953.

[141] D. E. Groom. *Atomic and nuclear properties of air*. 2017. URL: https://pdg.lbl.gov/2017/AtomicNuclearProperties/HTML/air_dry_1_atm.html.

[142] G. Battistoni et al. "The FLUKA code: Description and benchmarking". In: *AIP Conf. Proc.* 896.1 (2007). Ed. by M. Albrow and R. Raja, pp. 31–49. DOI: 10.1063/1.2720455.